
PICK-AND-PLACE NANOASSEMBLY

Brian N. Hubert

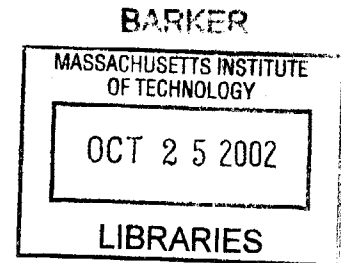
B.S./M.S. Mechanical Engineering, MIT, 1996

Submitted to the department of Mechanical Engineering in partial fulfillment
of the requirements for the degree of Doctor of Philosophy in Mechanical
Engineering at the Massachusetts Institute of Technology

May 2001
June 2001

©2001 Brian N. Hubert. All rights reserved.

The author hereby grants to MIT
permission to reproduce and to
distribute publicly paper and
electronic copies of this thesis
document in whole or in part.



Signature of the Author
Department of Mechanical Engineering, 12 April 2001

Certified by
Joseph M. Jacobson, Associate Professor of Media Arts and Sciences
Thesis supervisor

Certified by
Christine Ortiz, Assistant Professor of Material Science and Engineering

Certified by
Peter So, Associate Professor of Mechanical Engineering

Accepted by
Ain A. Sonin, Professor of Mechanical Engineering
Chairman, Department Graduate Committee



PICK-AND-PLACE NANOASSEMBLY

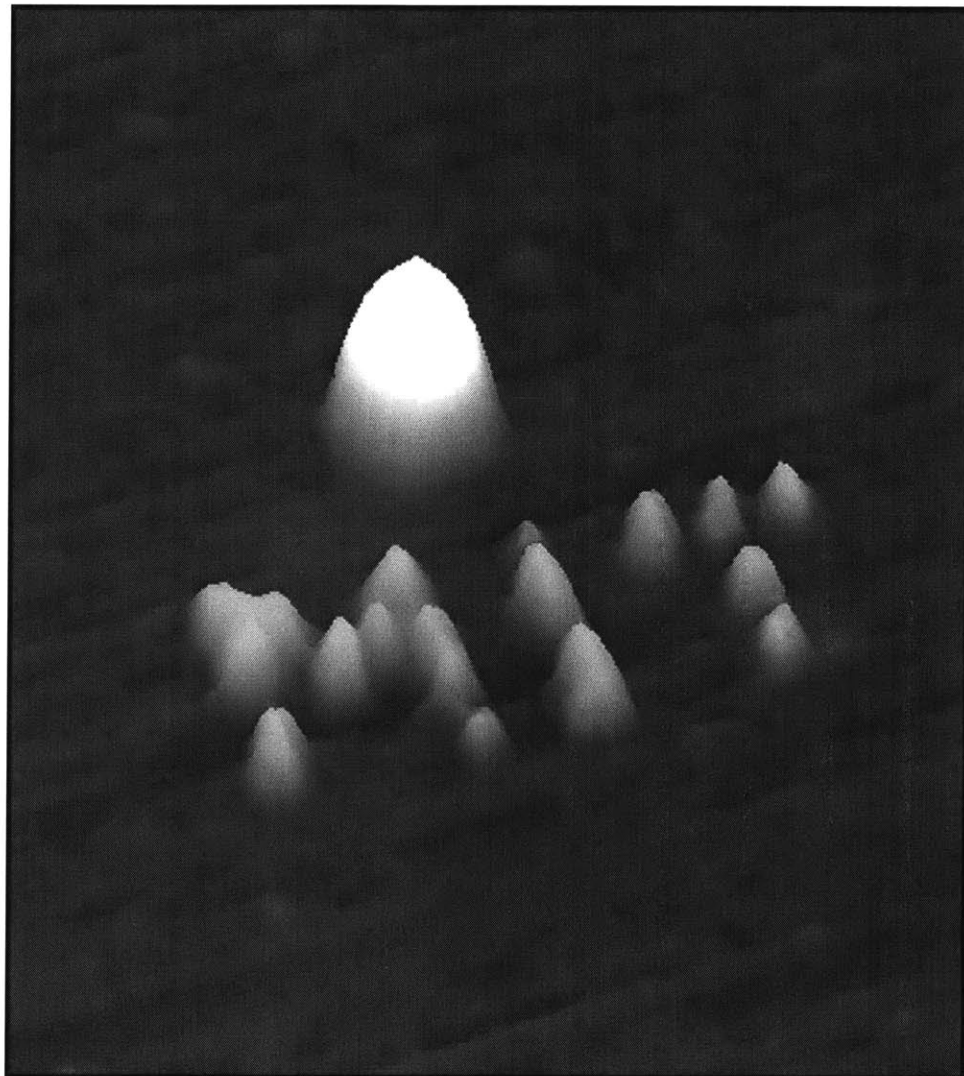
Brian N. Hubert

Submitted to the department of Mechanical Engineering in May of 2001 in partial fulfillment of the requirements for the degree of Doctor of Philosophy in Mechanical Engineering at the Massachusetts Institute of Technology

ABSTRACT

A new all-additive method for direct fabrication of nanometer-scale planar and multilayer structures using the probe tip of an atomic force microscope (AFM) and a material reservoir is proposed. The process, which is called Pick-and-Place NanoAssembly, enables true “pick-and-place” retrieval and deposition of materials with a wide range of electrical, chemical, and mechanical properties. The silicon tip of an AFM is used to discretely pick up molecules from a reservoir, transfer them to a construction zone, and then weld them to a surface. Unlike the prior art, this assembly method offers high-resolution direct patterning of a variety of materials, many of which are not amenable to patterning using current probe-based or conventional lithography methods. Metal nanoparticles, polymers, inks, solvents, and organics have been deposited onto a variety of substrates with resolutions approaching 1 million dots per inch (1 trillion dots per square inch). Lines of nanoparticles have been deposited with line widths of less than 17 nm. These materials can be assembled using reservoirs of viscous liquids, non-viscous liquids, and soft solids. Deposited volumes span a range of 10 orders of magnitude from 10^{-24} to 10^{-14} liters. Structures with dimensions of 60 to 100 nm are common, with the smallest discrete features being smaller than 32 nm. The patterning process is capable of creating structures with height-to-width aspect ratios of better than 1-to-2, and is relatively insensitive to fluctuations in temperature (3 - 30 °C) and humidity (0% - 90%). Methods for the fabrication of multi-layer structures and routes towards true three-dimensional structures are also introduced. It is anticipated that Pick-and-Place NanoAssembly will be suitable for precision deposition and direct patterning of a wide range of useful materials including semiconductors and biological compounds such as DNA. This technique promises to be an enabling tool for biological, chemical, and molecular electronics applications throughout the field of nanotechnology. Near-term applications may include the fabrication of ultra-high density gene chips, high-capacity nano-patterned magnetic disk drives, and single electron transistors.

Thesis supervisor: Joseph M. Jacobson, MIT Media Laboratory
Associate Professor of Media Arts and Sciences



The Pick-and-Place NanoAssembly system has been used to spell out the letters "MIT" by directly depositing 65 nm dots of silver metal. Each letter is 300 nm tall, and the entire word is less than 1 micrometer long. At the scale of the image above, a sewing needle lying on its side would have a thickness as tall as a 20-story office building.

ACKNOWLEDGEMENTS

I am profoundly grateful for the privileged opportunity that I have had to conduct my graduate research under the direction of Professor Joseph Jacobson at the MIT Media Laboratory. Thank you Joe, for your constant support and your enthusiastic drive to always push for the 'next great result'.

I wish to thank Professor Christine Ortiz and Professor Peter So, for their participation as valuable members of my thesis dissertation committee, and for providing insight into the nanomechanical aspects of this research.

For his specific contributions to this work, I wish to sincerely express my gratitude to Aggelos Bletsas of the Media Lab 'Physics and Media Group'. Aggelos created the custom software interface that was critical for the conversion of a conventional atomic force microscope into a true high-resolution 'pick-and-place' nanoassembly system. Our many hours of collaboration and contentious banter resulted in a software package that is capable of precisely controlling every aspect of the nanoassembly process.

During my graduate career, I have been fortunate to work with some very talented researchers. The Jacobson Group at MIT has been an extremely stimulating environment, due in no small part to lab colleagues Brent Ridley, Colin Bulthaupt, Saul Griffith, Eric Wilhelm, Babak Nivi, Sawyer Fuller, Leila Hasan, and Ivano Gregoratto.

I would also like to extend my thanks to Dr. Kathryn (Wilder) Guarini of IBM (formerly with the Calvin Quate Group at Stanford University), Lynore Abbott (formerly of Queensgate), as well as Dr. Tim Wong, Ray Eby, and John Janzer of Thermomicroscopes.

I am grateful to my family and friends for their love and support. Mom and Dad, thanks for enduring my many excited phone calls home during major breakthroughs in my research, many of which were full of arcane and probably unbearable nanotechnology lingo. And Kevin, the inventive discussions have been truly inspiring.

This research was supported in part by a National Science Foundation (NSF) Graduate Fellowship for the academic years of 1997-2000. I also enjoyed the support provided by the Amar Bose Foundation Fellowship during the 1996-1997 academic year at MIT. Based primarily on the work presented in this thesis, I am pleased to have been selected as the 2001 winner of the Lemelson-MIT Student Prize for inventiveness and the spring 2001 winner of a Materials Research Society (MRS) Graduate Student Gold Award.

LOST
Did you find this folder?



lost: **thursday night @ 8:15 PM**
where: **along memorial drive between
the media lab & ashdown house**
what: **CRUCIAL research data**
email: **bnhubert@media.mit.edu**
phone: **253-0988, 225-9870**

There is at least one amusing story that should be recounted at this point. During a three-minute bike ride from the MIT Media Lab to Ashdown House on Thursday, November 2nd, 2000, at about 8:15 PM, I lost a folder that contained about two years worth of doctoral research. Upon reaching my destination, I discovered that my backpack was wide open. I immediately retraced my path, but no folder was to be seen. I searched that path again 6 more times that night. Aggelos Bletsas added an extra pair of eyes to the hunt. I sincerely hoped that someone in the MIT community had picked up the folder just seconds after I had dropped it. Unfortunately, my name and contact information was not written inside the folder. The grand irony was that I was bringing this folder home so that I could transfer the information to my computer,

so that I would have a digital copy of my work before beginning the actual writing of my thesis. Only minutes earlier, I had gathered every piece of critical experimental data from numerous binders and consolidated them into just one easily transportable (and lose-able!) folder. I sent an email notification to Charles Vest, the president of the university. He forwarded this announcement to his staff, and then on to the entire MIT community by way of thousands of email addresses on tens of different mailing lists. I spent the night taping up posters all over campus. The next morning, Hilary Sheldon received one of those emails and gave me a very happy phone call with the news that the folder had been found. About an hour earlier, visiting Professor Kwadwo Osseo-Assare had passed along to her a folder of papers that he and his wife, Dr. Fran Osseo-Assare, had discovered fluttering in the street on Thursday night. Fran had literally chased about 100 sheets of paper blowing in the wind down the street. Although some pages bore the markings of car tires and footprints, every page was returned intact. Simply amazing. Thank you Fran and Dwadwo! It was not long before I was using a scanner to backup my data. Over the course of the next several days, the outpouring of support from the MIT community was amazing and extraordinary. At first, I received dozens of emails from concerned people. Some offering to help put up posters, to help spread the word by email, or to provide valuable eyewitness accounts of what happened and where. Once the good news was sent out, I received even more emails offering congratulations and stories of similar experiences from other people. A feature-length article entitled "Student's lost folder begets e-mail mania" was published in the "MIT Tech Talk" newspaper the next week [\[cached\]](#).

SPECIAL NOTES

This document is hyperlinked

The Microsoft Word ".doc" version of this document is thoroughly hyperlinked. Many of the links point to a wealth of internal documents and references that are contained within associated folders available on the CD-ROM version of this thesis. To retain the internal hyperlinks, the Microsoft Word document must be kept within the original file folders, with the original folder names and hierarchy. Renaming or moving folders will cause all internal hyperlinks to be lost. The Adobe Acrobat ".pdf" version of this document is also hyperlinked. However, hyperlinks that appear in the footnotes may not be activated.

Microsoft Word 2002 version [link](#)

Adobe Acrobat 5.0 version [link](#)

ABOUT THE AUTHOR



While in pursuit of his Ph.D. degree in Mechanical Engineering from MIT, Brian Hubert [a] conducted 4 years of research on alternative non-photolithographic methods for the fabrication of microscale and nanoscale memory, logic, and MEMS devices. This "siliconless" technology promises to enable the construction of computer chips on flexible sheets of plastic for a fraction of the cost of their silicon-wafer counterparts. Recent research has led to the development of a high-resolution 'pick-and-place' nanoassembler, a new class of **patented** plastic memory film [b], a silicon ink-jet device for diode fabrication, and a process for direct microstamp patterning of sub-micron resolution conducting structures for all-printed transistor technology. Previous work completed as part of a combined B.S./M.S. degree program at MIT and the Los Alamos National Laboratory, led to the development of a **patented** chemical vapor deposition (CVD) system for low-cost commercial-scale production of superconducting thin films and wires [c]. Brian Hubert is the recipient of the 2001 Lemelson-MIT Prize for inventiveness and the 1996 Amar Bose Foundation Fellowship. He has also been awarded a prize for technical achievement from the Los Alamos National Laboratory, a graduate scholarship from the National Science Foundation, and a Graduate Student Gold Award from the Materials Research Society.

[a] Brian Hubert; Email: bnhubert@alum.mit.edu; bnhubert@media.mit.edu; bnhubert@mit.edu; MIT Media Laboratory, Room E15-015, 20 Ames Street, Cambridge, MA 02139. Permanent address: 5308 W. Lincoln Avenue, Yakima, WA 98908

[b] United States Patent number 6,072,0716: "Memory structures and method of making same".

[c] United States Patent number 5,820,678: "Solid source MOCVD system".

TABLE OF CONTENTS

| | |
|---|-----------|
| Abstract | 3 |
| Acknowledgements | 6 |
| Special Notes | 8 |
| This document is hyperlinked | |
| About the Author | 9 |
| Table of Contents | 10 |
| Introduction | 13 |
| Semiconductor technology roadmap | |
| Alternative materials and fabrication methods | |
| Scanning probes as physical patterning tools | |
| Pick-and-Place NanoAssembly: Summary | 22 |
| Early research | |
| Pick-and-Place NanoAssembly system | |
| Nanoassembled structures | |
| NanoAssembler: Hardware | 31 |
| Scanning probe microscope | |
| Vibration isolation | |
| Environmental enclosure and temperature control | |
| Electronics | |
| Consumable materials: probes, inks & substrates | |
| Laser curing system | |

| | |
|---|------------|
| NanoAssembler: Software | 40 |
| Motives for a custom software tool | |
| 'LithoLab' custom nanoassembly software | |
| Custom nanoassembly function calls | |
| Nanoassembly scripts | |
| Additional considerations: Tip-reservoir alignment & tip engagement | |
| 'LithoLab' Intelligent Scripting Assistant | |
| Glossary of nanolithography modes and methodologies | |
| | |
| 2D NanoAssembly | 63 |
| Fabrication of dots with liquid-phase inks | |
| Working with liquid phase inks | |
| <i>Fabrication at low temperatures and reduced humidity</i> | |
| <i>Evaporation-insensitive inks</i> | |
| <i>Tapping mode compensation for ink pool flooding</i> | |
| <i>Frequency tuning algorithm for added mass compensation</i> | |
| Fabrication of dots with solid-phase inks | |
| <i>Grayscale dots using the "scratch pad" method</i> | |
| <i>Nano-stamping with solid-phase dots</i> | |
| Fabrication of lines | |
| | |
| 3D NanoAssembly | 91 |
| Multiple-layer structures | |
| Laser-assisted nanoassembly | |
| Local electron beam-assisted nanoassembly ("nanowelding") | |
| Thermal source-assisted nanoassembly | |
| Future routes to 3D nanoassembly | |
| | |
| Theory of NanoAssembly | 126 |
| Nanomechanical theory of material deposition | |
| <i>Hertzian and JKR models of adhesion</i> | |
| <i>Adhesion model for deposition for 2D nanoassembly</i> | |
| <i>Adhesion model for deposition for 3D nanoassembly</i> | |
| <i>Calculation of the smallest line width for a 3D column nanostructure</i> | |
| <i>Limitations of the adhesion model</i> | |
| Resonating cantilever as real-time mass transfer detector | |
| <i>Continuous beam model</i> | |
| <i>Lumped parameter model</i> | |

Comparison

Frequency shift detection sensitivity

Mass measurement sensitivity

The scale of a picogram

Routes to increasing mass measurement sensitivity

References

144

Cited references by chapter (in order of citation)

Un-cited references

Suggested reading

INTRODUCTION

Semiconductor technology roadmap

The fabrication of semiconductor industry products, such as memory chips, microprocessors, and MEMS devices, has generally required costly and time-consuming manufacturing techniques. Conventional photolithography and masking methods are used to etch patterns into films of metals and oxides on semiconducting wafers of silicon. The continual demand for greater computational power and transistor count onboard a single computer chip has driven the industry to push photolithography toward its limit. Perpetuating Moore's Law comes with a hefty price tag. Today, a state-of-the-art chip fabrication facility costs between two and three billion US dollars, and the cost of that facility must generally be recovered within no more than four years. After that time, the technology is expected to have progressed so significantly that retrofitting 'the fab' with the newer equipment may no longer be a viable option. The need for smaller and smaller logic and memory elements manufactured using techniques with even higher resolution capabilities continues to accelerate. The long-term predictions for technology nodes proposed by the International Technology Roadmap for Semiconductors (ITRS) [a] indicate that 60 nanometer design rules will need to be implemented by 2008 [Table 1]. The fabrication of microchips will very soon be a true nanotechnology endeavor. Completely new methods and materials are likely to be needed to address the challenge of patterning and constructing useful devices with features no larger than a few tens of nanometers. The unpalatable cost and looming physical limits of photolithographic techniques provide a strong incentive for the pursuit of alternative materials and methods for nano-scale technologies.

Table 1 --- Year 2000 update for technology roadmap predictions (from the ITRS)

| Int'l Technology Roadmap for Semiconductors (2000 Update) | | | | | |
|--|--------|-------|-------|-------|-------|
| Year of Production | 2001 | 2004 | 2008 | 2011 | 2014 |
| Technology Node (nm) | 130 nm | 90 nm | 60 nm | 40 nm | 30 nm |

Alternative materials and fabrication methods

In the early 1950's and 1960's, when the semiconductor industry was still in its infancy, many different materials were seriously considered as options for addressing the challenge of building microscale devices. For example, at various times in the past, cadmium selenide transistors and chalcogenide glass memory films were regarded as prime contenders in the technology race. Today, however, silicon is king. Our chips contain silicon transistors, silicon memory cells, and silicon MEMS elements. It is most probable that silicon (and other high performance wafer species such as GaAs and InP) will continue to be the material of choice for the fabrication of the highest performance computing devices. Unfortunately there are substantial costs that are associated with working with silicon wafers. In addition, form factor and processing constraints prevent wafer-bound silicon from addressing the need for large area or flexible intelligent products such as wall-sized displays, ultra-cheap wireless tags, and flexible electronic newspapers. Over the past five years, there has been a dramatic revival of research dedicated to the development of alternative materials suitable for the construction of micro-devices. Organic transistors, organic light emitting diodes (OLED), and polymer memory films are a few examples of recent efforts. Some nano-sized devices, such as single electron transistors, are made of only metal and insulators, and as such do not require silicon at all. There have also been discoveries of novel molecular switching materials that operate deep within the territory of nanotechnology, wherein the memory device may consist of a just a few molecules ---- a feat that mass-produced silicon is unlikely to achieve. As expected, these new materials will require new processing and patterning methods. Many materials that would be useful in nano-scale devices cannot currently be patterned by any known method to form very small structures. For example, certain organic molecules such as DNA and proteins cannot be patterned at nanometer resolutions with conventional resist and photolithography or electron-beam lithography techniques. And yet it would be exceeding useful if such a high-resolution patterning method did exist. Such a method would enable, for example, the fabrication of ultra-dense gene chips that could quickly read out the entire human genome, and thereby help physicians discover all the genetic-related diseases in an individual in a matter of minutes – and long before the patient showed any symptoms.

Scanning probes as physical patterning tools

Since its inception, scanning probe microscopy (SPM) has proven to be an indispensable tool for high-resolution imaging of nano-scale structures. The scanning probe is usually formed from a cantilever of silicon having a length of about 200 microns, with a tip attached to one end. The apex of the tip is very sharp and can have a radius of curvature

below 10 nanometers. Depending on the imaging mode being used, topological features as fine as individual atoms can be resolved. The most common SPM-based imaging methods are AFM (atomic force microscopy) and STM (scanning tunneling microscopy).

More recently, researchers have shown that scanning probes can also be used to modify and manipulate features on a surface. As shown in Figure 1 through Figure 11, numerous schemes have been employed to achieve nano-scale modification and manipulation of particles and surfaces. Eigler [b], Requichia [c], Superfine [d] and other investigators have demonstrated that a wide range of objects including atoms, nanoparticles, and nanotubes can be pushed into desired positions by the tip of a scanning probe. Due to the complexity of the pushing operations, construction of useful structures is necessarily tedious. Mirkin [e] [f], on the other hand, has demonstrated fully additive deposition of SAMs (self-assembling monolayers) onto gold and silver substrates using a silicon tip pre-coated with SAM molecules. The process depends on the formation of a humidity-initiated water meniscus between the tip and the surface in order to deposit the SAMs onto the metal substrate, which appears to limit patterning speed and the environmental conditions under which the deposition can occur. In addition, the Mirkin process can only be used with a very restricted set of deposition molecules (namely SAMs) and carefully chosen substrates which exhibit special substrate-liquid interactions and self-assembling chemistry.

-
- [a] "International Technology Roadmap for Semiconductors (ITRS)", 1999 Edition and 2000 update; available on the web at <http://public.itrs.net/Reports.htm>
- [b] HC Manoharan, CP Lutz and DM Eigler, "Quantum mirages formed by coherent projection of electronic structure", *Nature*, Vol. 403, No. 6769, 512-515 (2000).
- [c] R Resch, N Montoya, BE Koel, A Madhukar, AAG Requicha and P Will, "Manipulation of nanoparticles in liquids using MAC mode Atomic Force Microscopy", *Molecular Imaging Application Note*, April 1999 (1999).
- [d] MR Falvo, RM Taylor II, A Helser, V Chi, FP Brooks Jr, S Washburn and R Superfine, "Nanometre-scale rolling and sliding of carbon nanotubes", *Nature*, Vol. 397, No. 6716, 236-238 (1999).
- [e] S Hong, J Zhu, and CA Mirkin, "Multiple ink nanolithography: Toward a multiple-pen nano-plotter", *Science*, Vol. 286, Oct 15, 523-525 (1999). **[cached]**
- [f] S Hong and CA Mirkin, "A nanoplotted with both parallel and serial writing capabilities", *Science*, Vol. 288, June 9, 523-525 (2000). **[cached]**
-
-

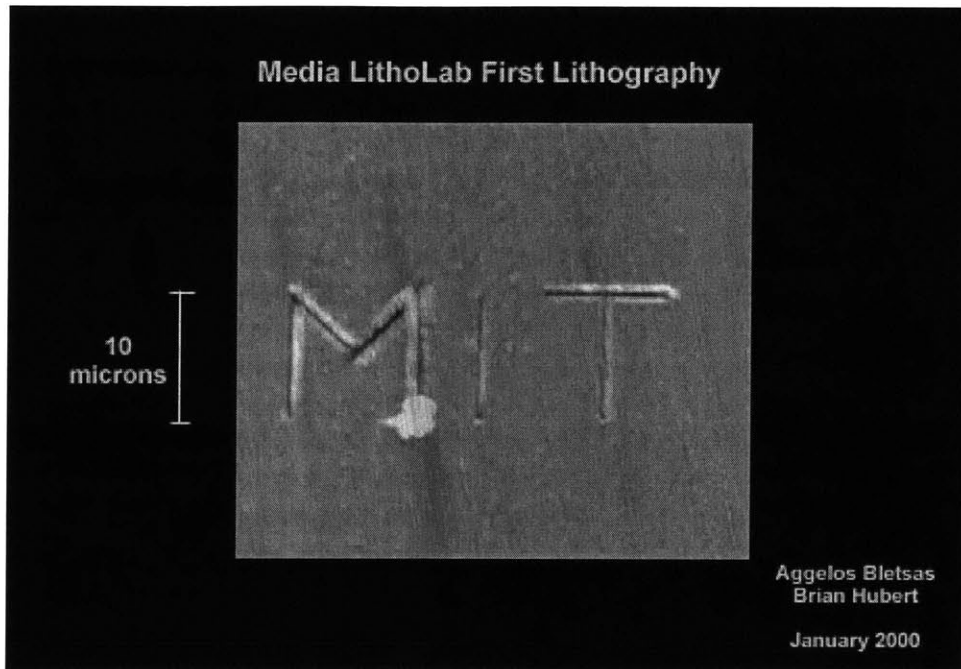


Figure 1 --- Trenches scratched into a soft-solid film with the tip of an AFM probe. B. Hubert & A. Bletsas, MIT.

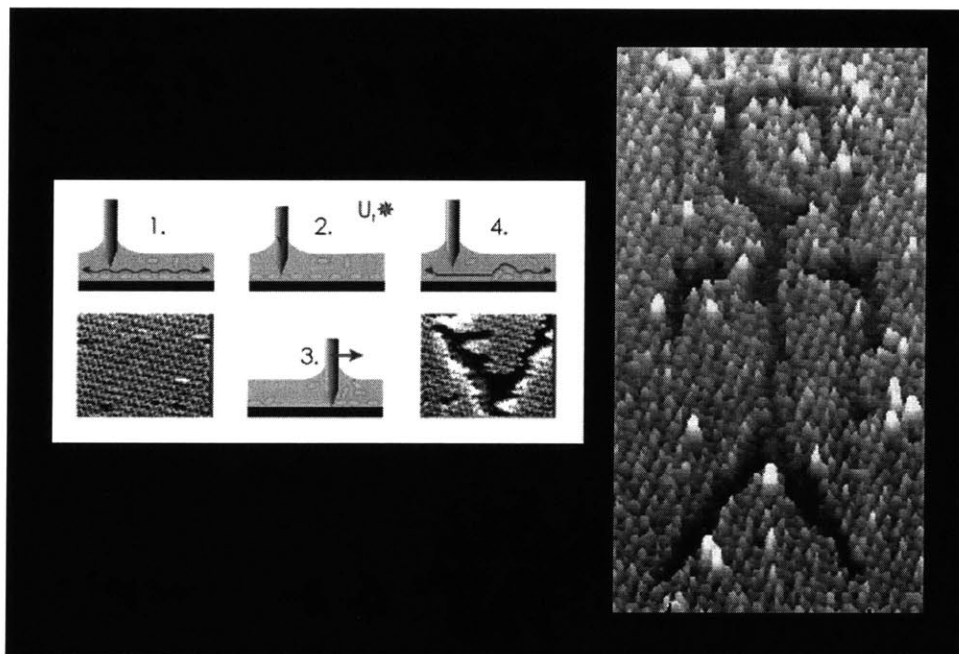


Figure 2 --- Shallow trenches carved into a self-assembled monolayer (SAM) of molecules with a charged STM probe. 1 - 3 nm line width. Reiter & Trixler, LMU Munchen.

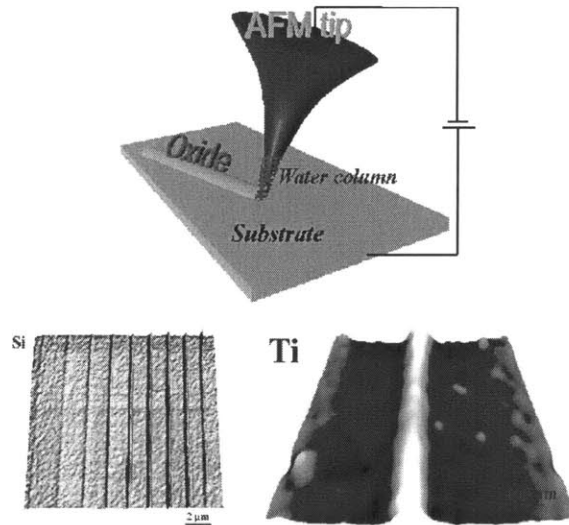


Figure 3 --- STM (scanning tunneling microscope) voltage-potential oxidation of a titanium thin film using a charged probe tip. CNR-Istituto di Biofisica, Pisa, Italy.

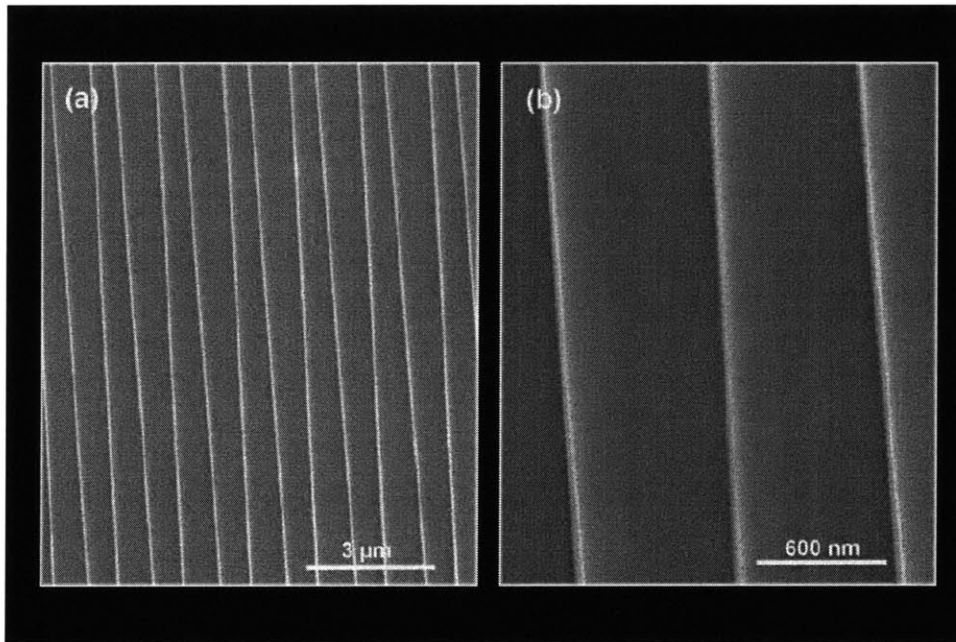


Figure 4 --- Localized electron beam exposure of etch resists with a charged STM probe tip. Line resolution can be as good as 30 nm. K. Wilder & C. Quate, Stanford University.

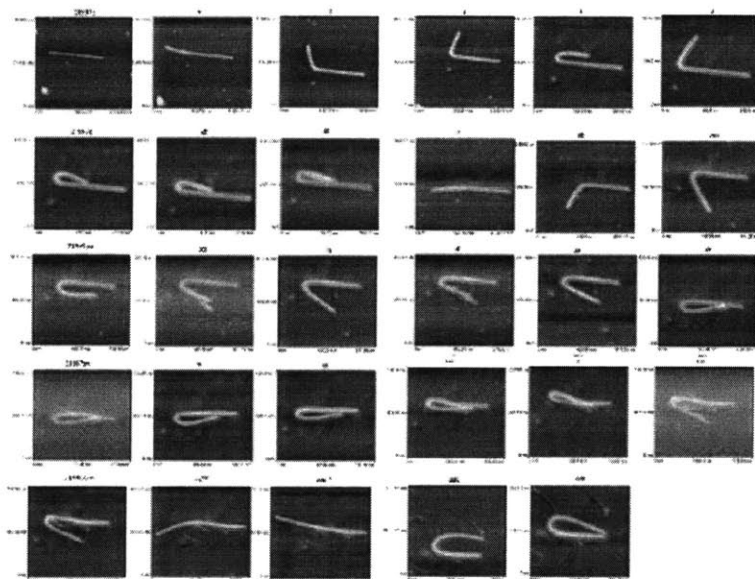


Figure 5 --- Sequential images of nano-manipulation of a carbon nanotube using an AFM probe tip. R. Superfine, Univ. of North Carolina.

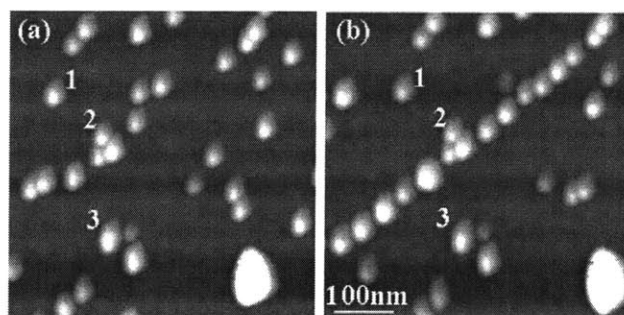


Figure 6 --- A line of gold nanoparticles meticulously assembled by many pushing and pulling actions with an AFM probe tip. Requicha & Ramachandran, Univ. of Southern California.

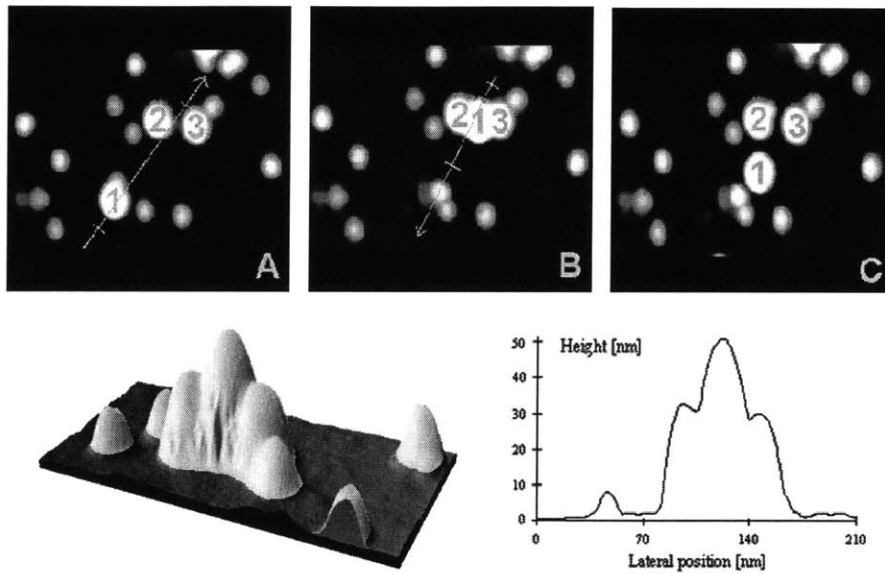


Figure 7 --- One gold nanoparticle pushed on top of two other gold nanoparticles with an AFM probe tip. Requicha & Ramachandran, Univ. of Southern California.

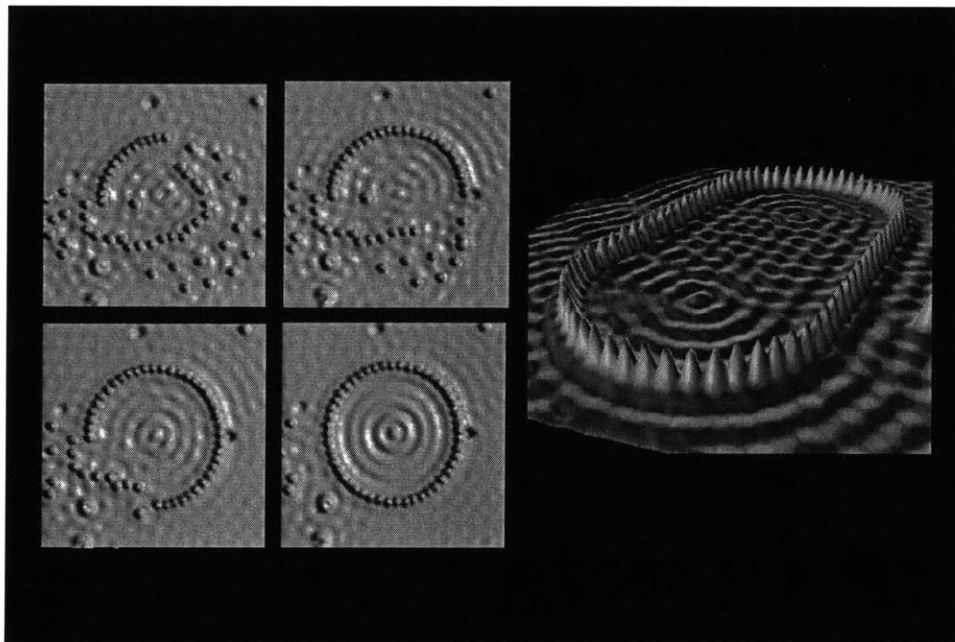


Figure 8 --- Quantum corrals formed by pulling individual atoms one by one across a surface using the tip of a scanning tunneling microscope (STM) probe. Iron atoms on a copper substrate. D. Eigler, IBM.

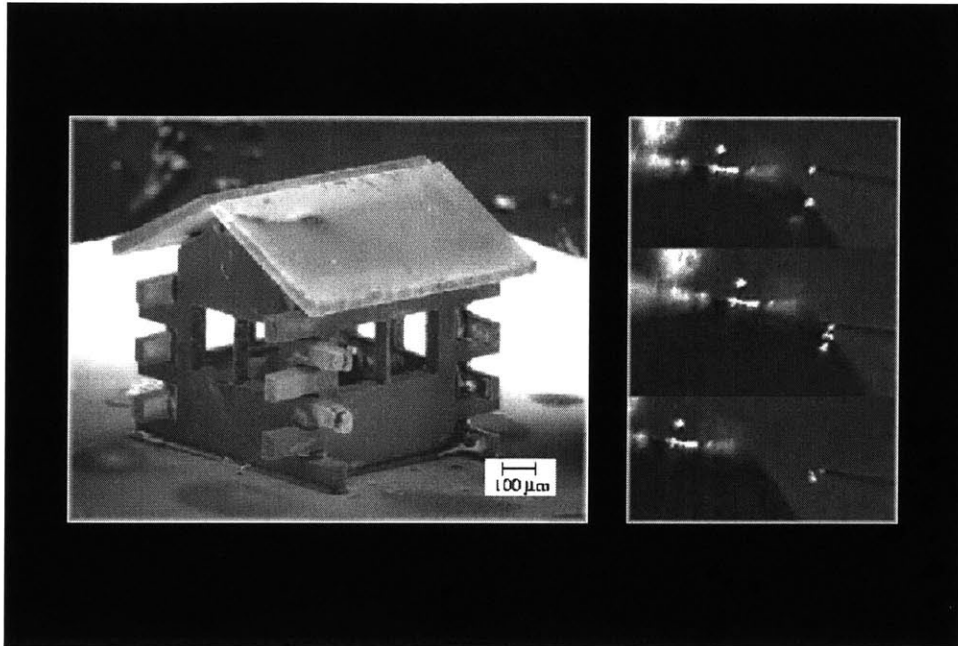


Figure 9 --- 3D assembly of micro-scale and meso-scale structures using an electrostatic probe and laser cutting tool. The house occupies a volume of approximately 1 cubic millimeter. Nakao & Hatamura, Univ. of Tokyo.

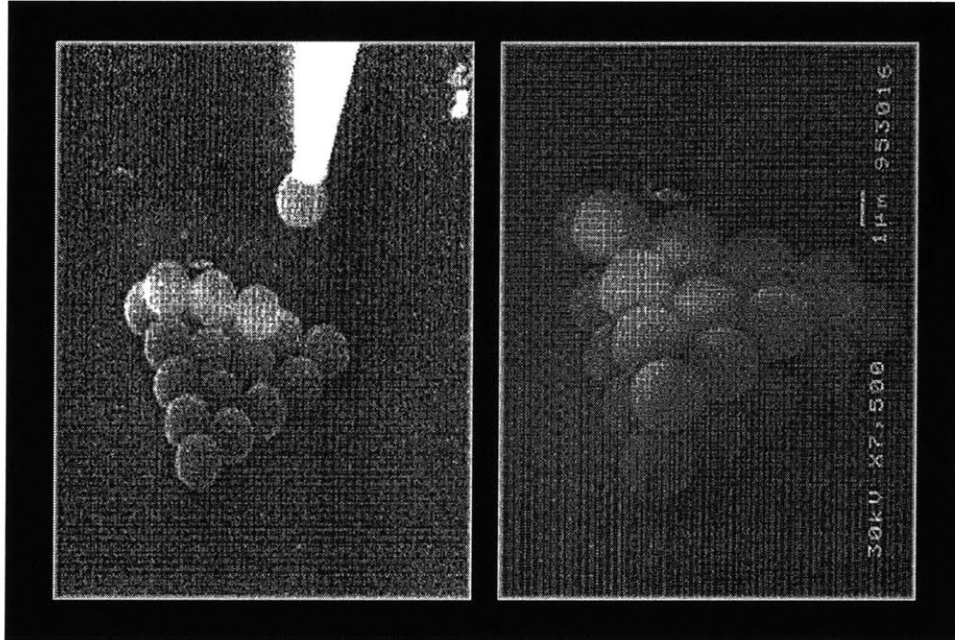


Figure 10 --- A pyramid of 2-micron spheres assembled using an electrostatic probe tool. Miyasaki & Sato, Univ. of Tokyo.

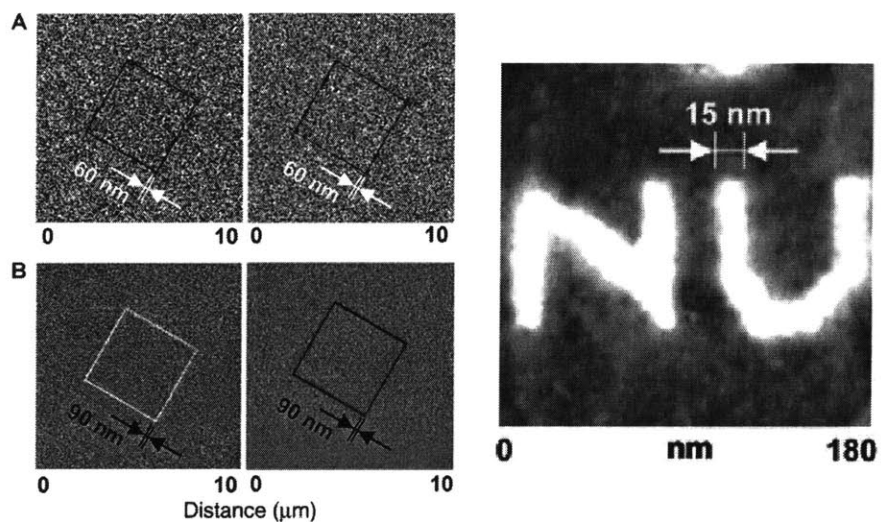


Figure 11 --- Patterns drawn onto surface by a probe tip coated with SAM molecules. The molecules are transported from the tip to the surface by a water meniscus formed between the surface and the tip. C. Mirkin & S. Hong, Northwestern Univ.

PICK-AND-PLACE NANOASSEMBLY: SUMMARY

Early research

Within the academic framework of the MIT Mechanical Engineering Department, and under the direction of Professor Joseph Jacobson, I have pursued a number of research efforts at the MIT Media Laboratory that subsequently led to the creation of the Pick-and-Place NanoAssembly system. This early work included the development of a new class of plastic memory film based on carbon-in-polymer and silicon-in-polymer formulations [Figure 12], a silicon ink-jet device for all-additive diode fabrication [Figure 13], and a process for direct stamp patterning of sub-micron resolution conducting structures useful for all-printed transistor technology [Figure 14 and Figure 15]. The common motive underlying each of these early research efforts was the discovery of new materials and fabrication methods useful for the generation of micro-scale and nano-scale devices. There has been a natural progression in my research on three fronts. Firstly, the new materials that were developed have exhibited increasingly complex electrical behavior – from passive, to passive non-linear, to non-linear with non-volatile hysteresis. Secondly, the new fabrication techniques that were invented have enabled the patterning of novel materials with finer and finer resolutions – from millimeter scale, to micro-scale, to nano-scale. And thirdly, the pursuit of the ideal universal patterning method has led to the development of new fabrication techniques that have been increasingly capable of patterning an ever-expanding variety of materials – from one semiconducting material, to several metallic materials, to essentially any material that exhibits a viscous liquid or soft solid phase.

Pick-and-Place NanoAssembly system

We propose the development of a universal high precision deposition system that is capable of directly assembling planar and multi-layer structures with high aspect ratios and nano-scale geometry onto arbitrary substrates such as plastics, metals, glasses, and semiconducting wafers. The system should be capable of precisely depositing materials with a wide range of useful electrical, chemical, mechanical, and biological properties. Ideally, this system should also provide accurate control over line width and volume deposition rate, while at the same time being relatively insensitive to environmental conditions such as temperature, humidity, atmospheric composition, vibration, and thermal drift.

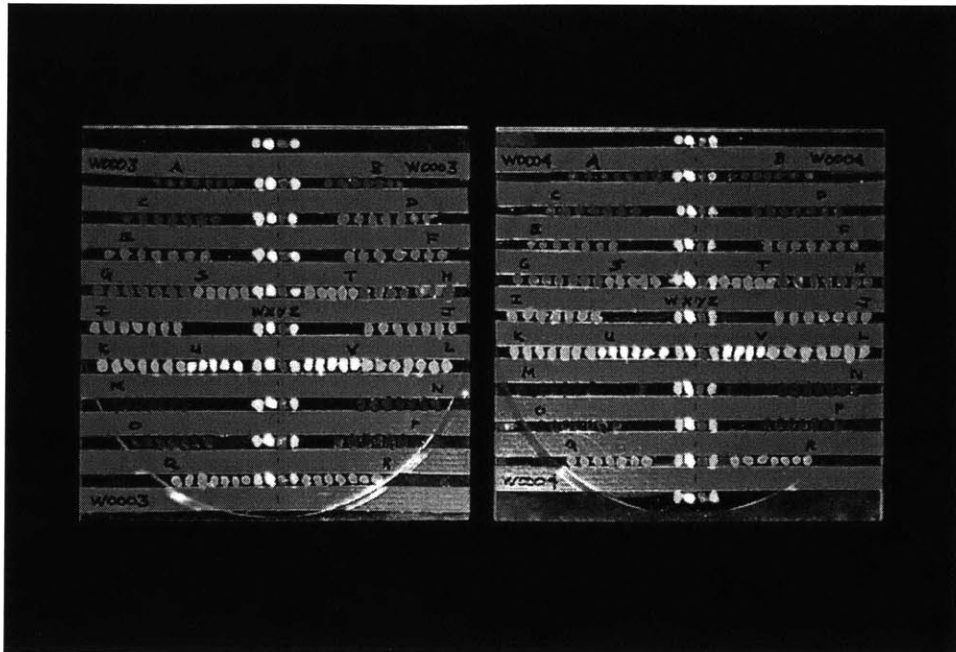


Figure 12 --- A carbon-in-polymer memory film system was discovered by the author using a combinatorial search of many metals and semimetals in various polymer compositions. Here, two silicon wafers were spotted with numerous candidate materials.

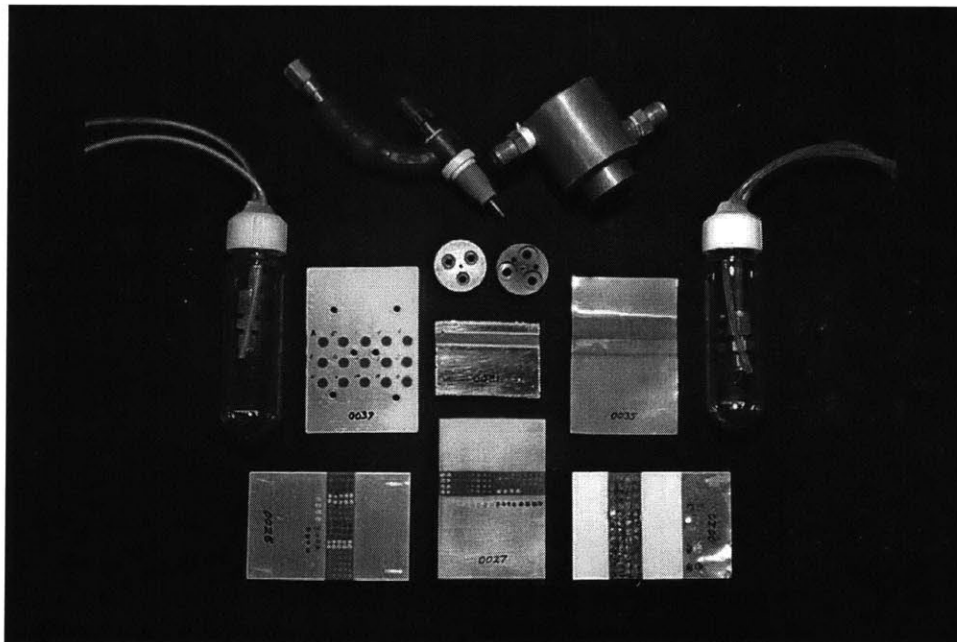


Figure 13 --- The author's silicon ink jet machine used a welding plasma jet to melt Si particles entrained in a gaseous flow. Upon exiting the nozzle, the molten particles were deposited onto various substrates such as copper and aluminum foil to form diodes.

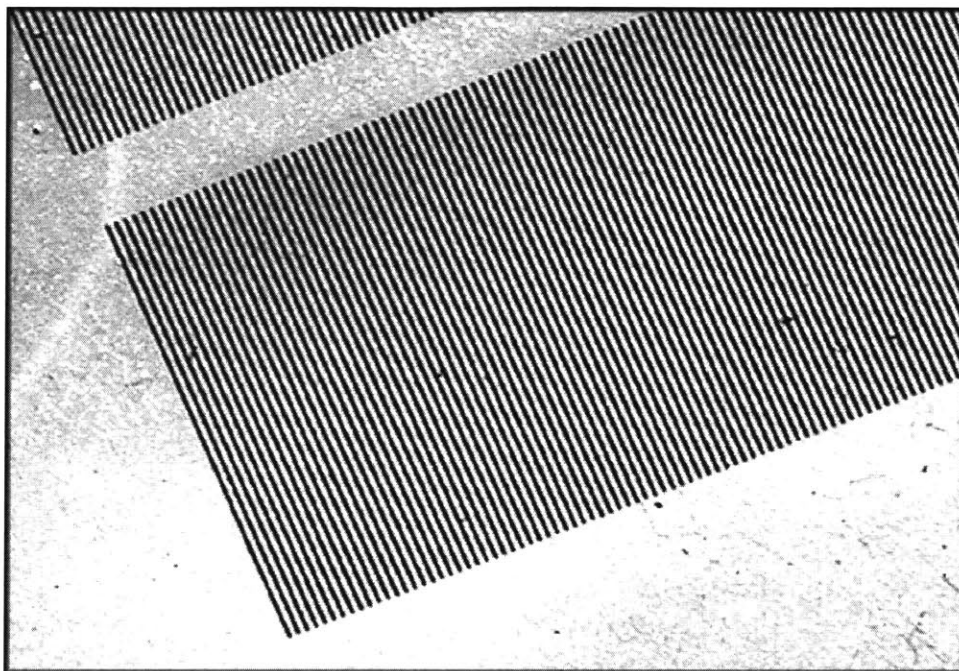


Figure 14 --- The author used direct stamping of metal nanoparticle inks to generate fine metallic features. The general procedure involved the transfer of a pattern of liquid-phase ink from a PDMS stamp onto a suitable substrate such as glass or plastic.

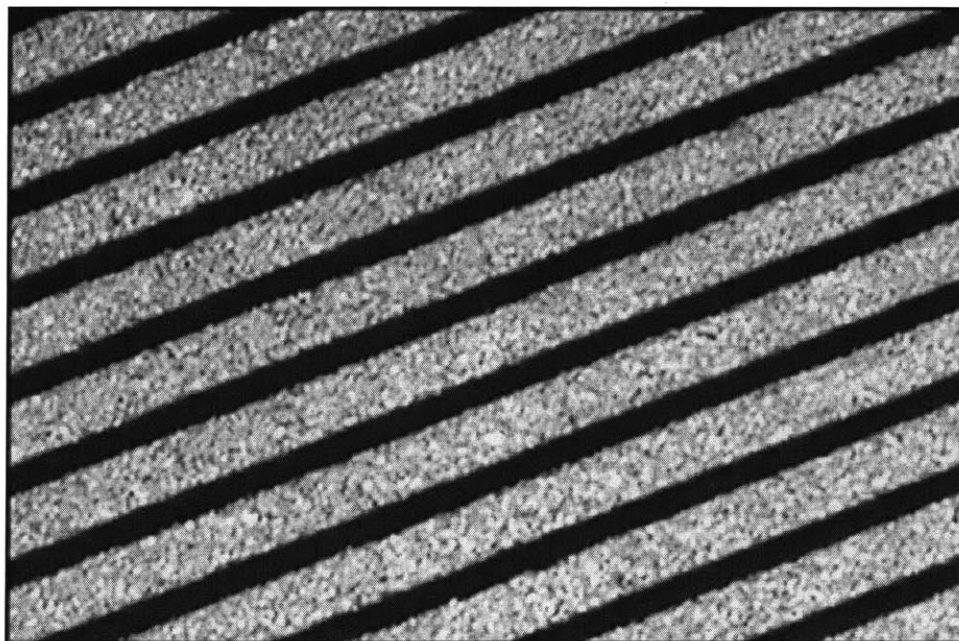


Figure 15 --- Fine metallic features were created using the author's direct stamping technique. The silver metal grating pattern shown here consists of 3.5 micron wide lines with 1.5 micron spaces. The metal lines are 20 nm thick with 300 nm edge resolution.

We have developed a device and process that meets many of the aforementioned desirable characteristics for a universal nano-scale deposition system. The sharp tip on the end of an atomic force microscope (AFM) probe is used to assemble and then image nano-sized structures with high precision. The process, which has been named Pick-and-Place NanoAssembly (PPNA), can deposit materials directly onto arbitrary substrates. Unlike other probe-based nano-manipulation devices that simply push atoms or nanoparticles around on a surface, the NanoAssembly system is capable of picking up and then depositing materials using true "pick-and-place" operations. Exceedingly small quantities of material are picked up by a silicon tip from a reservoir and are then assembled at a designated construction site on the substrate [Figure 16 and Figure 17]. The reservoir can contain viscous liquids, non-viscous liquids or soft solids. Deposited volumes span a wide range from 10^{-23} to 10^{-14} liters, and line widths of 60 to 100 nm are common, with the smallest features being less than 40 nm [Figure 18]. Single layer structures with height:width aspect ratios better than 1:2 have been demonstrated.

The difficulties of directly patterning structures at these small dimensions are many. Because objects behave so differently at nano-scales, some experts in the field have seriously doubted the feasibility of discretely picking up, moving, and depositing very small particles of arbitrary materials. To overcome these challenges, dozens of computer-controlled parameters for dictating every aspect of the NanoAssembly process have been implemented within a custom script-based software package called LithoLab [a]. Proper tip velocity, dwell time, and imperceptibly small forces are used to retrieve and deposit materials with reliability. An intelligent software system that automatically generates templates for scripted commands has also been developed. Solutions to the most difficult problems required a host of innovations including an in-situ cooling system, an environmental chamber with vibration isolation stage, and an integrated infrared laser device for thermal curing. The entire desktop apparatus is no larger than a carton of milk.

Additional efforts have been focused on the fabrication of true three-dimensional structures like columns and walls, which are likely be the fundamental building blocks for nano-robotics and other nano-scale electro-mechanical devices. New methods have been devised for assembling layers of molecules together to form objects with vertical geometries. For example, one method of construction utilizes an electron beam emitted from the tip of a scanning probe to instantly weld new materials into place. Infrared laser beams and thermally activated probes and substrates have also been employed to achieve multi-layer results. In some constructions, several hundreds of layers have been assembled and welded together. To our knowledge, this is the first time that such nano-structures have been incrementally built up layer by layer using a discrete pick-and-place process.

Nanoassembled structures

Dots and lines are the most basic canonical structures that have been fabricated using the Pick-and-Place NanoAssembly system. The geometry of both kinds of structures can be altered by a number of parameters, the most important of these being the contact or tapping mode of the AFM probe, and the solid or liquid phase of the materials in the reservoir. Other important parameters include the pressure and lateral speed of the tip, as well as the velocity of vertical approach of the tip to the surface. Dots can be formed by dipping the tip into a reservoir of a soft solid, translating the tip to the construction site, and then quickly lowering the tip to make contact with the substrate surface. Using current tools, one dot can be formed every second. The aspect ratio for single layer dot structures can be as good as 1:2. As expected, the deposited dots can be assembled to form more complicated patterns like lines and letters [Figure 19].

Due to the extra degree of feedback sensitivity offered by a vibrating tapping mode probe, deposited volumes and minimum dot diameters are generally smaller for dots deposited using tapping mode than for contact mode. Contact mode volumes and dot diameters are generally on the order of 10^{-19} Liters and 100 to 160 nm, while tapping mode can typically provide less than 10^{-22} Liters and 60 to 100 nm. Most recently, sub-40 nm dots have been formed by using a tip in tapping mode and a liquid reservoir. Grayscale patterns with varying line widths can be generated by a single reservoir dipping operation followed by two or more consecutive deposition steps [Figure 20]. Additional work has shown that dots can be placed on top of one another to form multi-layer structures, and can be accomplished with and without the assistance of intermittent laser, thermal, and electron beam initiated curing.

Lines can be directly patterned by dragging a material-laden tip across the surface of a substrate while applying sufficient vertical force. Lines can be formed continuously at high speeds that range between 10 and 100 microns per second. When using the contact mode and a liquid-phase material, a large liquid bulb is often deposited at one end of the line. By using the tapping mode during writing, the "bulb problem" is resolved, and line widths can be as good as 55 to 70 nm [Figure 21].

The use of reservoirs containing liquid materials can be challenging. When dipping a tapping mode vibrating tip into a liquid reservoir, substantial mass can be suddenly added to the tip. This causes the resonance frequency of the cantilever supporting the tip to drop, and causes the amplitude to increase. Then, in the fraction of a second required to transfer the tip to the deposition zone, a significant portion of the liquid mass may leave the tip due to solvent evaporation. Because tapping mode AFM operations are regulated by resonance frequency feedback control, a tuning algorithm that dynamically

compensates for frequency changes was developed. This tuning operation was often implemented just after withdrawing material from the reservoir, and again just before deposition. Throughout the patterning process, the changing resonance frequency can be actively monitored and recorded, thereby allowing calculation of the precise amount of material being transferred per unit time. With a frequency sensitivity of about 130 Hertz, mass changes as small as 12 picograms ($\sim 10^{-15}$ kg) can be observed.

[a] The LithoLab custom lithography software interface was primarily authored by Aggelos Bletsas, Physics and Media Group, MIT Media Lab

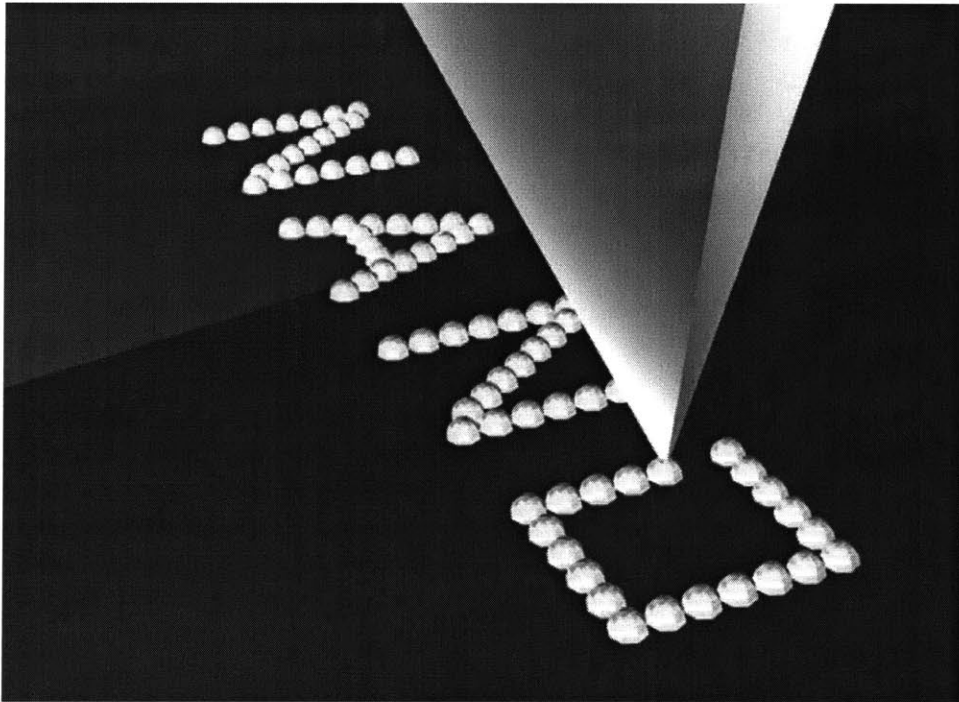


Figure 16 --- A rendered view of the extreme end of the tip used to pick up and deposit discrete dots of material to form the letters in the word "NANO". The AFM probe comprises a sharp tip attached to the end of a silicon cantilever.

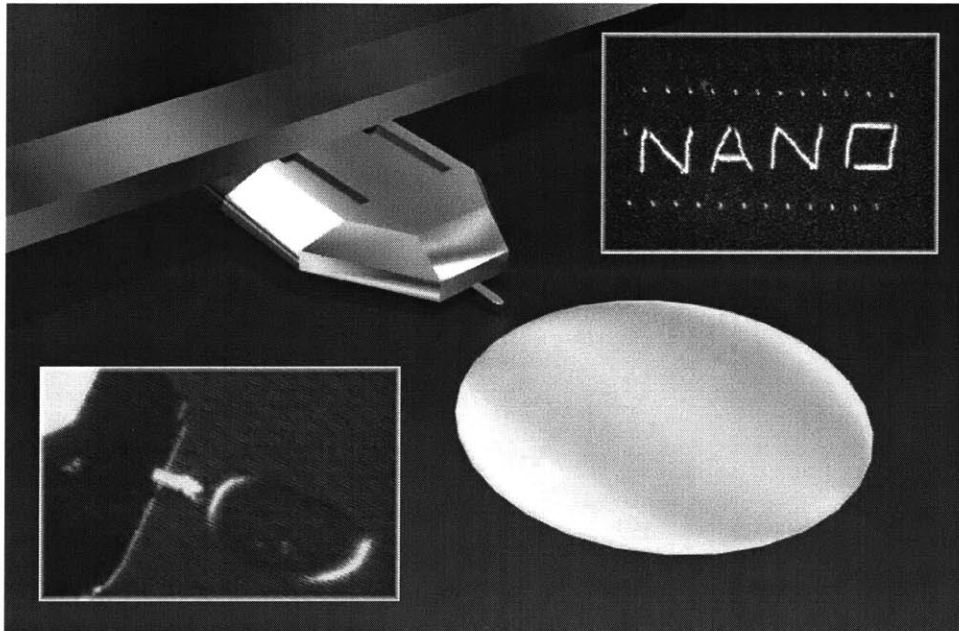


Figure 17 --- Rendered and optical views of the silicon cantilever and the material reservoir. The tip is on the underside of the cantilever and cannot be seen here. Upper right: SEM image of the word "NANO" assembled from gold nanoparticles. Each letter is 2 microns across.

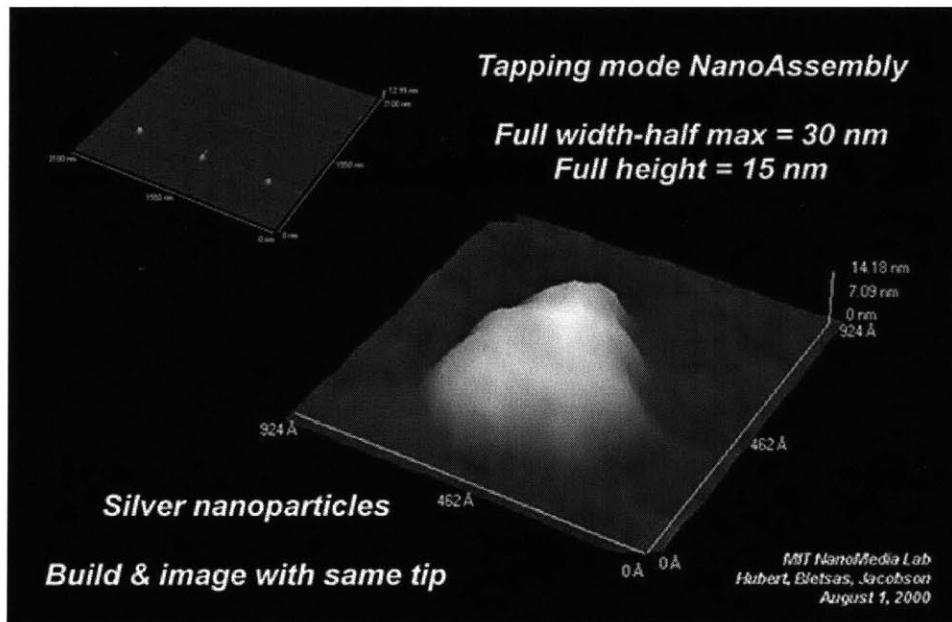


Figure 18 --- These 32 nm wide dots of silver nanoparticles are also 15 nm high, to give an extraordinarily good height:width aspect ratio of nearly 1:2. About 80 atoms can fit

across the diameter of the deposited dot. At the scale of this image, a sewing needle's thickness would be about 2000 feet high. This AFM image has no vertical exaggeration. The same tip was used for both NanoAssembly of the dots and subsequent AFM imaging.

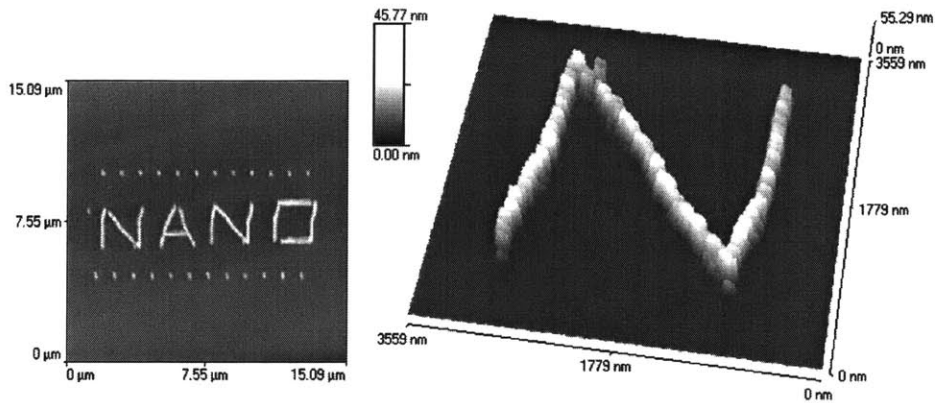


Figure 19 --- The NanoAssembly process was used to spell out the letters "NANO" using gold nanoparticles. Each letter is 2 microns across. Image obtained with an AFM.

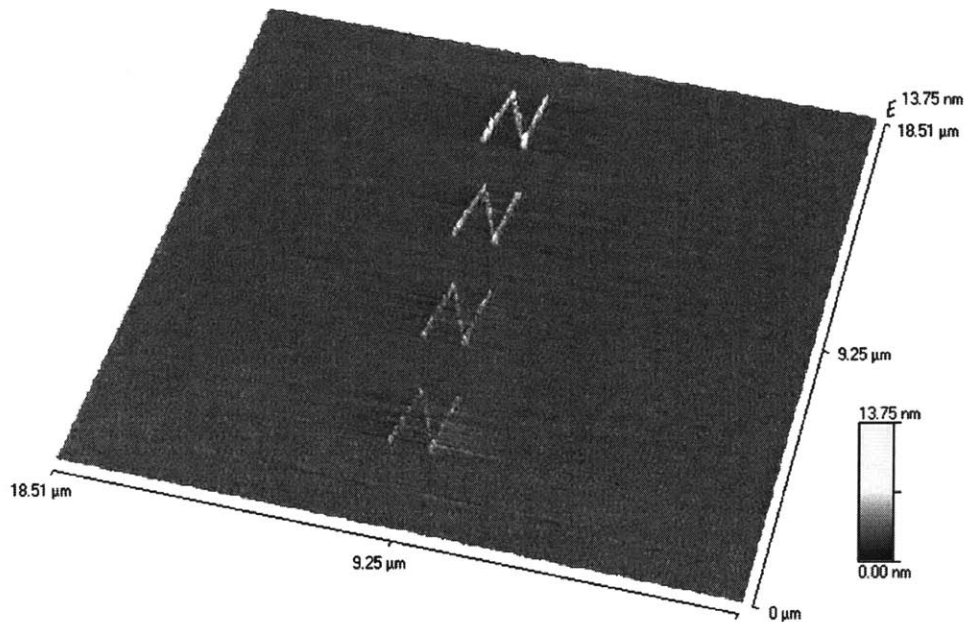


Figure 20 --- Four copies of the letter "N" have been nanoassembled in parallel. Four different line thicknesses were achieved by using a single reservoir dipping operation followed by four consecutive deposition steps, one for each "N" being constructed.

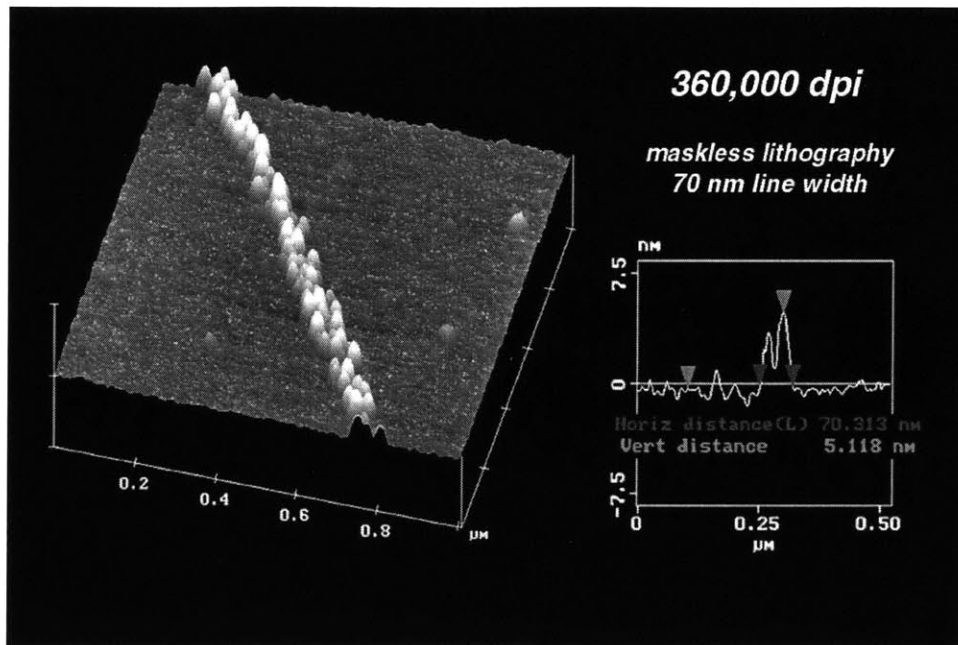


Figure 21 --- A 70 nm wide line of silver nanoparticles was deposited by dragging a silver ink-laden AFM tip across a surface in tapping mode. The width of the line can be varied by changing the pressure applied by the tip to the surface.

NANOASSEMBLER: HARDWARE

Scanning probe microscope

The working principles of an atomic force microscope (AFM) are relatively simple. Three piezoelectric transducers control the movement of a scanning probe tip along the XYZ axes for imaging purposes at the nano-scale range. In an alternate configuration, a single “tube piezo” may be used to execute movements along all three axes. When the tip at the end of a cantilever-style probe is brought into direct contact with a surface in “contact mode”, the cantilever bends ever so slightly. A laser beam and photodetector arrangement is used to detect the cantilever deflection, which is generally in the range of a few tens of nanometers. An electronic feedback loop controls the movement of the Z-axis piezo to maintain constant deflection of the cantilever, which allows the tip to deliver constant force to the surface. The required movements of the Z-piezo as a function of planar X and Y coordinates during raster scanning are recorded and linearized, and are then displayed on a computer screen as a three-dimensional image. The image is a representation of topographical nature of the scanned surface. When used for “tapping mode” (non-contact mode) imaging, the same laser and detector arrangement is implemented within a Z-piezo driven feedback loop so that the mechanical resonant frequency of the vibrating cantilever is held constant as the tip is scanned across the features of a surface.

The Pick-and-Place NanoAssembly (PPNA) system is based on the Explorer model scanning probe microscope manufactured by Thermomicroscopes [a] (formerly Topometrix). The Explorer [b] microscope is capable of performing a range of scanning probe techniques including contact mode and tapping (non-contact) mode atomic force microscopy (AFM), lateral force microscopy (LFM), scanning tunneling microscopy (STM), scanning electro-potential microscopy (SEPM), scanning capacitance microscopy (SCM), magnetic force microscopy (MFM), and micro-thermal microscopy. The scanning “head” of the Explorer [Figure 22] system is a soda can sized device with a tripod piezo configuration that allows the for imaging of a 100 micron by 100 micron planar area using its X-axis and Y-axis piezo stacks. A third piezo stack provides 10 microns of vertical movement along the Z-axis. A scanning probe, usually in the form of a silicon cantilever with a sharp tip at its end, is secured directly to the underside of the Z-axis piezo stack [Figure 23] by way of a magnetic mounting plate tilted at a nominal 4.5 degrees relative to the substrate. Additional inclination of the cantilever can be provided by adjustments to the two elevator screws on the rear section of the AFM head. Unlike most AFM systems available on the market, the Explorer offers real-time closed-loop linearization of X-Y piezo movements. This strain gauge linearized closed-loop

control capability, dubbed "TrueMetrix" by the manufacturer, is crucial for nanolithography operations, wherein repeated movements to precise locations must be extremely reproducible. In addition, the linearization ensures that straight-line movements are in fact straight, without the accumulation of piezo-related hysteretic errors. The Explorer system consists of five primary components: (1) the Explorer scanning head; (2) the electronic control unit (ECU), which contains high voltage amplifiers and all scanning probe related electronics including the mother board; (3) the "1010" connector box, which routes the primary control signals between the ECU and the head; (4) a personal computer and CRT screen; and (5) a television monitor for visualizing the scanning probe through the optical microscope CCD located on the side of the Explorer head. Considerable care was taken to ensure the selection of the proper scanning probe system. Before settling on the Explorer as the optimal choice, other options were seriously considered. For example, in one proposed scheme, a Queensgate NPS-XYZ-100/15A three-axis piezo stage, with 3 nm repeatability closed-loop motion control, was to be integrated with a Digital Instruments D3100 AFM system with an open-loop piezo scanner. The Explorer system simultaneously offers at least two key features that no other system can deliver. First, the Explorer provides closed-loop X-Y piezo scanner control. And second, and perhaps most importantly, the Explorer control software can be easily modified for the development of custom automated lithography scripting operations. Once the Explorer system was acquired, a full battery of tests was carried out to verify performance capabilities. These tests were used to determine the Explorer's X-Y imaging resolution, thermal drift at room temperature, repeatability of piezo movements, and Z-axis noise floor.

Vibration isolation

Scanning probe systems are generally large and heavy instruments, and vibration isolation is most often provided by a multi-thousand dollar air levitated isolation table. The air is usually supplied by a pressurized tank and regulator. The scanning portion of the Explorer system, known as the 'head', is exceptionally compact and weighs less than 2 pounds. With some experimentation, it was discovered that a custom bungee-cord supported stage can provide excellent vibration isolation while maintaining a very small physical footprint. As an added bonus, the cost of materials for this solution was approximately \$15, which compares favorably to the \$5,000 to \$10,000 cost of a commercial vibration isolation table. Two bungee-cord based designs for the stage have been implemented. The first design [Figure 22] comprises a heavy metal plate hung from a cantilevered shelf by way of two pairs of criss-crossed bungee cords. To further restrict lateral movement and improve damping, the bottom of the plate is connected to a very heavy and stationary anchor plate with two more pairs of criss-crossed bungee cords. This design is useful for supporting the Explorer AFM head alone. A second isolation

stage design [Figure 24], with a slightly different bungee-cord arrangement, can support the head as well as a clear plastic enclosure for atmospheric composition control. A third isolation stage design requires no bungee cords at all. Amazingly, very satisfactory nanoassembly and imaging results can be obtained by placing the AFM head on top of a multi-layer stack of damping materials on a wobbly desk. The damping materials consist of two layers of plastic bubble-wrap on top of a single layer of half-inch thick carpeting. Measurements taken by a MEMS-based accelerometer have shown that this very simple stage provides vibration isolation good to about 5 micro-G's (5 millionths of earth's gravitational acceleration) over a large range of frequencies.

Environmental enclosure and temperature control

Many of the liquid-phase ink materials used in the nanoassembly experiments contain solvents that evaporate rather quickly, which causes large changes in the viscosity of the ink reservoir on the substrate. Viscosity fluctuations are highly undesirable in the middle of a nanoassembly run, as ink viscosity has a major effect on the geometry of the deposited structures. A peltier stack attached to the underside of the substrate cools the reservoir, which substantially reduces the evaporation rate and stabilizes the viscosity for extended periods of time. Humidity-initiated moisture condensation on the cooled substrate is prevented by an environmental enclosure [Figure 25] with atmospheric composition controls. With sufficient overpressure supplied by an argon or nitrogen gas tank, the humidity in the enclosure can be driven down to 0% within several minutes. Relative humidity, atmospheric temperature, and substrate temperature monitoring systems are installed inside the enclosure along with the Explorer AFM head, substrate positioning stage, and *in situ* curing laser. With the peltier cooling and humidity control systems in place, some ink materials that normally evaporate within just a few minutes at room temperature (25 C.), can be kept in the liquid phase for more than an hour at 3 degrees C. and 0% humidity. When required, the voltage polarity supplied by an amplifier can be reversed so that the peltier stack provides in-situ thermal curing of ink structures deposited onto the substrate by the nanoassembly technique.

Electronics

Many experiments were conducted in the process of discovering the tools and procedures necessary for planar and multi-layer nano-structure fabrication. Most of these experiments required additional electronic components [Figure 26] including a high voltage amplifier, current pre-amplifier, voltage pre-amplifier, oscilloscope, function generator, laser, shutter system, and cabling. A detailed discussion and diagrams of the implemented circuit layouts are presented in the experimental section of this thesis.

Consumable materials: probes, inks & substrates

Cantilever-style probes are used as the additive deposition and lithography instruments in the Pick-and-Place NanoAssembly process. The probes come from a number of sources including commercial vendors and academic research labs. Standard contact mode probes (with the two-legged triangular cantilever design) are generally not stiff enough to be used for dot and line construction. The bending stiffness of a contact mode probe is usually so low, and the relative surface area of the supporting cantilever so large, that long-range electrostatic interactions with the substrate can cause the cantilever to bend, even before the tip fully engages the surface. Instead, commercial tapping mode probes with thin rectangular cantilevers are employed for the vast majority of the nanoassembly experiments. These tapping mode probes feature substantially increased stiffness, which minimizes the effects of electrostatic forces. In many early experiments, factory-mounted tapping mode probes from Thermomicroscopes [c] were employed. However, these probes are quite expensive and are easily destroyed by typical nanoassembly procedures. Un-mounted tapping mode probes from Molecular Imaging [d] and MicroMasch [e] are less expensive and often yield superior results. The NSC12/W2C model probes [f] from MicroMasch are particularly useful for a variety of nanoassembly applications. These un-mounted probes have six closely spaced cantilevers with a variety of stiffness levels and lengths. The bending force constants of the cantilevers span a range from 0.3 N/m to 14 N/m, with mechanical resonant frequencies between 21 kHz and 210 kHz. Because each cantilever has a different length, the Explorer AFM head can be tilted so that only one cantilever touches the substrate at a time. It is easy to conduct nanoassembly procedures with one cantilever, and then immediately switch to tapping mode imaging with a fresh unused cantilever. The tips of these silicon probes are coated with a conductive layer of tungsten-carbide [g], which is useful for multi-layer e-beam cured depositions. For special applications, like multi-layer assembly, pre-mounted thermal probes [h] from Thermomicroscopes are used. The tip of each thermal probe is constructed from a V-shaped wire of a platinum-rhodium alloy that exhibits a significant temperature coefficient of resistance. Additional experiments were conducted using custom thermal probes contributed to the project by Yiching Liang of the Thomas Kenney group at Stanford University. These probes are capable of providing temperatures as high as 300 degrees Celsius with time constants of 1 to 10 microseconds.

Although a variety of materials in both liquid and soft solid phases have been used in the nanoassembly experiments, most work is conducted using commercial gold and silver nanoparticle inks. These metal inks, which have concentrations of 30% to 40% metal by weight, are often diluted with alpha-terpineol to reduce both the viscosity and the thickness of the reservoir. The reservoir is comprised of a small oval-shaped pool of ink, with a long dimension of 200 to 1000 microns, formed by the manual transfer of a tiny volume of liquid from a bottle to the substrate using the end of a very thin metal wire.

The oval shape of the pool reduces the likelihood of “flooding” when the tip engages an ink material that exhibits a large contact angle relative to a non-wetting surface. The nanoassembly deposition zone is generally located within 50 microns of the edge of the reservoir adjacent to one of the long ends of the oval. After the nanoassembly process is complete, the patterned metal ink and the reservoir are thermally cured on a hotplate. Other inks that have been successfully deposited onto substrates using the nanoassembly technique include Dow Sylgard 184 (a silicone elastomer pre-cursor and curing agent), Norland optical adhesive #72 (a UV-curable clear adhesive), Filmtronics spin-on-glass diluted with alpha-terpineol, and Shipley SPR 3012 photoresist diluted with alpha-terpineol.

Laser curing system

Many ink materials require a thermal cure after patterning. Generally this curing step involves the removal of the substrate from the positioning stage followed by heating on an external hot plate. Once the substrate is removed from the positioning stage, it is very difficult and time-consuming to again find the previously nanoassembled structures for subsequent imaging. *In situ* thermal curing with an infrared laser enables immediate solidification and imaging of nanoassembled patterns without removal and realignment of the substrate. This improvement dramatically reduces the cycle time for patterning, curing, and imaging. In addition, the IR laser can provide intermittent thermal curing during nanoassembly runs, which is useful for the fabrication of multilayer structures.

The laser curing system comprises an IR laser source and rotating mounting bracket, laser beam shutter, AFM head positioning stage, and camera beam blocker. An IRE-Poulus Group ytterbium fiber infrared laser emits at 1060 nm and supplies up to 5 watts of optical power. The near-collimated laser beam is focused down to a 20 micron by 10 micron spot on the substrate using an 11 mm focal length lens at the end of a metal tube inserted into the side of the AFM head. To obtain the smallest spot size, the lens is positioned about 11 mm away from the substrate. Timed laser beam exposure is enabled by a solenoid-driven shutter positioned between the laser source and the focusing lens. Laser bursts as short as 50 milliseconds are triggered by timing signals from the computer during the execution of nanoassembly runs. The CCD camera on the AFM head is protected from excessive laser beam exposure by a custom beam blocking mechanism attached to the rotating focusing wheel of the camera.

For a number of reasons, including frequent adjustment of the control knobs on the side of the AFM head, the length of the laser beam path from the laser source to the substrate can be no shorter than 12 inches. Considerable effort was devoted to the design of an aiming device that precisely steers the laser beam onto the “nanoassembly zone” on the

substrate using the focusing lens embedded within the AFM head. After the design and testing of five lens aiming devices, the sixth and final device [Figure 69] provides sub-micron resolution placement of the laser beam spot upon the substrate. This aiming device offers fine control of the horizontal location, lateral location, rotation, pitch, and yaw of the focusing lens relative to the incoming laser beam. Additionally, the laser source is mounted on its own dual-axis rotating stage [Figure 67], which provides even more beam aiming flexibility.

-
- [a] ThermoMicroscopes, 1171 Borregas Avenue, Sunnyvale, CA 94089, <http://www.thermomicro.com>, info@thermomicro.com , Phone: (408) 747-1600, 1-800-727-5782.
- [b] Thermomicroscopes Explorer scanning probe microscope brochure [[cached](#)].
- [c] ThermoMicroscopes pre-mounted high resonance frequency tapping mode silicon cantilevers: model 1650-00; 320 kHz; 42 N/m force constant. Website: www.thermomicro.com. Tel: 408-744-3001, 800-727-5782 Address: 1171 Borregas Avenue, Sunnyvale, CA 94089. See brochure [[cached](#)].
- [d] Molecular Imaging Corporation: model NCH (NCH-16); 330 kHz; 42 N/m force constant. Website: www.molec.com. Tel: (800) 819-2519, (480) 753-4311. Address: 9830 S. 51st Street, Suite A124 Phoenix, AZ 85044. See brochure [[cached](#)].
- [e] MicroMasch (Silicon-MDT, Moscow, Russia) un-mounted high resonance frequency tapping mode silicon cantilevers: model NSC15; 325 kHz; 40 N/m force constant. Dimensions: 4 microns thick by 35 microns wide. Cantilever length: 125 microns. Websites: www.spmtips.com, www.micromasch.com, www.siliconmdt.com. Distributed in the USA by K-TEK International, 7086 S.W. Beveland Street, Portland, Oregon 97223. Website: www.ktekintl.com. Tel: (503) 624-0315. See brochure [[cached](#)].
- [f] MicroMasch (Silicon-MDT, Moscow, Russia) un-mounted high resonance frequency tapping mode silicon cantilevers: model NSC12/W2C (model NSC12 cantilevers with tungsten-carbide coating); 6 cantilevers on one chip. Resonant frequency: 21, 28, 41, 150, 210, 315 kHz. Force constant: 0.30, 0.35, 0.65, 4.50, 7.50, 14.00 N/m. Cantilever thickness and width: 2 microns thick by 35 microns wide. Cantilever lengths: 350, 300, 250, 130, 110, and 190 microns. Websites: www.spmtips.com, www.micromasch.com, www.siliconmdt.com. Distributed in
-
-

the USA by K-TEK International, 7086 S.W. Beveland Street, Portland, Oregon 97223. Website: www.kteintl.com. Tel: (503) 624-0315. See brochure [\[cached\]](#).

[g] MicroMasch (Silicon-MDT, Moscow, Russia) tungsten-carbide conductive coatings for silicon cantilevers: An ultra-thin (2 - 25 nm) film is pulsed plasma deposited on the probe tips. The probes are then annealed to form the final tungsten-carbide (W_2C) films. The rated hardness is 18-20 GPa with a melting point of 3028 degrees Celsius. See brochure [\[cached\]](#).

[h] Thermomicroscopes model 1615-00 scanning thermal probes: 5 micron diameter wire core of 90%/10% Pt/Rh alloy with a temperature coefficient of resistance of 0.00165 per Kelvin and 2.1 Ohm nominal. 5 N/m spring constant. See brochure [\[cached\]](#).

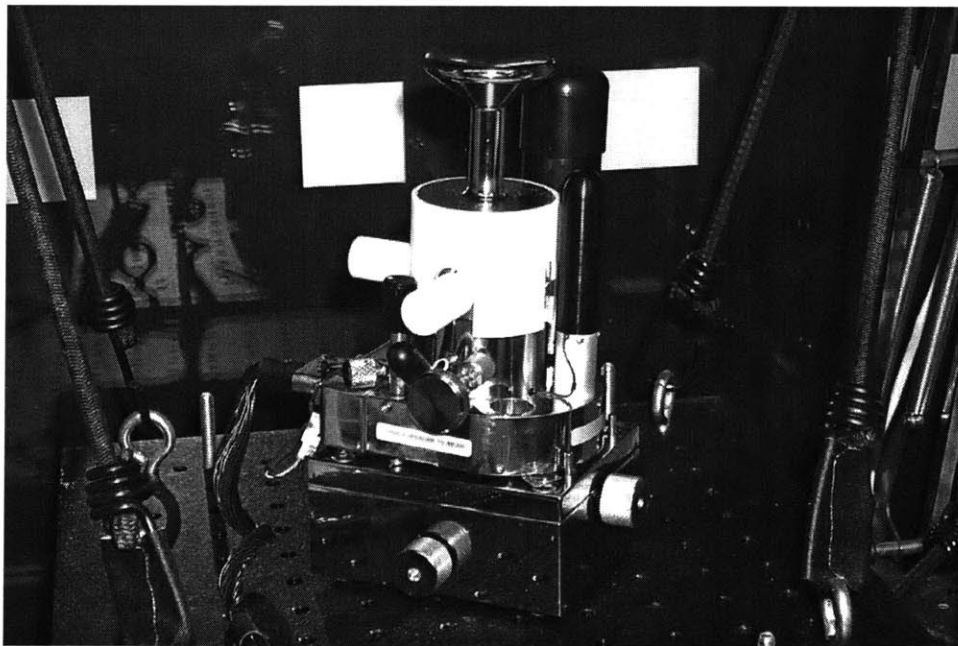


Figure 22 --- Scanning "head" assembly of the Thermomicroscopes Explorer AFM system. The "first" bungee-cord design for a vibration isolation stage is shown here.

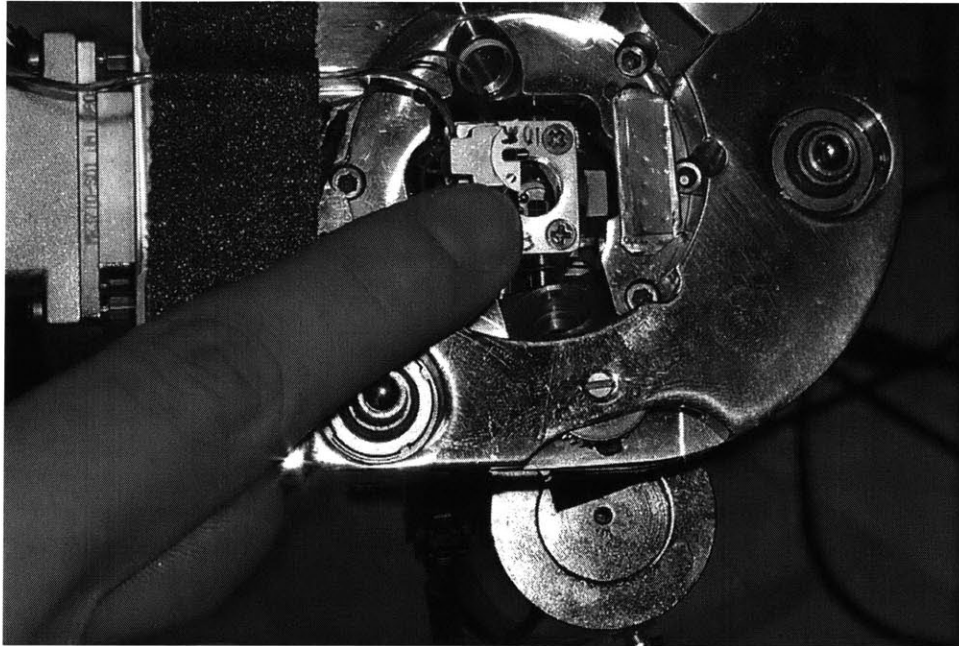


Figure 23 --- The under side of the scanning head of the Explorer AFM system. The finger is pointing at a cantilever-style probe used for AFM imaging.

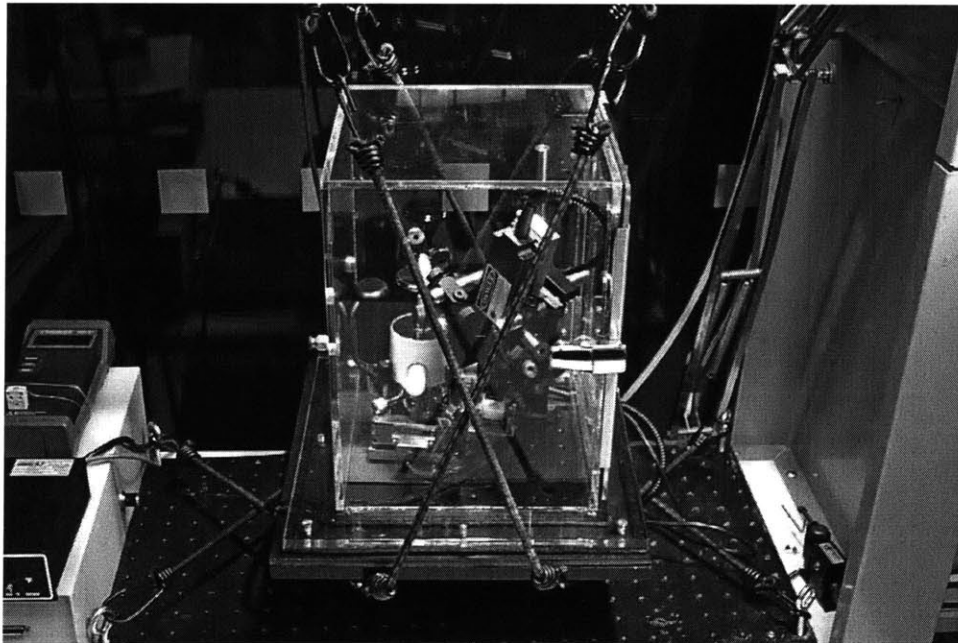


Figure 24 --- The AFM head is placed inside a clear plastic environmental chamber that is supported on a bungee-cord vibration isolation stage. The environmental chamber enables the control of relative humidity, gaseous composition, and temperature. The "second" bungee-cord design for a vibration isolation stage is shown here.

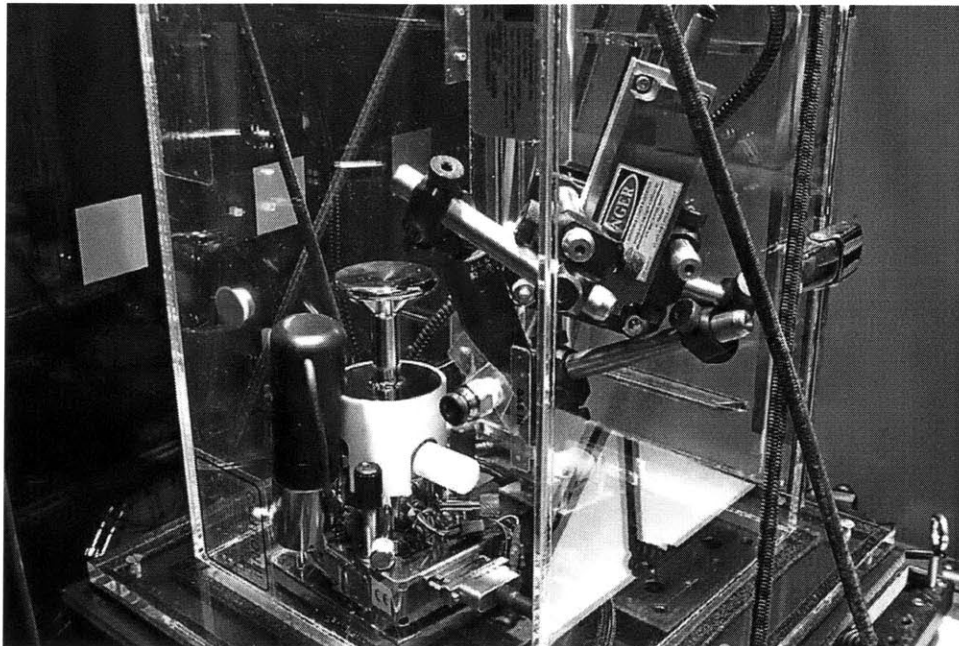


Figure 25 --- A close-up view of the AFM scanning head inside the bungee cord supported environmental chamber. The laser apparatus for thermal-assisted curing of nanoassembled structures is visible in the upper right corner of the chamber.

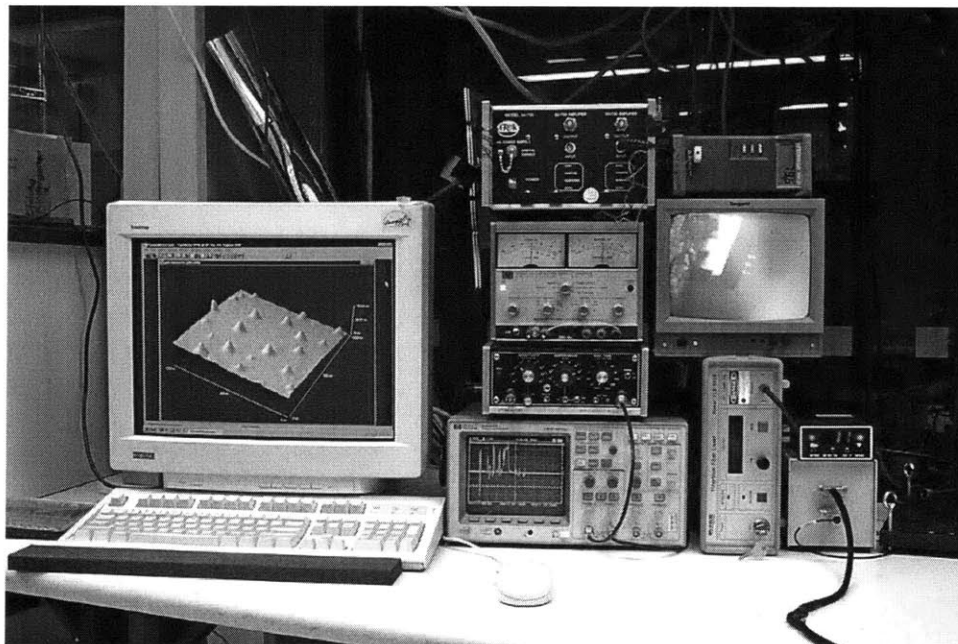


Figure 26 --- The desktop setup for the NanoAssembly system comprises a number of monitor and control devices including a computer screen, laser control system, peltier amplifier, humidity/temperature monitor, e-beam emitter amps, and CCD microscope.

NANOASSEMBLER: SOFTWARE

Motives for a custom software tool

Before a conventional AFM image of a surface can be obtained, there are a host of control parameters that must be specified to execute a successful scanning operation. Included among these are the contact or tapping mode of the cantilever-style probe, the setpoint or force that is applied by the cantilever and tip to the surface, the parameters that control the response time and dynamic behavior of the piezo-mechanical feedback loop, the drive frequency and amplitude used to excite the vibrating cantilever, and the X-Y raster scanning speed and resolution. Proper selection of the best settings for these parameters are largely dependent on the topography and morphology of the scanned surface, the dynamic response and geometry of the scanning tip, user-available time (and patience!), the size of the scan, and a range of environmental conditions such as humidity, mechanical noise, thermal drift rates, and temperature fluctuations. The complexity of the operations increases dramatically when the AFM probe is used as a high-resolution nanoassembly tool, wherein the tip is intentionally maneuvered to apply controlled forces and patterns to a substrate. In the research presented here, a cantilever-style probe was used to extract a miniscule volume of ink from a reservoir and then deposit a desired pattern of the ink onto a substrate. The complexity of such dip-and-write operations at the nanometer scale can be appreciated when one considers the variety of feedback controls and parameters called into action when a human hand manipulates a macroscopic writing instrument, such as an absorbent paint brush, to deposit simple patterns of ink onto a piece of paper. The hand writing process generally becomes extremely unreliable and unforgiving, requiring even more finely tuned controls, when a hard, sharply pointed, non-absorbent device, such as a sewing needle, is used as the dipping and writing instrument. In this case, the sewing needle is macroscopically analogous to the nano-scale sharp tip at the end of an AFM cantilever. All of the control parameters used in conventional AFM imaging operations must also be operative for AFM-assisted pick-and-place nanoassembly procedures, with the simultaneous inclusion of many new and important considerations. For example, new parameters and function calls are needed to control the vertical decent and ascent rates of the tip, switching means between “in-feedback” and “out-of-feedback” states, maximum impulse delivered by the tip to the surface at the point of impact, dwell times and delays, retraction modes, dynamic resonance frequency measurement and modification, and tip-to-reservoir 'ripple' behavior. All of these new terms will be discussed in the following sections.

At the time that this project was undertaken, there was only one lithography software program [a] for the Thermomicroscopes Explorer AFM system on the market.

Unfortunately, this software was suitable for only three types of AFM lithography processes, and all three were restricted to contact mode operations: voltage-initiated surface oxidation, scratching with constant force, and scratching with constant depth. In addition, the software only supported graphical specification of lithography patterns (GUI), without means for modification of scripts or function calls. The complexity of the operations envisioned to achieve the goal of true pick-and-place nanoassembly necessitated that we develop our own custom software package.

'LithoLab' custom nanoassembly software

The Thermomicroscopes Explorer system featured an open architecture software development environment, which made the system particularly attractive for the creation of a custom nanoassembly software package. The SPMTTools development environment, which ran on a Microsoft Windows NT platform, used a Windows Device Driver to drive the DSP hardware and a set of higher level Windows DLLs (Dynamically Loadable Libraries) which provided a set of basic scanning probe functions. Using Microsoft Visual Basic as an editing environment, Aggelos Bletsas of the MIT Media Lab 'Physics and Media Group' created a custom software interface called "LithoLab", which enabled the automated execution of scripted nanoassembly operations. The development of LithoLab required a deep understanding of the software-hardware interactions at the most fundamental level. The manufacturer's documentation of the SPMTTools environment was thorough and substantial. But as can be expected with a system of this level of complexity, there were legacy software problems and hardware incompatibilities that arose almost immediately. From a programming perspective, a great deal of "other people's mess" had to be cleaned up before substantial progress could be made. When required, Thermomicroscopes' Dr. Tim Wong, who wrote much of the Explorer's original imaging software, provided some assistance for resolving particularly dicey issues. Because of the extra hardware element involved, the coding-debugging cycle was substantially longer than the cycle for conventional computer programming. A new set of codes would often appear satisfactory and pass every on-screen debugging test. But when the codes were actually used to drive the physical hardware, the unexpected results, when they occurred, often ranged from unsatisfactory to catastrophic.

Once matured and thoroughly debugged, LithoLab provided a platform for the scripted execution of over 50 custom nanoassembly function calls, each of which consisted of a string of lower level API hardware commands. Most of these functions calls provided real time on-screen output of operational parameters, so that scripts could be monitored for coherence to expected performance levels and terminated when necessary. The on-screen data stream [Figure 27] was often collected and stored for post-run analysis and archiving. LithoLab also provided in-situ AFM imaging of the structures fabricated by

the nanoassembly process as a means of rapid verification of successful script execution. Due to the modular construction of the software interface, new function calls and capabilities could be added without altering the pre-existing codes. We suggest that LithoLab can be further improved by the incorporation of scripted iteration structures, such as 'if-then loops' and 'for loops'. These iteration structures would be useful for the instantaneous modification of parameters in the middle of a nanoassembly run to accommodate an unanticipated event such as a sudden change in cantilever resonance frequency or the alteration of tip sharpness.

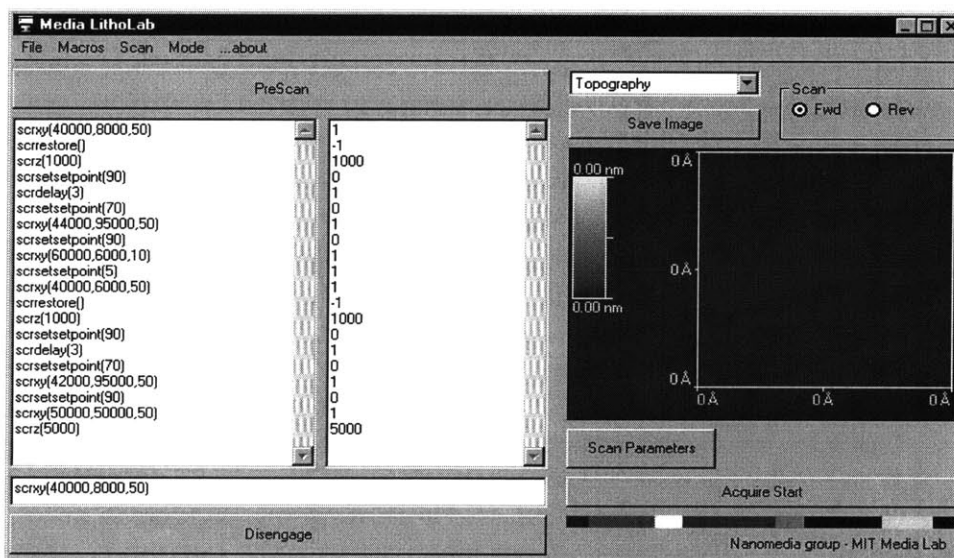


Figure 27 --- The computer screen interface for the custom "LithoLab" nanoassembly software program. Real time function calls and parameters are displayed.

Custom nanoassembly function calls

Numerous custom function calls were created to address the unique requirements of the nanoassembly method. Long strings of these function calls were assembled into text files to form the scripts that directed the operation of the AFM system during automated nanoassembly runs. Table 2 introduces the most common function calls, along with a short description of their proper implementation. Table 3 describes a few additional function calls that are likely to be useful for future work, while the function calls contained in Table 4 are not generally recommended. And finally, Table 5 provides a condensed list of simple function calls that were rarely used on their own, but instead were often incorporated as sub-commands within other more complex function calls.

Table 2 --- Most commonly used function calls in nanoassembly scripts

| function | application, usage, and special notes |
|--------------------------|--|
| scrncon() | activates tapping (non-contact) mode; tip oscillation begins |
| scrncoff2() | de-activates tapping (non-contact) mode; tip oscillation stops and de-activation is indicated in the non-contact mode menu |
| scrzz(a) | can only be used BEFORE tip approach: engagement occurs at 'a' nm below the full lift-up point (range is 0 nm [tip high] to 9000 nm [tip low]); this function call contains a combination of the less commonly used scrz() and scrrestore() commands |
| scroscf() | executes a 5-second long frequency sweep and tuning operation for tapping mode; maximizes the amplitude of cantilever oscillation; is usually quite accurate |
| scrsetTBref() | sets the current cantilever deflection signal (T-B) value as the new 100% setpoint value; is usually implemented after a scroscf() command; for tapping mode only |
| scrsetpid(a,b,c) | sets the PID feedback (a = proportional, b = integral, c = derivative) parameters; if 'a' is low (~0.01), the z-piezo controlling the tip reacts very slowly; if 'a' is high (~0.30), the z-piezo reacts more quickly |
| scrsetsetpoint(a) | sets the tip force setpoint to 'a' nanoamps in contact mode or 'a' % for tapping mode; scrsetsetpoint(-60) is used to lift up and disengage the tip from the surface in contact mode only |
| scrsetsp(a) | scrsetsp(-60) is used to lift up and disengage the tip from the surface in tapping mode only |
| scrtipapproach() | causes the tip to engage the surface and apply a force defined by the most recently executed scrsetsetpoint() command |
| scrdelay(a) | creates a pause in the running script that is 'a' seconds long |
| scrbinfeedback() | checks that the tip is engaged and with the surface; outputs '1' for engaged and '-1' for not-engaged |
| scrfeedbackz() | outputs the z-piezo position in nanometers (range is about 0 to 9000 nm) to the computer screen |
| scrxy(a,b,c) | causes the x- and y-piezoes to translate the tip to the specified x,y coordinates (a is 0<x<100000 nanometers; b is 0<y<100000 nanometers) with a translation speed of 'c' micrometers per second |

| | |
|------------------------|---|
| scr10out1(a,b) | causes a signal of 'a' volts ($-10 < a < +10$) to be output from I/O-10 board BNC #1 for 'b' milliseconds |
| scrmovetipup(0) | directs the tip to disengage from the surface; the z-motor runs for the default number of milliseconds specified within a computer file called "stages.ini" under the section designated as "ZMotorDisengageTime" |
| scral_on() | activates the output of an electronic signal corresponding to the magnitude of the cantilever deflection signal (T-B) through the I/O-10 board BNC connector |
| scral_off() | de-activates the output of the cantilever deflection signal (T-B) through the I/O-10 board BNC connector |

Table 3 --- Functions calls that may useful for future work

| function | application, usage, and special notes |
|-------------------------|---|
| scrdisengage(a) | directs the tip to disengage from the surface by causing the z-motor to run for 'a' microseconds ($0 < a < 2000000$); the motor speed (in volts) is specified and can be modified within a computer file called "stages.ini" under the section designated as "ZMotorStandard" |
| scrsetdrive(a) | directly sets the tapping mode oscillation drive amplitude 'a' in volts |
| scrncf(a) | directly sets the tapping mode frequency 'a' in hertz |
| scrsetrelfreq(a) | changes the tapping mode oscillation frequency by 'a' hertz up or down from the current oscillation frequency |

Table 4 --- Functions calls used in early scripts, but are not generally recommended

| function | application, usage, and special notes |
|-------------------|--|
| scrscsp(a) | changes the force setpoint to be 'a' nano-amps (nA) above the previous setpoint setting; because the new setpoint is cumulatively added to the previous setpoint, multiple executions of this function call can cause errors in the force applied by the tip to the surface; this function call is used to force the tip to engage the surface after the standard tip approach procedures have failed (i.e. the tip pops up again after briefly touching the surface during the tip approach); for contact mode only |

| | |
|-------------------|--|
| scroscf2() | executes a 2-second long rough and fine frequency sweep and tuning operation for tapping mode; maximizes the amplitude of cantilever oscillation; is usually not very accurate |
| scrz(a) | this function call can cause the tip to crash into the surface in both contact and tapping modes when employed AFTER tip approach |
| scrzz(a) | this function call can cause the tip to crash into the surface in both contact and tapping modes when employed AFTER tip approach |

Table 5 --- Simple function calls that are incorporated into other more complex function calls

| | | |
|---------------------------------|----------------------------|----------------------|
| scrncoff() | scrgetwalkerstep() | scrdokimi() |
| scrlinescan() | scrsetwalkerstep(a) | scrbcnc() |
| scrsetscanspeed(a) | scrgetzvr() | scrtipap() |
| scrgetscanrange() | scrgetzv() | scrrestore() |
| scrgetsetpointlimits() | scrgetsp() | scrrestore2() |
| scrgetfeedbackchannel() | scrvolttoz(a) | scrgetpid() |
| scrsetfeedbackchannel(a) | scrztovolt(a) | scrhf() |
| scrADCmux(a,b) | scrzvoltrange() | screxit |

Nanoassembly scripts

More than 160 nanoassembly scripts were composed for the automated fabrication of nano-scale structures and patterns. At the most basic level, the scripts were comprised of function calls which executed a series of repetitive tip "dip" and tip "lift" operations. Here, the term tip 'dip' is used as a general reference to the action of lowering the tip with the Z-piezo to cause the tip to make contact with some underlying surface. The tip 'dip' operation was utilized for both inking and deposition steps. As expected, a tip 'dip' action was almost always followed by a tip 'lift' action. As shown in Table 6, different function calls were used to execute a dipping or lifting procedure depending on the contact or tapping mode specified within the script.

Table 6 --- Tip dip and tip lift function calls

| | contact mode | tapping mode |
|--------------------|--|--|
| tip dipping | scrsetsetpoint(a) [where 'a' is about 6 nA] | scrsetsetpoint(a) [where 'a' is about 50%] |
| | notes on alternative function calls: scrsetsp(a) works nearly identically to the recommended scrsetsetpoint(a) command; scrscsp(a) also works, but should not be used because it cumulatively adds the value 'a' to the current setpoint value which causes the force on the tip to add up quickly | notes on alternative function calls: the scrsetsp(a) function call generally crashes the tip into the surface for any number 'a', and should not be used; the scrscsp(a) function call is inactive when the tapping mode is turned on, and therefore can not be used in tapping mode |
| tip lifting | scrsetsetpoint(-60) | scrsetsp(-60) |
| | notes on alternative function calls: scrsetsp(-60) works nearly identically to the recommended scrsetsetpoint(-60) | notes on alternative function calls: scrsetsetpoint(-60) does not work in tapping mode |
| other | scrz(a) and scrzz() should not be used for dipping and lifting procedures because this often results in a crash for some tip designs; however these commands can be used for setting the Z-axis piezo elevation before the tip approach and engagement steps in a typical script | |

Although not always the case, most nanoassembly scripts were comprised of three main sections: (1) tip engagement, (2) fabrication, and (3) tip disengagement. A concise summary of the most common function calls in the order that they generally appeared within the scripts is presented in Table 7.

The first section of a script, as detailed in Table 8, contained function calls that prepared the tip to engage the surface. These “tip engagement” function calls activated the contact or tapping modes of operation and the real-time monitoring of cantilever deflection via an external oscilloscope. Other preparatory functions were used to set the proper Z-piezo elevation, tip force, and engagement PID feedback parameters. Additional functions calls initiated the tip approach, tip-surface engagement, and tip retraction procedures.

The second section of a typical script, as presented in Table 9, contained a long series of repetitive actions that were actually responsible for the nanoassembly fabrication

processes. The procedures outlined in the table provide a simplified template for only a single tip dipping and tip lifting cycle. It should be noted that the deposition of even a single dot of material onto a substrate always required at least two complete cycles of these dipping and lifting operations ---- one dip-lift cycle for “inking” the tip in the ink reservoir, and a second dip-lift cycle for depositing the adhered ink onto the substrate. If an optional "scratch pad" technique was employed, in which a dip into the ink reservoir was followed by more than one deposition step for the purpose of forming very high-resolution structures, additional dip-lift cycles were added to the script. The dip-lift cycle template presented in Table 9 can accommodate a wide selection and ordering of procedures for dot and line formation, dynamic tuning of the cantilever resonance frequency, alteration of PID feedback control parameters, the setting of tip-surface interaction forces and velocities, and the output of external control signals. In addition, several curing techniques, such as local electron beam curing and global infrared laser curing, can be implemented before, during, or after the tip dipping step. Depending on the number of individual nano-structures formed during a nanoassembly run, a script often incorporated tens to hundreds of tip dipping and lifting cycles.

The third and final component of a typical script contained a series of function calls that controlled the tip disengagement, parking, and shutdown operations at the conclusion of a nanoassembly run, as shown in Table 10.

Table 7 --- Overview of the three main sections of a typical nanoassembly script: (1) tip engagement, (2) fabrication, and (3) tip disengagement. The function calls are presented in the order that they would generally appear within a script.

| engagement operations | function call |
|---------------------------------|---------------------------------|
| pre-run operations | scral_on() |
| | scrncoff2() OR scrncon() |
| prepare for tip approach | scrzz(a) |
| | scrsetpid(a,b,c) |
| | scrxy(a,b,c) |
| | scrdelay(a) |
| | scrsetsetpoint(a) |

| | |
|---------------------|---|
| tip approach | scrtipapproach() |
| | scrdelay(a) |
| tip lift up | scrsetsetpoint(-60) OR scrsetsp(-60) |
| | scrdelay(a) |

| fabrication operations | function call |
|------------------------------------|---|
| move tip to dipping zone | scrxy(a,b,c) |
| | scrdelay(a) |
| preparation for dip | scrsetpid(a,b,c) |
| | scroscf() |
| | scrsetTBref() |
| pre-dip local cure | scr10out1(a,b) |
| activate the dipping action | scrsetsetpoint(a) |
| | scrdelay(a) |
| | scrsetsetpoint(a) |
| | scrdelay(a) |
| | scrfeedbackz() |
| activate linear drag | scrxy(a,b,c) |
| mid-dip local cure | scr10out1(a,b) |
| tip lift up | scrsetsetpoint(-60) OR scrsetsp(-60) |
| | scrdelay(a) |

| | |
|------------------------------|-----------------------|
| post-lift local cure | scr10out1(a,b) |
| post-lift global cure | scrxy(a,b,c) |
| | scr10out1(a,b) |

| disengagement operations | function call |
|---------------------------------|---------------------------------|
| tip lift up | scrmovetipup(0) |
| parking procedures | scrxy(a,b,c) |
| | scrsetsetpoint(a) |
| | scrncoff2() OR scrncon() |
| | scral_off() |

Table 8 --- Nanoassembly script section #1: pre-run & tip approach operations

| process | line number, function call & action description | | |
|---------------------------------|--|--|---|
| pre-run operations | A | scral_on() | activates the "analog out" signal for the monitoring of cantilever deflection (which can be viewed in real time on an oscilloscope) |
| | B | scrncoff2() OR scrncon() | use scrncoff2() to activate contact mode, OR use scrncon() to activate non-contact mode (tapping mode) alternative option: scrncoff2() can be used, but how this function differs from scrncoff() is unknown |
| prepare for tip approach | C | scrzz(a) | adjusts the height of the z-piezo so that the tip-surface engagement is set to occur 'a' nm below the full lift-up elevation (range is 0 nm [high] to 9000 nm [low]); typically 'a'=7000 nm |
| | D | scrsetpid(a,b,c) | sets the PID feedback parameters |

| | | | |
|---------------------|---|--|---|
| | E | scrxy(a,b,c) | moves the tip to an x-y position suitable for the manual alignment of the tip relative to the ink reservoir |
| | F | scrdelay(a) | provides the time delay for the manual alignment of the tip relative to the ink reservoir |
| | G | scrsetsetpoint(a) | sets the tip-surface force at the point of engagement for both contact and tapping modes |
| tip approach | H | scrtipapproach() | activates tip engagement with the surface at position x,y=50000,50000 |
| | I | scrdelay(a) | provides an optional time delay after tip-surface engagement is complete |
| tip lift up | J | scrsetsetpoint(-60) OR scrsetsp(-60) | <p>activates the tip lift-up action; use scrsetpoint(-60) for contact mode, OR use scrsetsp(-60) for tapping mode</p> <p>alternative option 1: scrscsp(-60) works for contact mode only, but is not recommended because this function call cumulatively adds '-60' to the current setpoint value</p> <p>alternative option 2: scrzz(a) can be used in either contact or tapping mode for non-feedback lifts, but often causes crashes</p> <p>alternative option 3: scrsetpid(0,0,0) will lift up the tip in tapping mode, but can crash the tip in contact mode</p> |
| | K | scrdelay(a) | provides the delay time necessary to allow the tip fully lift up; the minimum delay time is dependent on the feedback PID setting (a higher 'I' integral number causes a quicker lift, which requires a shorter delay time) |

Table 9 --- Nanoassembly script section #2: fabrication operations (only one tip "dip-lift" cycle is shown)

| process | line number, function call & action description | | |
|------------------------------------|--|--------------------------|--|
| move tip to dipping zone | 1 a | scrxy(a,b,c) | moves the tip to hover over the dipping zone |
| | 1 b | scrdelay(a) | optional time delay for completing the tip translation |
| preparation for dip | 1 c | scrsetpid(a,b,c) | optional change of PID settings for the upcoming dip |
| | 1 d | scroscf() | optional 5-second long cantilever resonance frequency tuning operation (tapping mode only) alternative option: scroscf2() requires only 2 seconds to perform a rough and fine frequency tuning, but is far less accurate (tapping mode only) |
| | 1 e | scrsetTBref() | sets the current T-B signal value (as a result of previous frequency retuning) as the 100% setpoint (zero force) value for tapping mode |
| pre-dip local cure | 1f | scr10out1(a,b) | optional activation/de-activation of local curing processes (e-beam, thermal) located on or near the tip while the tip is hovering just over the surface |
| activate the dipping action | 1 g | scrsetsetpoint(a) | activates the dipping operation with a specified force for both contact and tapping modes alternative option 1: scrmsp(-60) works for contact mode only, but is not recommended because this function cumulatively adds 'a' to the current setpoint value alternative option 2: scrz(a) or scrzz(a) sets the z-piezo elevation to a constant height with feedback off, but often causes the tip to crash alternative option 3: scrsetpid(a,b,c) when immediately preceded by scrsetpid(0,0,0) and scrsetsetpoint(a) [in that order], can also be used to execute a dipping action |

| | | | |
|-----------------------------|--------|---|--|
| | 1 h | scrdelay(a) | provides the delay time necessary to allow the tip to dip and fully contact the surface; the minimum delay time is dependent on the feedback PID setting (a higher 'I' integral number causes a quicker dip, which requires a shorter delay time) |
| | 1i | scrsetsetpoint(a) | optional second stage to the dip; helps to protect the tip from bearing the full force of impact on the first stage of the dip |
| | 1j | scrdelay(a) | optional time delay for the optional second stage of the dip |
| | 1 k | scrfeedbackz() | optional real time monitor of z-piezo position on the computer screen; 0 nm is all the way up, ~9000 nm is down |
| activate linear drag | 1l | scrxy(a,b,c) | optional linear movement to drag the tip in the ink pool or to deposit a line of ink at the construction zone on the substrate |
| mid-dip local cure | 1 m | scr10out1(a,b) | optional activation/de-activation local curing processes (e-beam, thermal) located on or near the tip while the tip is in direct contact with the surface |
| tip lift up | 1 n | scrsetsetpoint(-60) OR scrsetsp(-60) | <p>activates the tip lift-up action; use scrsetpoint(-60) for contact mode, OR use scrsetsp(-60) for tapping mode</p> <p>alternative option 1: scrzsp(-60) works for contact mode only, but is not recommended because this function call cumulatively adds '-60' to the current setpoint value</p> <p>alternative option 2: scrzz(a) can be used in either contact or tapping mode for non-feedback lifts, but often causes crashes</p> <p>alternative option 3: scrsetpid(0,0,0) will lift up the tip in tapping mode, but can crash the tip in contact mode</p> |
| | 1 o | scrdelay(a) | provides the delay time necessary to allow the tip fully lift up; the minimum delay time is dependent on the feedback PID setting (a higher 'I' integral number causes a quicker lift, which requires a shorter delay time) |

| | | | |
|----------------------------------|--------|-----------------------|---|
| post-lift local cure | 1 p | scr10out1(a,b) | optional activation/de-activation of local curing processes (e-beam, thermal) located on or near the tip while the tip is hovering just over the surface |
| post-lift global cure | 1 q | scrxy(a,b,c) | moves the tip out of the way to allow laser or other global curing processes to proceed unobstructed by the cantilever |
| | 1 r | scr10out1(a,b) | optional activation/de-activation of global curing (laser, peltier); when using the laser shutter, this function call is followed by a scr10out1(-a,b) command to close the shutter |

Table 10 --- Nanoassembly script section #3: tip disengagement and parking operations

| process | line number, function call & action description | | |
|--------------------------------|--|--|---|
| tip dis- engagement | V | scrmovetipup(0) | activates tip disengagement from the surface |
| parking procedures | W | scrxy(a,b,c) | moves the tip to a specified parking location |
| | X | scrsetsetpoint(a) | sets the force setpoint value in anticipation of the next nanoassembly run |
| | Y | scrmcoff2() OR scrmcon() | optional: use scrmcoff2() to activate contact mode OR use scrmcon() to activate non-contact mode (tapping mode), in anticipation of the next nanoassembly run |
| | Z | scral_off() | turns off the analog signal for monitoring the cantilever deflection on an external oscilloscope |

Additional considerations: Tip-reservoir alignment & tip engagement

Before running a nanoassembly script, a series of preparatory adjustments, frequency tuning, and manual tip-to-reservoir alignment procedures were undertaken to ensure that the tip would reliably engage the substrate and the ink reservoir using the desired settings. Then a special diagnostics pre-run script was executed to verify proper engagement and retraction of the tip using both the tapping and contact modes. A

summary of the recommended actions is presented in Table 11 and Table 12. When all tests and preparations were complete, a desired nanoassembly script could be run as planned.

Table 11 --- Manual pre-run procedures

| step | manual operation description |
|------|--|
| 1 | apply an elongated oval-shaped ink pool (the reservoir) to the substrate with the end of a metal wire; while the end of the ink-laden wire is contact with the substrate, pull the wire in a direction parallel to the length of the AFM cantilever to form an oval pool |
| 2 | ensure that the "stages.ini" computer file is set so that: ZMotorApproach=0.50 V, ZMotorStandard=5.00 V, ZMotorDisengageTime=25 ms |
| 3 | open the original factory-installed Thermomicroscopes AFM imaging software |
| 4 | adjust the mirror knobs on the side of the AFM head so that: SUM is less than 7 nA, L-R is -0.5 nA, and T-B is -0.5 nA |
| 5 | activate the tapping (non-contact) mode using the imaging software menu |
| 6 | activate the frequency sweep using the imaging software menu; tune the cantilever by selecting the proper oscillation drive (in volts) and frequency which maximizes the oscillation amplitude; make a note of the 100% setpoint T-B value in units of nA |
| 7 | close the Thermomicroscopes AFM imaging software, and open the custom LithoLab nanoassembly software |
| 8 | set the scan size to be 100 microns, to enable unrestricted translation of the tip over a 100x100 region around the AFM tip (note: smaller scan sizes will restrict the maximum translation distance of the tip during a nanoassembly run) |
| 9 | using the AFM head motor and/or manual height-adjustment knobs, lower the head so that the tip is in close proximity (<100 microns) to the surface; the substrate should be positioned so that the tip is hovering just beyond the edge of the ink pool |
| 10 | click the on-screen menu to turn on the AFM head internal laser |
| 11 | check that the L-R and T-B values are still close to -0.5 nA; make adjustments to the mirror knobs on the AFM head if required |
| 12 | using the LithoLab menu, activate the tapping (non-contact) mode |

| | |
|-----------|---|
| 13 | verify that the 100% setpoint T-B value is about the same as what was noted previously when using the factory-installed Thermomicroscopes AFM imaging software; the proper oscillation drive voltage should have been automatically recalled by the software; type in and execute a <code>scroscf()</code> command, which retunes the cantilever, if changes to the resonant frequency are required |
| 14 | load and run the custom tip engagement verification script file called "code161.txt"; see Table 12 for a view of this script |
| 15 | while the code is running, ensure that the tip successfully engaged and lifted up off the surface twice (once in tapping mode, and one in contact mode) |
| 16 | verify that the on-screen displayed output for the two <code>scrbinfeedback()</code> and <code>scrfeedbackz()</code> commands were "1" and approximately "7000", respectively |
| 17 | during the 10-second delay included near the end of the script, use the X-Y knobs on the substrate positioning stage to move the substrate so that the edge of ink pool lies just out of reach of the hovering tip (the extreme end of the tip must be less than 50 microns away from the edge of the ink pool), as observed through the AFM head's CCD camera |

Table 12 --- Code for ensuring proper tip engagement and ink pool alignment in tapping mode and contact mode at force setpoints of 40% and 6 nA, respectively (code161.txt)

| step | automated scripted function calls |
|---|--|
| pre-run parameter settings | <code>scral_on()</code> |
| | <code>scrsetpid(1,0.30,0)</code> |
| | <code>scrzz(7000)</code> |
| TAPPING MODE tip approach, engagement, and disengagement | <code>scrncon()</code> |
| | <code>scrxy(50000,50000,500)</code> |
| | <code>scrsetsetpoint(40)</code> |
| | <code>scrtipapproach()</code> |
| | <code>scrdelay(3)</code> |
| | <code>scrbinfeedback()</code> |
| | <code>scrfeedbackz()</code> |

| | |
|--|-------------------------|
| | scrsetsp(-60) |
| | scrdelay(3) |
| | scrmovetipup(0) |
| | scrsetsetpoint(40) |
| <p style="text-align: center;">CONTACT MODE</p> <p style="text-align: center;">tip approach, engagement, and disengagement</p> | scrncoff2() |
| | scrxy(50000,50000,500) |
| | scrsetsetpoint(6) |
| | scrtipapproach() |
| | scrdelay(3) |
| | scrbinfeedback() |
| | scrfeedbackz() |
| | scrsetsetpoint(-60) |
| | scrdelay(3) |
| <p style="text-align: center;">manual alignment of the edge of the ink pool relative to the end of the tip during a 10-second time delay; the edge of the ink pool must be less than 50 microns away from the tip</p> | scrxy(50000,100000,500) |
| | scrdelay(10) |
| | scrxy(50000,50000,500) |
| | scrdelay(2) |
| | scrmovetipup(0) |
| | scrsetsetpoint(6) |
| | scral_off() |

'LithoLab' Intelligent Scripting Assistant

There was a vast collection of control parameters and variables [Figure 28] that needed to be considered for the successful execution of even the simplest pick-and-place nanoassembly operations. Because of this inherent complexity, the creation of scripts from scratch for each new experiment was overly tedious, even with the aid of templates. Therefore, we developed an expert software system, called the LithoLab ISA (Intelligent Scripting Assistant), which automatically generated scripts that satisfied a set of user-defined requirements [Figure 29] [Figure 30]. The LithoLab ISA proposed the appropriate type and sequence of actions that generated the desired nano-scale pattern, while at the same time accommodating a range of requirements such as pattern geometry preferences (line width and aspect ratio), ink specifications (solid loading, viscosity, evaporation rate, and phase), and apparatus information (cantilever spring constant, tip sharpness, and substrate temperature).

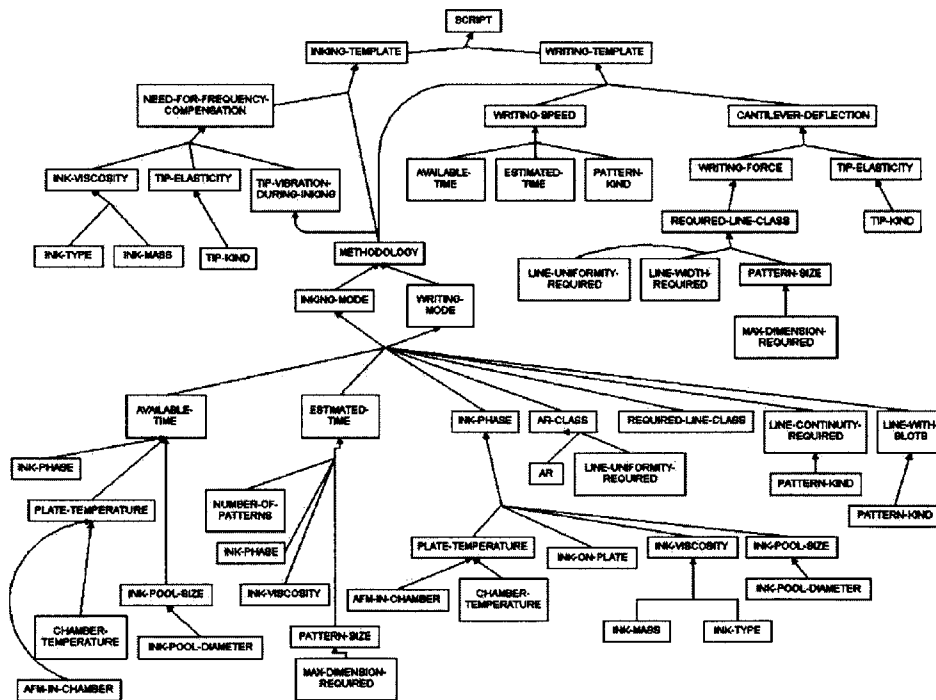


Figure 28 --- Summary of the knowledge base, control parameters, and variables required to carry out a typical set of nanoassembly operations.

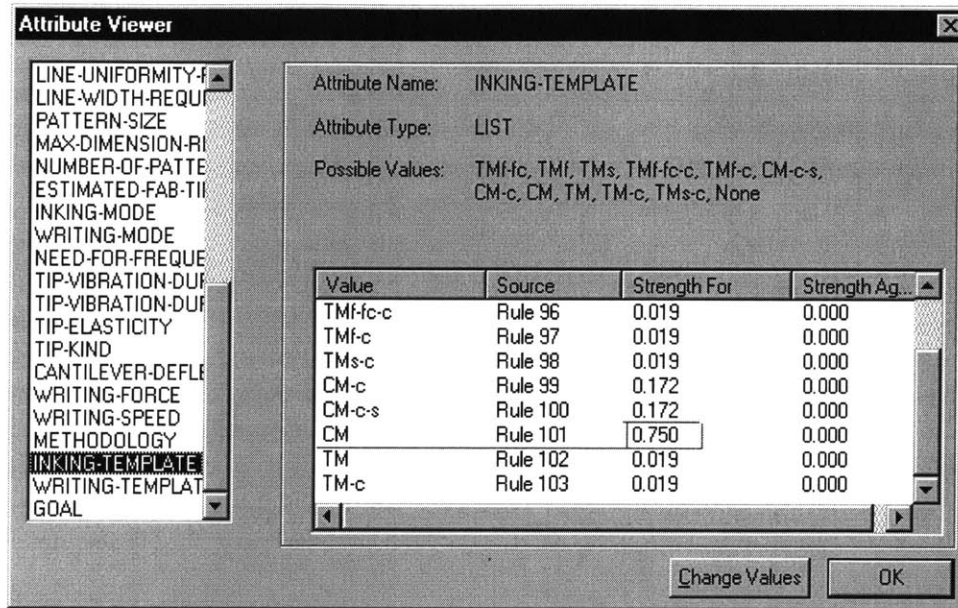


Figure 29 --- LithoLab ISA (Intelligent Scripting Assistant) inking procedure template. In this case, the ISA suggested an inking template lithography script designated as "CM" with a 75% goodness match to the user-specified requirements.

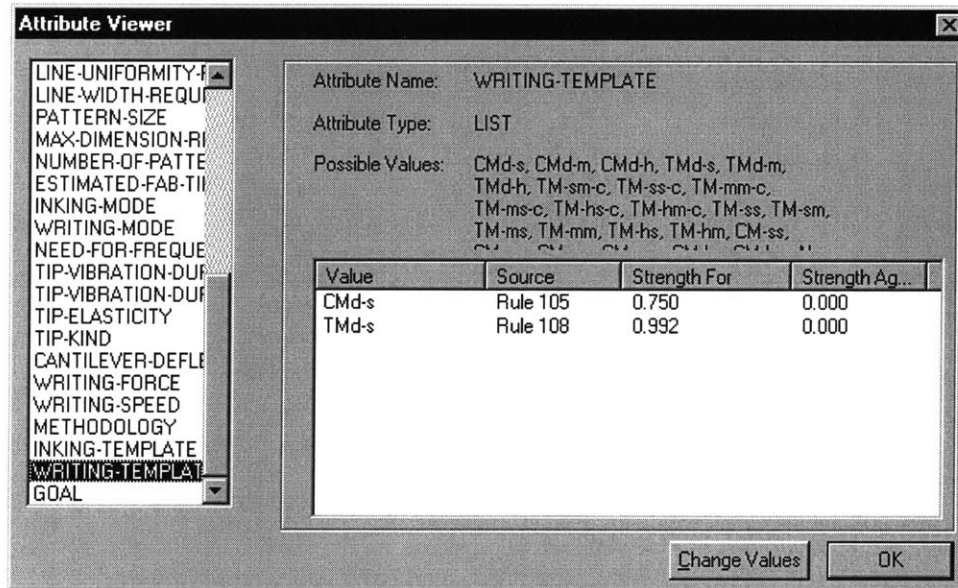


Figure 30 --- LithoLab ISA writing procedure template. In this case, the ISA suggested a writing template script designated as "TMD-s" with a 99% goodness match to the user-specified requirements.

The utility and operation of the LithoLab ISA can be illustrated by consideration of the following scenario. Suppose that a ‘user’ needs a nanoassembly script that enables the fabrication of three nano-scale parallel lines using tapping mode operations at room temperature. The user desires that these lines be 1 micron long and 80 nm wide, with a height-to-width aspect ratio of 50%. In addition, the build material is specified to be silver ink loaded with 35% metal by weight. The LithoLab ISA now asks the user a series of questions about the most important characteristics of the desired nanoassembled pattern. An example query and response exchange between the Intelligent Scripting Assistant and the user is presented in the following table.

| Sample questions asked by the expert assistant | | User's responses |
|--|--|------------------|
| 1 | What is the material phase of the ink? | Solid |
| 2 | How much time is available for fabrication? | Un-specified |
| 3 | What is the kind of pattern you desire to fabricate? | Line |
| 4 | Is line uniformity an important factor for your pattern? | Yes |
| 5 | What is the desired width of the fabricated lines (in nm)? | 80 |
| 6 | What is the desired height-to-width Aspect Ratio (expressed in percent) of the fabricated lines? | 50 |
| 7 | Would you like blots on your fabricated lines? | No |
| 8 | What is the maximum dimension of the desired pattern (in nm)? | 1000 |
| 9 | Is the total number of desired patterns large or small? | Small |

After some computation, the LithoLab ISA provides an output that is presented on the computer screen. Example screen shots are shown in Figure 29 and Figure 30. Let us assume that the following output is generated:

INKING TEMPLATE: CM-c 1.0
WRITING TEMPLATE: TMd-s 1.0

This rather cryptic message suggests an “inking template” and a “writing template” that best satisfy the user-defined requirements. Each template is composed of a long list of function calls in the proper order. To aid in the interpretation of the templates, LithoLab ISA also generates an easily comprehensible list of the characteristics of the “best match” templates, as shown in the two following tables.

| Example inking template (CM-c) | |
|---------------------------------------|--|
| CM-c | The tip is dipped into the ink pool using the contact mode. |
| | After the ink-laden tip is withdrawn from the ink pool, the tapping mode is switched on. |
| | Re-tuning of the cantilever (to compensate for additional ink on the tip) is optional. |

| Example writing template (TMd-s) | |
|---|---|
| TMd-s | The nanoassembled pattern is composed of dots of ink (instead of lines). |
| | The tip deposits dots of ink using the tapping mode. |
| | Re-tuning the cantilever after the deposition of each dot of ink is not required. |
| | The translation speed of the tip, from the ink pool to the writing area, is “moderate” (to avoid losing registration and precision). |
| | The force applied by the tip to the substrate during the deposition of each dot of ink is set to be 5% less than the force used for conventional AFM imaging. |
| | After each dot of ink is deposited, the contact mode is switched on. |

Glossary of nanolithography modes and methodologies

The tables that follow contain information concerning the various modes of operation and lithography methods handled within the LithoLab ISA software program.

| Inking-Modes | |
|-----------------------|--|
| iTapping-mode-solvent | The cantilever will be vibrating during the inking procedure (Tapping mode). The tip will approach a solid ink pool, after it has dip into a solvent material. |
| iTapping-mode | The cantilever will be vibrating during the inking procedure (Tapping mode). The tip will approach a liquid ink pool. |
| iTapping-mode-flood | The cantilever will be vibrating during the inking procedure (Tapping mode). A flood of the ink pool must be created first, with a fast approach of the tip into the ink pool, so that ink initially will be attached on the tip. After that, for consecutive writing procedures, the tip will dip into one of the smaller liquid pools, created from the initial flood. |
| iContact-mode | The cantilever will dip into the ink pool, with no vibration. |
| iContact-mode-solvent | The cantilever will approach a solvent pool first, with no vibration. Then, the tip will dip without vibration into a solid ink pool. |

| Writing-Modes | |
|-------------------------|---|
| wTapping-mode-dotmatrix | The cantilever will be vibrating during the writing procedure (Tapping mode). The writing unit will be a dot of ink (instead of a whole line). The cantilever will vibrate during writing, depositing material dot-after-dot. |
| wContact-mode-dotmatrix | The writing unit will be a dot of ink (instead of a whole line). The cantilever will NOT vibrate during writing, depositing material dot-after-dot. |
| wTapping-mode-drag | The cantilever will be vibrating during the writing procedure (Tapping mode). The writing unit will be a whole line, instead of a single dot . The cantilever will vibrate during writing, depositing material continuously, in a line trace. |
| wContact-mode-drag | The writing unit will be a whole line, instead of a single dot . The cantilever will NOT vibrate during writing, depositing material continuously, in a line trace. |

| Methodologies | |
|---------------|--|
| CMTMs | iContact-mode-solvent for inking and wTapping-mode-drag for writing. |
| CMTMd | iContact-mode for inking, and wTapping-mode-dotmatrix for writing. |
| CMCMd | iContact-mode for inking and wContact-mode-dotmatrix for writing. |
| TMfTMdg | iTapping-mode-flood for inking and wTapping-mode-drag for writing. |
| TMsTMdg | iTapping-mode-solvent for inking and wTapping-mode-drag for writing. |
| TMfCMdg | iTapping-mode-flood for inking and wContact-mode-drag for writing. |
| TMsCMdg | iTapping-mode-solvent for inking and wContact-mode-drag for writing. |
| TMTMdg | iTapping-mode for inking and wTapping-mode-drag for writing. |
| TMCMdg | iTapping-mode for inking and wContact-mode-drag for writing. |
| CMTMdg | iContact-mode for inking and wTapping-mode-drag for writing. |

[a] Paul Bucher Company: TopoLith lithography software for the Explorer scanning probe microscope system. Approximately \$5000 USD. Address: Schutzengraben 7, 4051 Basel, Switzerland. Tel: +41 61 269 1111 , www.bucher.ch/topolith.htm

2D NANOASSEMBLY

Fabrication of dots with liquid-phase inks

Operating under the control of a scripted series of commands within a custom lithography software program, the Pick-and-Place NanoAssembly system uses a sharp tip on the end of a silicon cantilever to transfer liquid ink from an ink reservoir to a substrate [Figure 31]. A dot of ink is the simplest structure that can be fabricated. A typical dot deposition procedure involves the following major steps: (1) dipping the tip into a reservoir of ink; (2) withdrawing the tip from the reservoir, with a small quantity of ink material adhering to the tip; (3) high speed elevated translation of the tip to the deposition zone at a height of several microns above the surface of the substrate; (4) engagement of the tip with the substrate to deposit the adhered ink material in the form of a dot of ink; (5) lift-off of the tip from the surface; and (6) high speed elevated translation of the tip back to the ink reservoir. In general, this complete cycle of steps is repeated once for every dot that is deposited at a frequency of about 1 cycle per second. The volume of liquid transferred to the substrate via a single dot is usually so small that special procedures must be undertaken to generate dots that are comparable in size to those deposited by more conventional technologies. For example, the NanoAssembly system, when using a specially dulled tip and highly viscous inks, requires a hundred or more deposition cycles to create a liquid dot with a diameter of 10 microns on a non-absorbent substrate. For comparison, the highest resolution piezo ink jet print head [a] can currently deliver a droplet with a volume of 3 picoliters to generate a dot with a diameter of 33 microns onto an absorbent substrate. Mechanical microspotting, a technique used to deposit small quantities of fluids for the fabrication biological devices such as gene chips, creates dots that are generally 50 microns across or larger.

The size of the dot deposited by the NanoAssembly system can be minimized by adjusting a number of key variables including the following: (1) the sharpness or dullness of the tip; (2) the maximum force applied by the tip to the substrate at the point when the dot is deposited; (3) the viscosity, mass loading, vapor pressure, and other material properties of the ink; and (4) the tapping (vibrating) mode or contact (non-vibrating) mode of the cantilever when dipping the tip into the ink reservoir, and when engaging the tip with the substrate to deposit a dot of ink. As expected, a tip with a smaller radius of curvature at its extreme end can generally deliver a smaller sized dot to the substrate. Decreasing the force applied by the tip to the substrate while using either contact mode [Figure 32] or tapping mode also decreases the size of the deposited dot, and the effect is particularly observable for multi-layer dots [Figure 33].

For liquid-phase inks, a reduction in dot size can be achieved by choosing an ink that exhibits lower viscosity. Much of the research presented here was focused on the deposition of silver nanoparticle and gold nanoparticle inks, which contained both solid and solvent fractions. The viscosity of the nanoparticle inks was reduced by mixing additional fractions of solvent into the ink. An experiment was conducted wherein two sets of dots were deposited using identical fabrication parameters with the exception of the metal content of the ink. The ink with the lower metal nanoparticle content was less viscous and therefore enabled the fabrication of a set of dots with smaller diameters [Figure 34]. Evaporation-initiated thickening of the ink was avoided by quickly using the ink in the reservoir before significant evaporation could occur. During an experiment, all fabrication parameters (including the metal nanoparticle content of the ink) for two sets of dots were identical except for the time that was allowed to elapse before the initiation of the nanoassembly process. The set of dots that was deposited with less elapsed time exhibited smaller dot sizes [Figure 35].

The combination of lowered deposition forces and reduced-viscosity nanoparticle inks was employed in the fabrication of high resolution 60 to 80 nm FWHM (full-width, half-max) dots under contact mode conditions [Figure 36]. For example, a dot-matrix-like pattern of dots was arranged to spell out the letters "MIT". The entire word was 300 nm tall and less than 1 micron long [Figure 37]. Even smaller dots are possible when switching from contact mode to tapping mode operations, wherein the cantilever is caused to vibrate at a frequency of several hundreds of kilohertz. Because the tapping mode feedback loop is sensitive to changes in frequency of the resonating cantilever (a long range effect) instead of changes in the angle of deflection of a non-resonating cantilever (a short range effect) used by a contact mode feedback loop, a vibrating tip can provide advance warning of the approaching surface as the tip descends to deposit a dot. The increased long-range sensitivity allows the tapping mode z-piezo feedback loop to act more quickly to reduce the excessive over-shoot forces that may be generated when the tip first impacts the surface. To further decrease the likelihood of over-shoot force, a "tip preservation" procedure was implemented in many tapping mode experiments wherein the engagement of the tip with the surface was a two-step operation with the execution of a first lesser force setting followed by a second greater force setting. The very smallest dots ever deposited by the NanoAssembly system were created using a low-viscosity liquid-phase silver nanoparticle ink, a tapping mode cantilever, and a lithography software script that included "tip preservation" operations to minimize impact forces [Figure 38]. These dots were 32 nm across (FWHM) with a remarkable height of nearly 15 nm, thereby providing a height-to-width aspect ratio of nearly 0.47. It is very likely that the dots were in actuality somewhat smaller than 32 nm, as the contribution from the radius of curvature of the imaging tip to the observed measurement of dot diameter was not factored in. Depending on the particular manufacturer and the condition of the tip, the radius of curvature of the tip can be between 10 nm and 30 nm, or more.

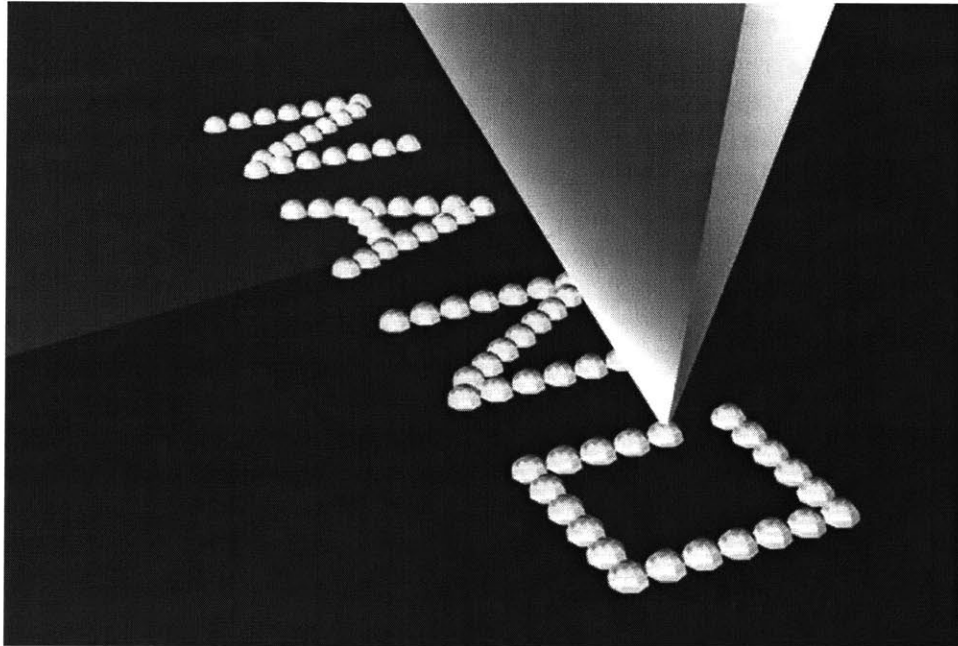


Figure 31 --- A rendered view of the extreme end of the AFM probe tip being used to deposit discrete dots of material to form the letters in the word "NANO".

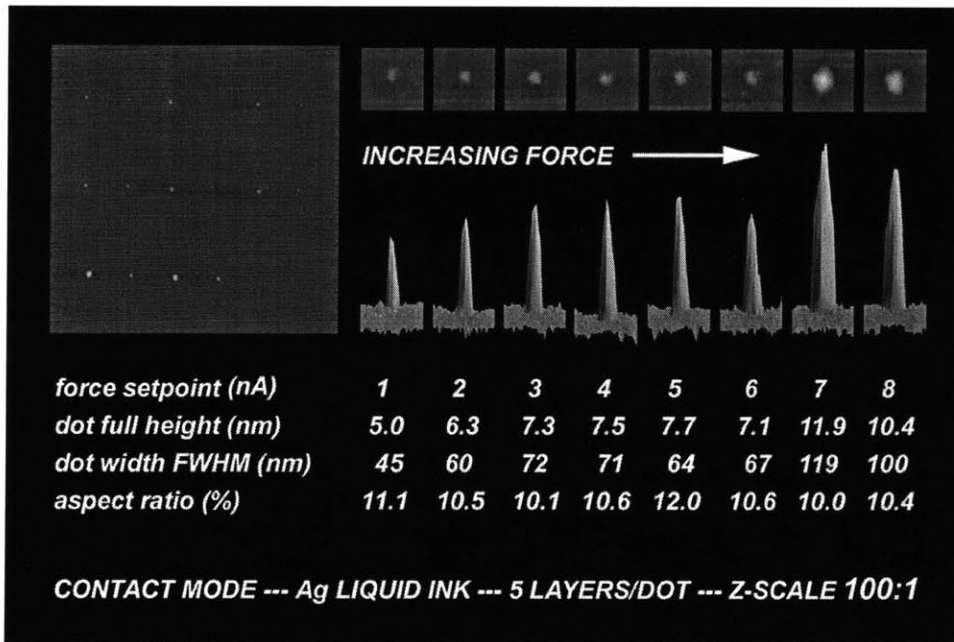


Figure 32 --- There is a direct correlation between tip contact force and the size of the deposited dot. Smaller dots are formed when using reduced forces. [Ex. q-231-ee]

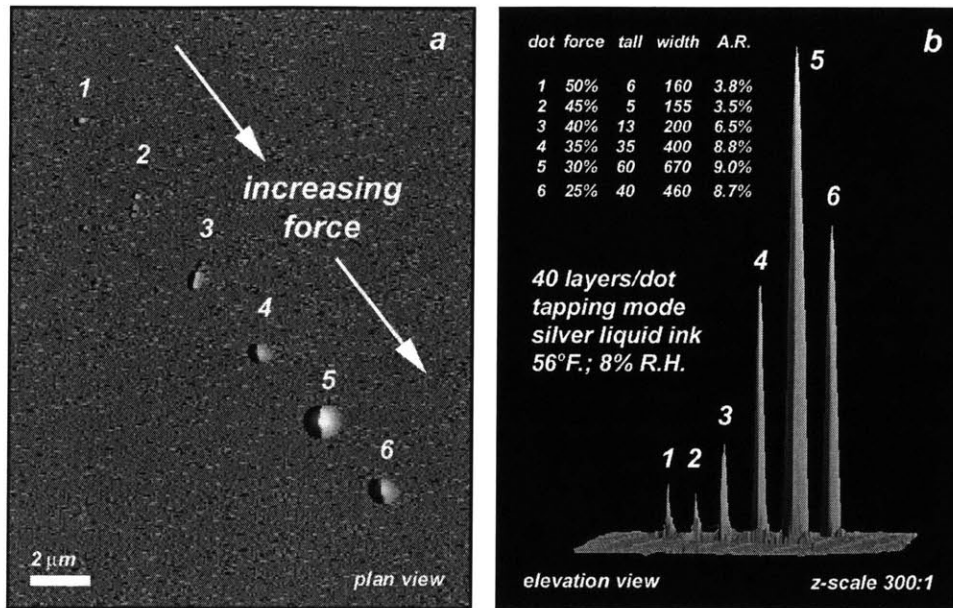


Figure 33 --- The correlation between tip contact force and the size of the deposited dot is particularly dramatic for multi-layer dots fabricated using tapping mode. [Ex. q-230-q]

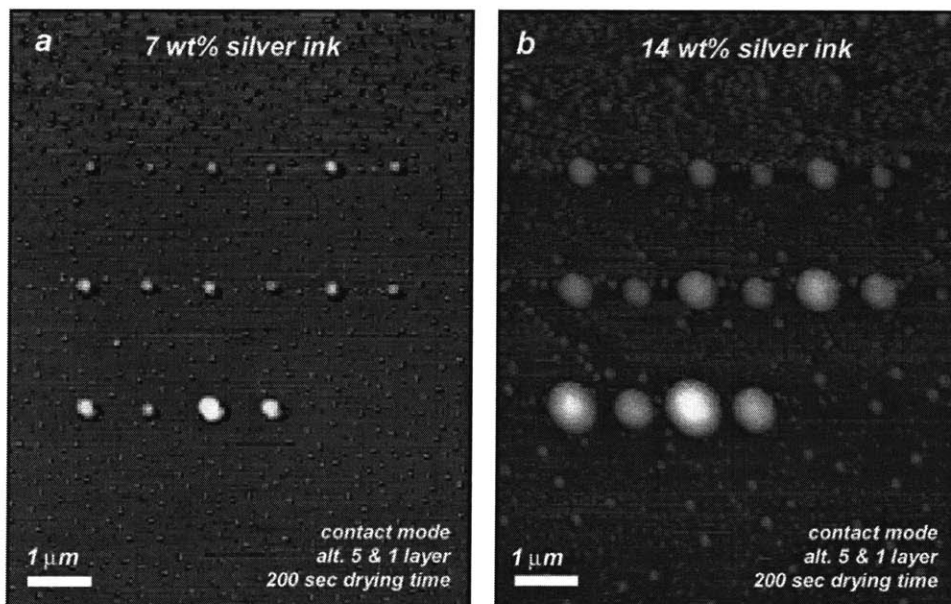


Figure 34 --- Two sets of dots were deposited using identical fabrication parameters except for the silver metal content of the ink. The dots formed from the ink with lower metal content were smaller. a [Ex. q-231-rr]; b [Ex. q-231-qq]

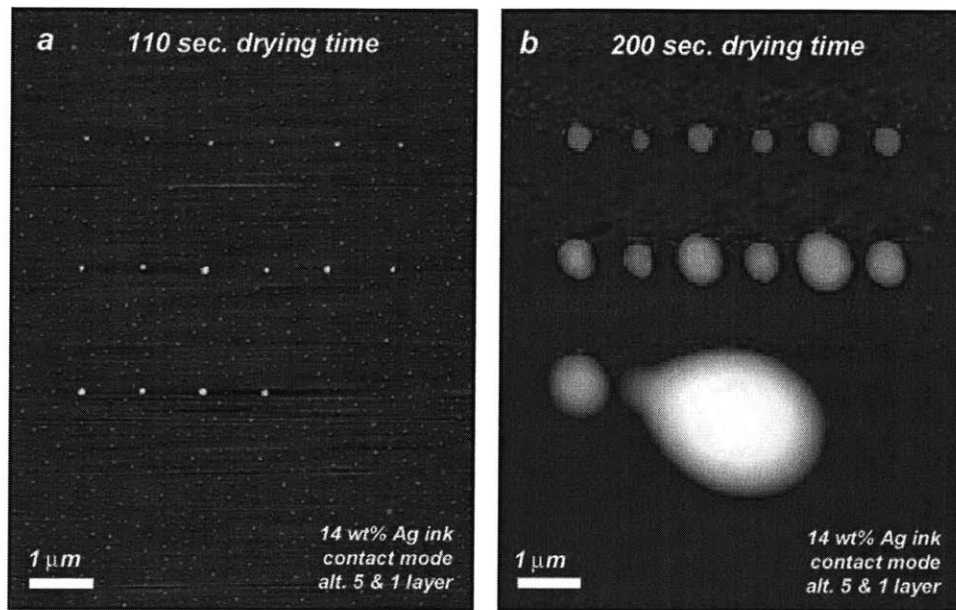


Figure 35 --- Two sets of dots were deposited using identical fabrication parameters except for the evaporation time allowed to elapse before deposition of the dots. The dots with less evaporation time were smaller. a [Ex. q-231-oo]; b [Ex. q-231-nn]

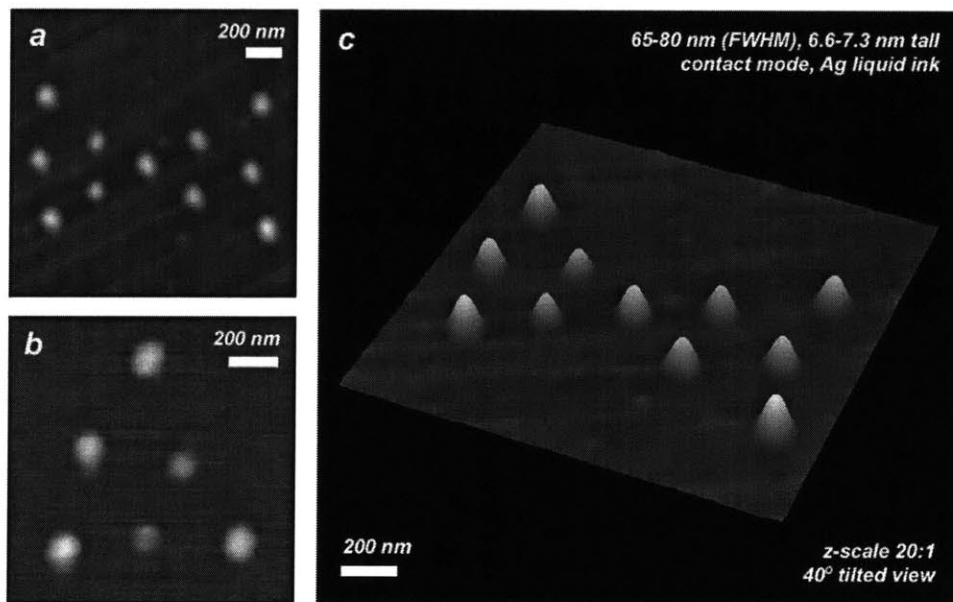


Figure 36 --- Reduced deposition forces and low-viscosity liquid silver inks were employed for the fabrication of high resolution 60 to 80 nm dots under contact mode conditions. [Ex. q-231-uu]

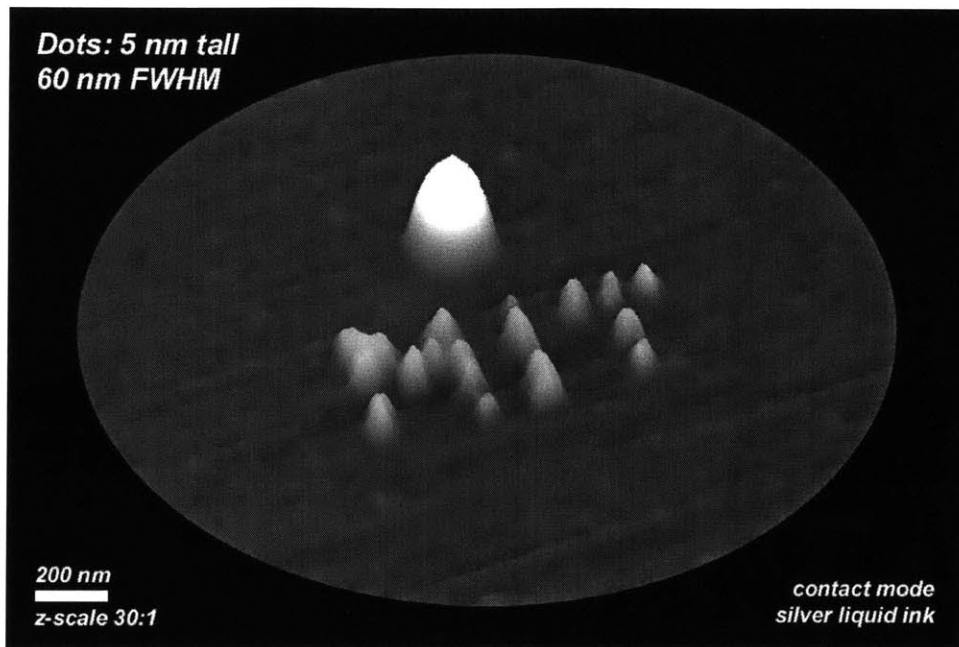


Figure 37 --- A pattern of 50 to 70 nm dots from silver nanoparticle liquid-phase ink was arranged to create the letters "MIT" using contact mode. The word was 300 nm tall and less than 1 micron long. The 5-layer dot in the background is 12 nm tall. [Ex. q-231-xx]

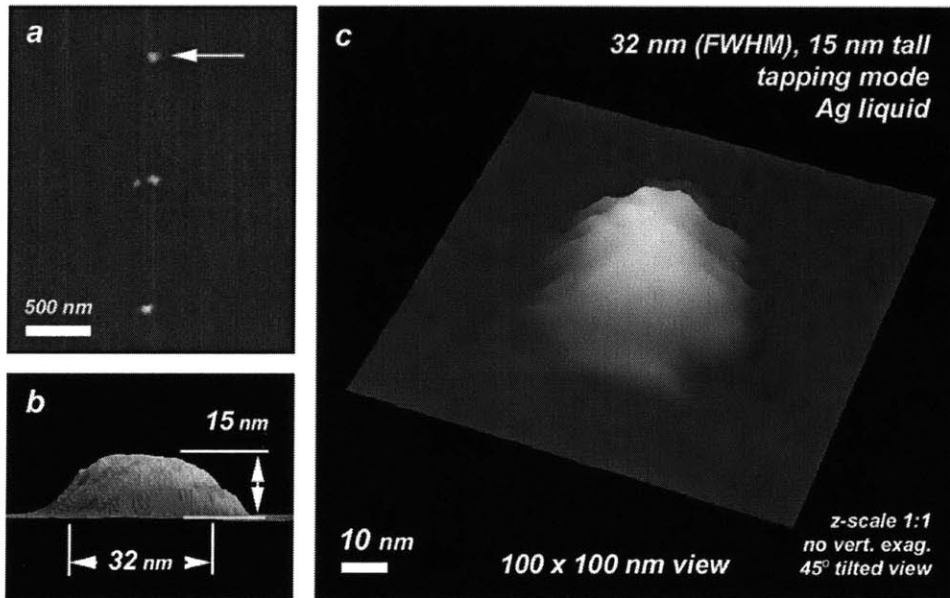


Figure 38 --- The smallest dots were deposited using a low-viscosity liquid-phase ink, a tapping mode cantilever, and a lithography software script that included "tip preservation" operations which minimized impact forces. These dots were 32 nm across (FWHM) with a height of nearly 15 nm and an aspect ratio of 0.47. [Ex. q-229-g]

Working with liquid phase inks

Fabrication at low temperatures and reduced humidity

Liquid phase inks present a unique set of challenges for the nanoassembly technique. Some liquid phase materials, such as nanoparticle inks, rapidly increase in viscosity with increased evaporation time, which has a detrimental effect on dot size. To enable long-term fabrication of complex high-resolution patterns, a double-stacked peltier substrate cooling system was installed to dramatically slow down the ink evaporation rate and to keep the ink viscosity nearly constant for the duration of the deposition process [Figure 39]. With a stabilized viscosity, the cooled ink in the reservoir could be used in the liquid state for many tens of minutes after being originally formed, thereby eliminating the need to hurriedly complete all dot depositions before the ink in the reservoir dried out. At the conclusion of the deposition procedures, the polarity of power supply driving the same peltier stack could be reversed to enable *in situ* thermal curing of the nanoassembled structures before AFM imaging.

Working at reduced temperatures also necessitated working at reduced or nominal humidity to prevent the condensation of moisture on the cooled substrate. For a number of the experiments, the AFM head assembly was placed inside an environmental chamber so that humidity and gas composition could be controlled and monitored during the lithography run [Figure 24]. Steady-state humidity level was maintained within the chamber by providing a fixed level of over-pressure of a gas with zero moisture content such as nitrogen, argon, or oxygen. Unlike the prior art demonstrated by Mirkin *et. al.*, the ability of the NanoAssembly system to deposit materials onto a substrate is not dependent on the level of moisture content in the atmosphere. Because the formation of a humidity-initiated liquid meniscus between the tip and the substrate is not required to carry out successful depositions, the Pick-and-Place NanoAssembly technique exhibits numerous advantages including improved deposition speeds, a vastly broadened materials set, and the ability to work with materials and within environments that are adversely affected by the presence of water.

In one example experiment, the peltier and humidity chamber enabled the fabrication of a series of multi-layer dots onto a silicon substrate at a reduced temperature of 11.6 degrees C. (52.8 degrees F.) and at a relative humidity of between 0 and 2 percent under an oxygen atmosphere [Figure 40]. The cooled ink pool, which would have dried hard in less than 10 minutes at room temperature, was kept in the liquid state for more than 30 minutes and allowed the completion of an 8-minute long lithography run with little change in ink viscosity. The peltier was then used to thermally cure and convert the ink dots into solid-phase structures at 100 degrees C.

Evaporation-insensitive inks

Although many of the experimental procedures described so far have primarily focused on the deposition of dots made from gold and silver nanoparticle inks, a number of other ink materials have also been used to fabricate dots. These additional materials include a mixture of photoresist and alpha-terpineol, a mixture of spin-on-glass and alpha-terpineol, a silicone (PDMS), and an ultra-violet (UV) light curable optical adhesive. In particular, the last two inks in this group offer a distinct advantage over evaporation-sensitive inks. PDMS and UV adhesives have exceedingly low vapor pressures and do not readily evaporate at room temperature. The viscosity of the fluids can be kept constant for very long periods of time without the requirement for reduced fabrication temperatures. With constant viscosity ensured, very long and complex patterns can be deposited at leisurely rates over the course of hours or days, if required.

Tapping mode compensation for ink pool flooding

Micron-scale pools of liquids exhibit many of the surface tension, spontaneous pooling, and other fluid-related effects of their macro-scale counterparts. In one experiment, several multi-layer liquid-phase dots were deposited by the NanoAssembly system onto a flat substrate in close proximity to each other. The liquid in the micron-sized dots spontaneously flowed a short distance across the surface to join together to form one larger dot [Figure 41]. This very mobile behavior of liquids becomes a problem when a tip engages an ink reservoir using the contact mode. Very often a "flooding" effect is observed, wherein a large quantity of ink from the reservoir is spontaneously sucked up onto the stationary tip. The ink can rapidly traverse the entire length of the cantilever, thereby spoiling the nearby deposition zone. A tapping mode vibrating tip can prevent this 'flooding' effect from occurring while the tip is retrieving liquid-phase ink from the reservoir. The heightened force sensitivity of the tapping mode feedback circuit allows the tip to acquire just enough ink, without becoming sucked down into the liquid reservoir. As ink begins to rush up onto the tip, the feedback circuit detects the dramatic reduction in resonant frequency and amplitude. To compensate, the z-piezo is immediately activated to pull the tip farther up out of the reservoir. When the cantilever resonant frequency is becomes nearly restored, the z-piezo drives the tip back down into the reservoir. By adjusting the integral setting of the feedback loop to accommodate a number of factors including the viscosity of the ink and the force setpoint, the tip can resonantly engage the liquid surface of the ink reservoir without flooding. A standing ripple wave can be established within the ink pool at a frequency of 3 to 20 Hertz.

Frequency tuning algorithm for added mass compensation

Much of the challenge of using liquid phase inks stems from the fact that a substantial mass of ink can be suddenly added to the end of the cantilever when the tip is dipped into the reservoir. This causes the resonance frequency to drop dramatically, and causes the amplitude to increase. Then, in the fraction of a second required to translate the tip to the deposition zone, a significant portion of the liquid mass may be lost due to solvent evaporation. Because the force applied by a tapping mode tip to the substrate is regulated by resonance frequency feedback control, a frequency tuning algorithm that dynamically compensates for rapid frequency changes was developed. To ensure that the proper level of force is applied by the vibrating tip to the substrate while depositing a dot, the tuning algorithm performs the following set of operations: (1) rough-tune and fine-tune frequency sweeps to find the newly acquired resonant frequency of the ink-laden cantilever; (2) the z-piezo electronic drive frequency is set to coincide with the cantilever mechanical frequency to obtain the maximum resonant response; and (3) the setpoint scale, which is used to define the desired force that should be applied between the tip and the substrate, is re-calibrated so that the maximum signal derived from the resonant peak of the freely vibrating cantilever is set to be full scale. This tuning operation is often implemented just after withdrawing ink material from the reservoir and again just before deposition. Optionally, the tuning operation can be initiated yet again immediately after the deposition of a dot of ink. The resonant frequency of the cantilever before and after the deposition of the dot can be compared to reveal the precise mass of ink that was deposited onto the substrate. A cantilever with a natural (un-loaded) resonant frequency of approximately 300 kilohertz and frequency shift sensitivity of about 170 hertz was used to detect mass changes as small as 12 picograms ($\sim 10^{-11}$ kg) in real time during nanoassembly experiments. Improvements to the frequency shift sensitivity, which are proposed in the section entitled "Resonating cantilever as real-time mass transfer detector", may enable the detection of mass changes as small as 0.12 picograms ($\sim 10^{-13}$ kg).

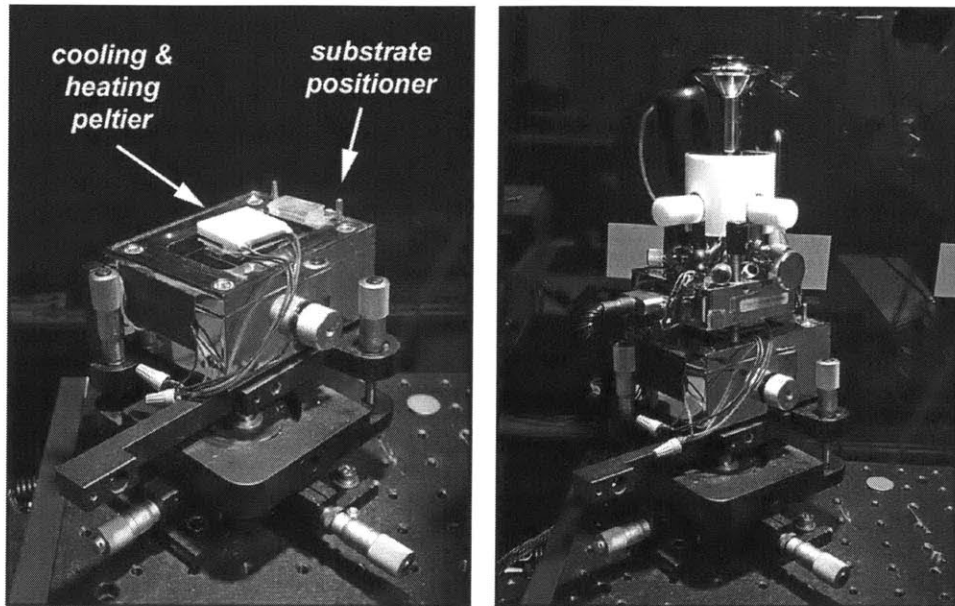


Figure 39 --- A double-stacked peltier cools the ink reservoir and stabilizes the viscosity of the ink for long-term lithography runs. At the conclusion of a lithography run, the polarity of the peltier's power supply can be reversed to enable thermal curing of the ink.

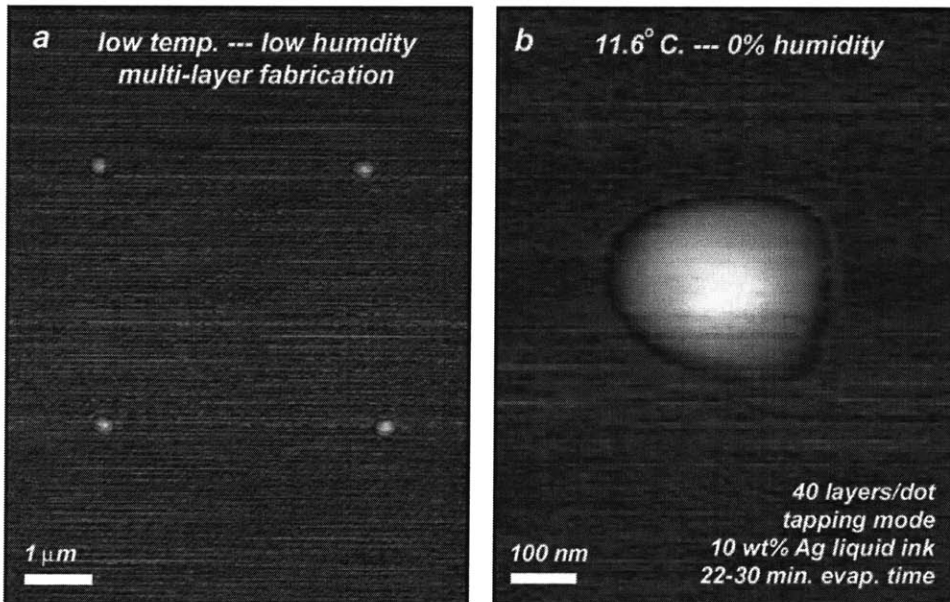


Figure 40 --- The nanoassembly process does not require humidity for successful deposition of nano-structures. During an extended 8-minute long build at low temperature, the maximum humidity during the run was less than 2% R.H. [Ex. q-230-I]

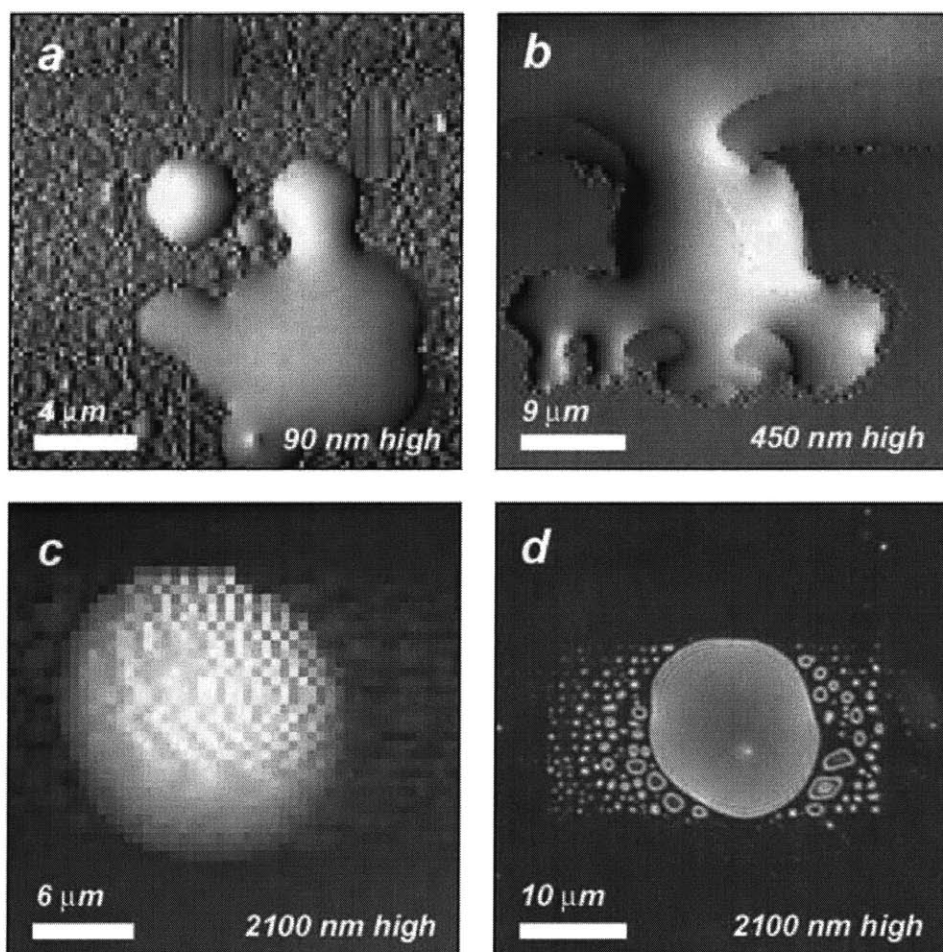


Figure 41 --- Micron-scale pools of ink deposited onto a substrate by the nanoassembly process exhibit many of the surface tension, spontaneous pooling, and other fluid-related effects of their macro-scale counterparts. These images clearly show that the ink was still in the liquid phase at the point when the tip deposited the ink onto the substrate. ---
 - Figure 'a' is a square arrangement of four multi-layer dots of gold nanoparticle ink (1 wt% gold). The dot in the lower right corner consisted of 100 layers, while the remaining three dots were fabricated from 10 layers each. Three of the dots spontaneously joined each other by way of a fluid phase isthmus. [Ex. q-238-d] ---- Figure 'b' shows a liquid phase deposition of UV-curable optical adhesive (Norland #72). [Ex. q-236-b] ----
 Figure 'c' and Figure 'd' are AFM and optical images of a very tall liquid phase deposition of UV-curable optical adhesive. The dot was constructed from 100 separate depositions, and is 2100 nm high. The scanning action of the AFM tip while imaging created the parallel lines of liquid droplets on both sides of the central ink dot. [Ex. q-236-g]

Fabrication of dots with solid-phase inks

As the solvent fraction of a nanoparticle ink evaporates, the overall viscosity of the ink in the reservoir increases, which leads to the deposition of larger dots. With additional evaporation time, the dot size rapidly reaches a maximum value as the ink viscosity continues to increase. As the ink begins to solidify into a soft solid, the dot size then begins to decrease. With even more evaporation time, the ink in the reservoir becomes a harder solid, and even smaller dots are achievable [Figure 42]. In some cases, dots can be fabricated from solid-phase ink reservoirs that have been allowed to dry for more than 3 hours at room temperature [b]. Eventually the ink in the reservoir becomes so hard that no material can be withdrawn by the tip, and dots can no longer be deposited. In general, solid phase inks are simpler to use than liquid phase inks. There are no complications associated with short evaporation times, rapidly changing viscosity, and flooding. For example, tapping mode dynamic frequency tuning algorithms are usually not required, because the mass of solid ink acquired by the tip is generally too small to significantly alter the resonant frequency of the cantilever.

Contact mode is the preferred mode for the extraction of small volumes of solid phase inks from a reservoir. After the tip retracts from the reservoir after a dipping action, deep tip-shaped indentations are left behind on the reservoir's surface [Figure 43]. Although the tapping mode can generally be used for the extraction of liquid phase and even "slushy phase" inks, this mode is generally not suitable for withdrawing material from a solid-phase ink reservoir due to the reduced forces imparted by the vibrating tip against the solid surface of the ink. Once a quantity of solid ink is adhered to the tip, either contact or tapping modes can be used for the actual deposition of the ink onto a substrate. For the sake of simplicity, contact mode dipping and contact mode writing are most commonly employed when using solid-phase inks. On occasion, special lithography scripts have been executed wherein the Z-axis piezo was compelled to rapidly switch between contact mode for dipping and tapping mode for writing for each and every dot that was deposited. This switching procedure provided sufficiently high contact mode impact forces for ink extraction from the solid reservoir and sufficiently light tapping mode impact forces for deposition of dots with minimum size onto the substrate [Figure 44] [Figure 45]. This alternating procedure enabled the discrete assembly of a tightly packed line of sub-100 nm dots of solid ink onto a silicon substrate [Figure 46]. However, it should be noted that this procedure places high stresses on the high voltage piezo drive electronics, and can cause one particular microchip inside the amplifier unit of the Explorer system to fatigue and fail.

Grayscale dots using the "scratch pad" method

When using soft solid inks, dot size can be reduced by modifying a number of key parameters including tip force, tapping or contact mode, and hardness of the ink material. Dot size can also be substantially reduced by using a "scratch pad" method wherein the tip is dipped only once into the ink pool and is then used to deposit more than one dot onto the substrate. As expected, the first dot in the series is the largest, because the tip is fully laden with ink from the reservoir. The second dot is substantially smaller, with subsequent dots in the series being smaller still [Figure 47] as more of the excess ink is removed from the tip. A number of these preliminary dots can be deposited within a "scratch pad" zone on the substrate, while the last dot in the series is deposited in the intended construction zone. This final dot is much smaller than can normally be obtained using the standard "one-dip, one-dot" approach. When using solid phase inks and contact mode operations, the process is very repeatable, and the dot size from one deposition cycle to the next is surprisingly uniform. It is suspected that the "scratch pad" method would also be an effective means of dot size reduction for liquid-phase inks and tapping mode operations. Large numbers of grayscale dots can be combined to form lines, letters, and other two-dimensional structures with resolutions below 100 nm [Figure 48].

In one experiment, four lines of dots were deposited in parallel using the "scratch pad" method, one dot at a time [Figure 49]. The fourth in the series of lines, formed from dots generated by one dip of the tip into the ink reservoir followed by four deposition steps, was comprised of dots that were approximately 300 nm across (FWHM) and 26 nm tall. These dots were less than half of the width and half of the height of the first-in-series dots. After the lines were cured with a hotplate at temperatures up to 450 degrees Celsius, SEM imaging revealed that the ink within the dots coalesced together to form conglomerated particles. The size of the particles decreased with decreasing thickness of the deposited line [Figure 50]. The particle size in the fourth-in-series dots was as small as 10 to 80 nm, with an inter-particle spacing of 10 to 20 nm. AFM imaging showed that the largest particles had a maximum height of 10 to 16 nm.

If the 'scratch pad' technique had been pushed even further, it is likely that ninth-in-series or tenth-in-series dots would have been very small, perhaps as small as a single nanoparticle with a diameter of a few nanometers. The 'scratch pad' method may prove useful for the discrete fabrication of a single electron transistor (SET), wherein a single metal nanoparticle is deposited by the tip precisely at the junction between the source, drain, and gate electrodes to form the Coulomb blockade island of the SET.

Nano-stamping with solid-phase dots

Unlike liquid-phase inks, solid-phase inks can be patterned onto a surface such that imperfections in the geometry of the end of the tip are replicated in the geometry of the deposited dot. In essence, a tip can be used as a nano-scale stamp, wherein the relief pattern on the end of the tip can be transferred to the substrate via the ink that is adhered to the tip. A typical silicon tip is very sharp and has a uniform pyramidal shape. A sharp tip has only one point of contact with the substrate, and is therefore capable of depositing only a single dot during each deposition step. A well-worn tip may become flattened, and often develops two or more lobes that protrude from the end of the tip. During several nanoassembly experiments, the arrangement of these lobes was replicated in the ink that was deposited onto the substrate. The lobe pattern was replicated into single-layer and multi-layer depositions. Every mound of deposited ink had an outline which mimicked the shape of the damaged tip. In one case, complicated letter patterns were created using a multiple-lobed tip to produce a calligraphy-like effect wherein the horizontal lines of a letter were wider than the vertical lines [Figure 51].

It is envisioned that a single electron transistor (SET) with a complete complement of electrodes (source, drain, coulomb blockade island, and gate) could be patterned with metal nanoparticle inks using just a single deposition step. In this case, the tip would be cut into four closely spaced lobes using a high-resolution milling tool such as a focused ion beam (FIB). Each lobe would transfer its load of ink directly to the surface to form four distinct nanometer-sized dots, with the spacing between the dots being precisely and rigidly defined by the pattern of lobes on the end of the tip.

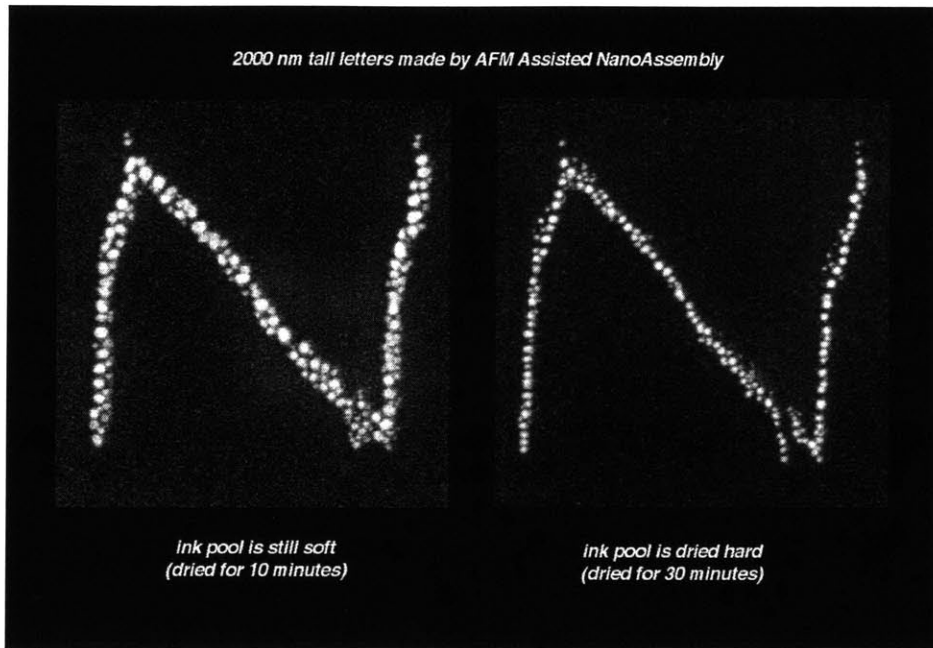


Figure 42 --- Two 'N's assembled with identical parameters from the same ink reservoir, but with different drying times. Dot size decreased as the ink changed from a soft solid to a harder solid. Left [Ex. q-225-s] ; Right [Ex. q-225-t]

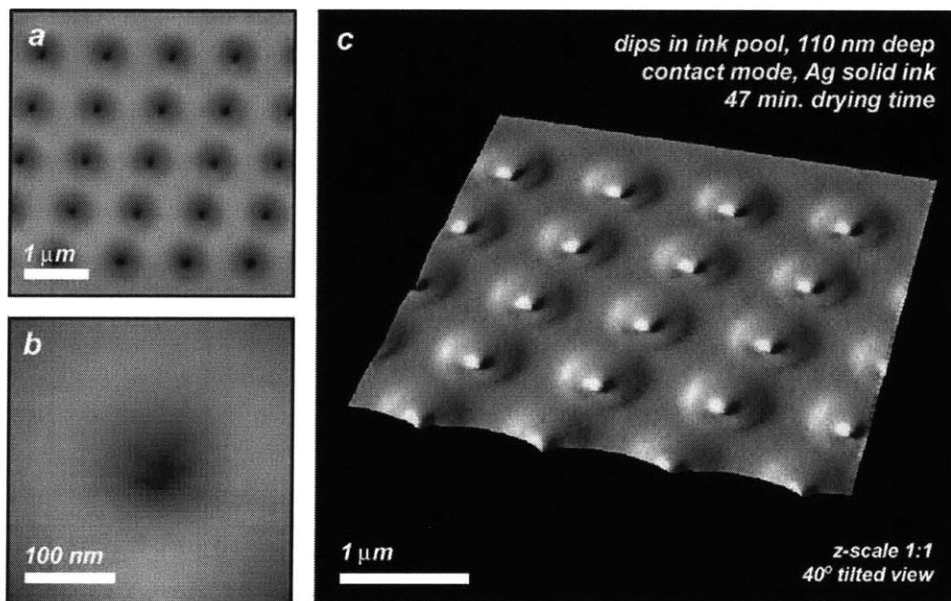


Figure 43 --- Deep indentations are left in the surface of a solid-phase ink reservoir after the tip extracts material from the reservoir in contact mode. [Ex. q-232-i]

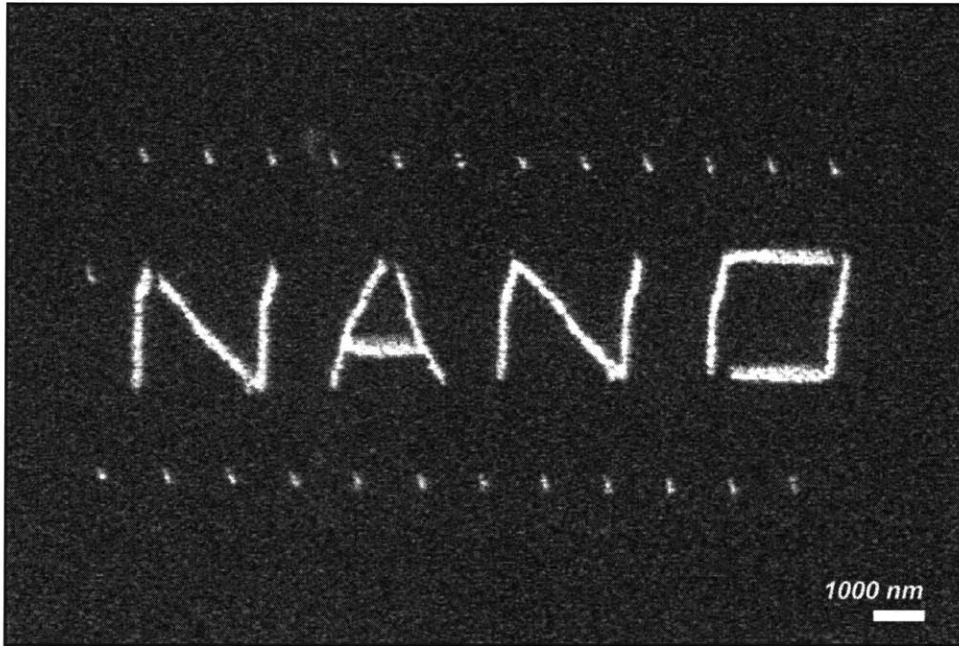


Figure 44 --- The word "NANO" was assembled using discrete dots of a soft solid ink. The ink drying time was short, resulting in relatively large dot size. [Ex. q-225-s]

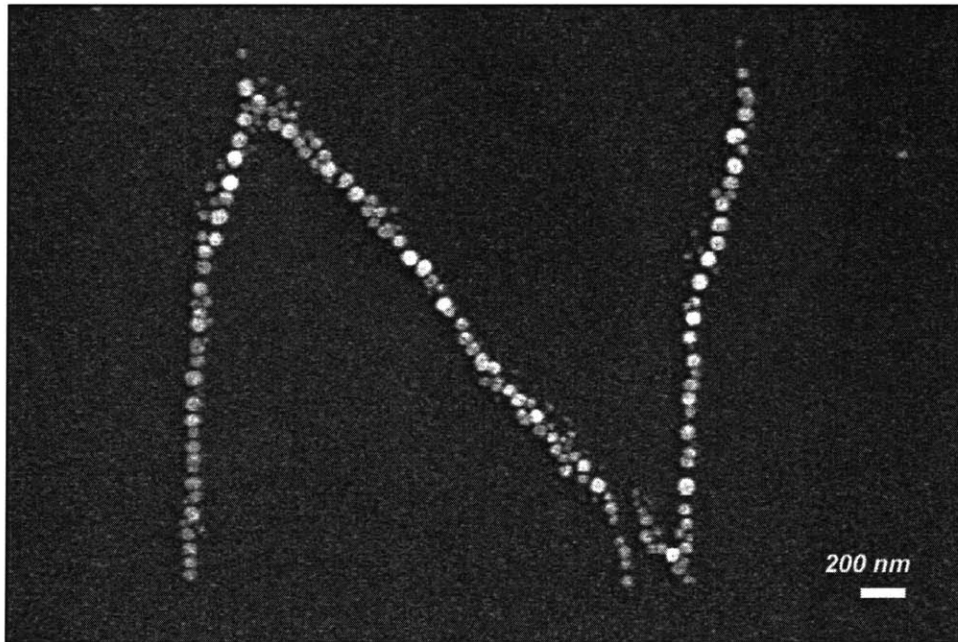


Figure 45 --- The letter 'N' was assembled from solid ink using a switching procedure: contact mode for dips into the reservoir, and tapping mode for deposition. [Ex. q-225-t]

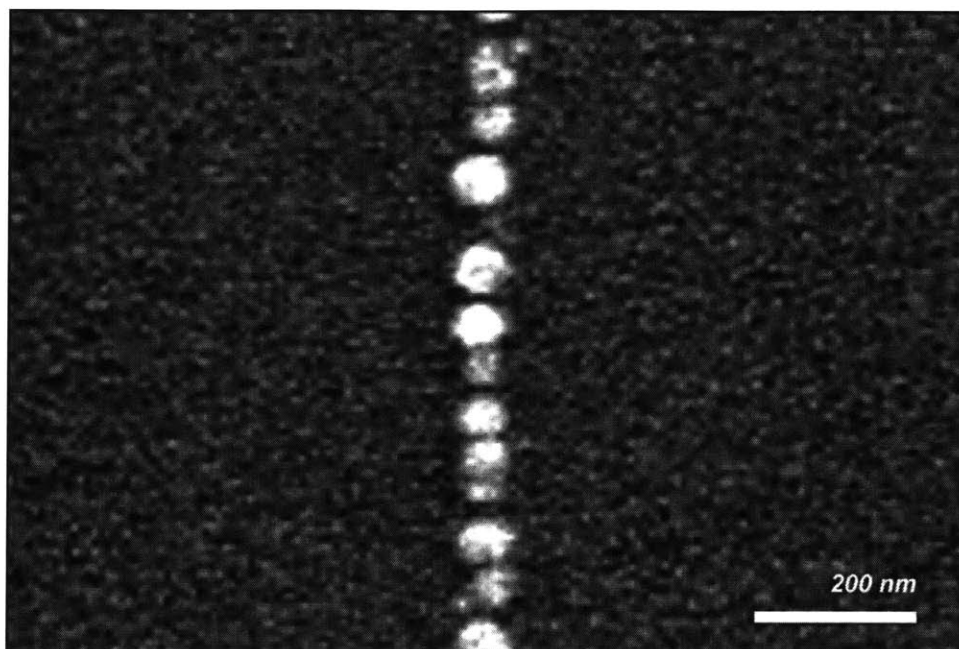


Figure 46 --- SEM images of a tightly-packed line of sub-100 nm dots of silver nanoparticles assembled using contact mode for dipping into a solid ink reservoir, and tapping mode for deposition of the dots onto a silicon wafer substrate. [Ex. q-225-t]

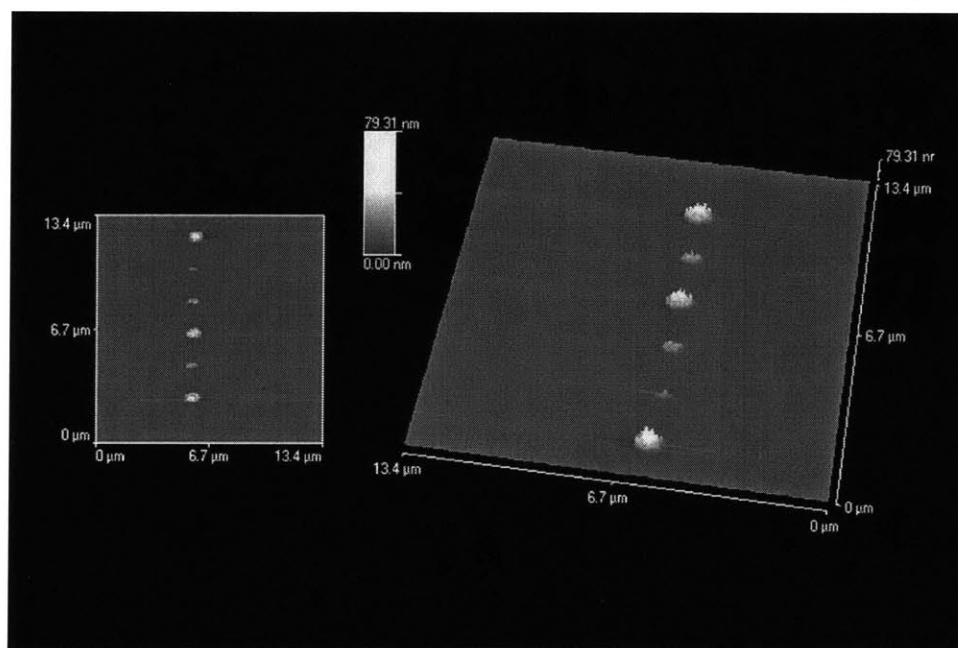


Figure 47 --- Grayscale dots deposited using a solid-phase silver ink in contact mode. Three separate dips into the reservoir were used to make six dots. From top to bottom, the deposition "series number" of each dot was 1, 2, 1, 2, 3, 1. [Ex. q-224-h]

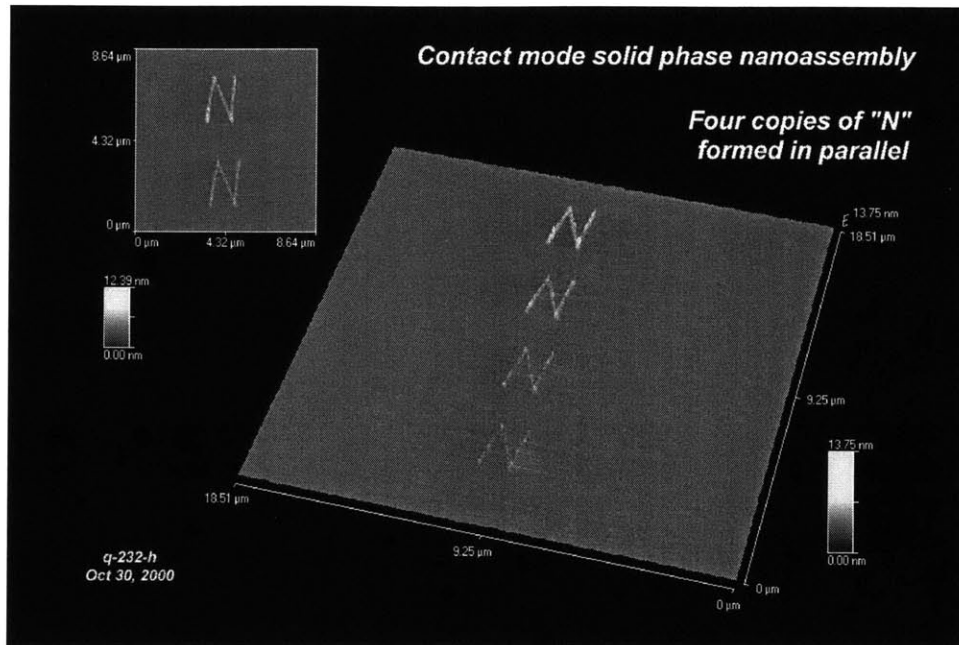


Figure 48 --- Four copies the letter "N" formed in parallel from solid-phase silver nanoparticle ink dots spaced at 100 nm centers using the contact mode "scratch pad" assembly method. The line width of the 4th copy is below 100 nm. [Ex. q-232-h]

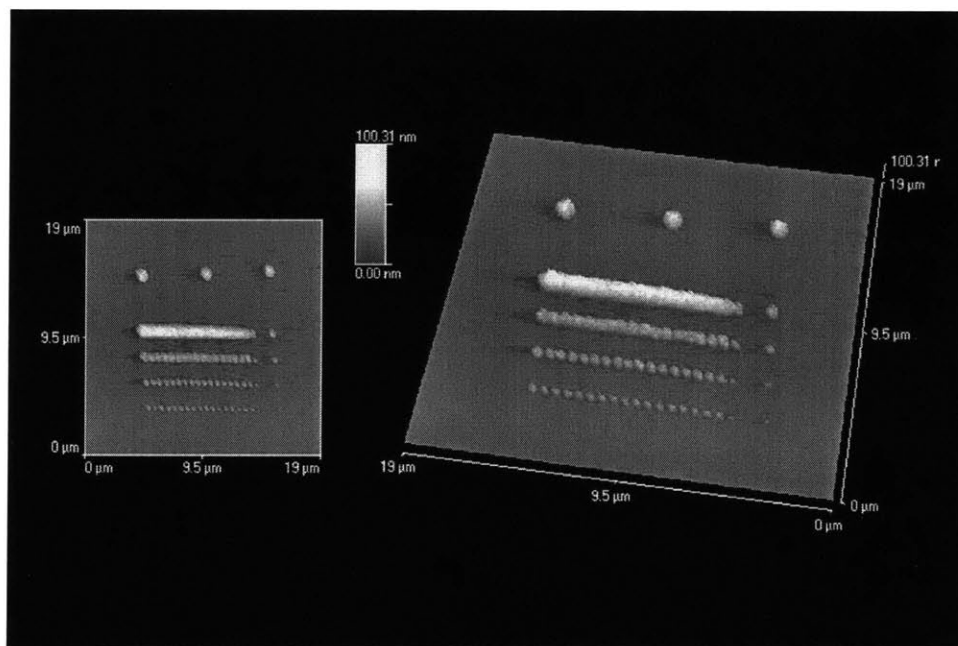


Figure 49 --- Grayscale lines formed in parallel by dipping the tip into a solid silver nanoparticle ink pool and then making a series of four contact mode depositions onto a silicon substrate. The dot size was very uniform. Uncured ink. [Ex. q-224-i]

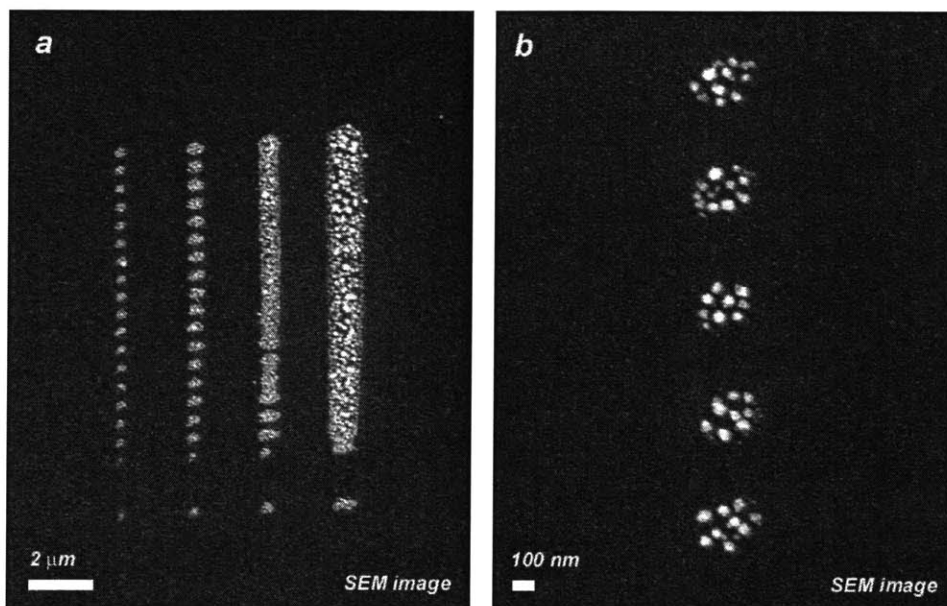


Figure 50 --- SEM images of four grayscale lines formed in parallel using the method described in Figure 49. Figure 'b' is a close-up view of the left-most "fourth deposition" line of dots shown in figure 'a'. The dots were cured at 250 C for 8 minutes and 450 C for 10 minutes. Final particle size in the "4th deposition" was 10 nm to 80 nm. [Ex. q-224-i]

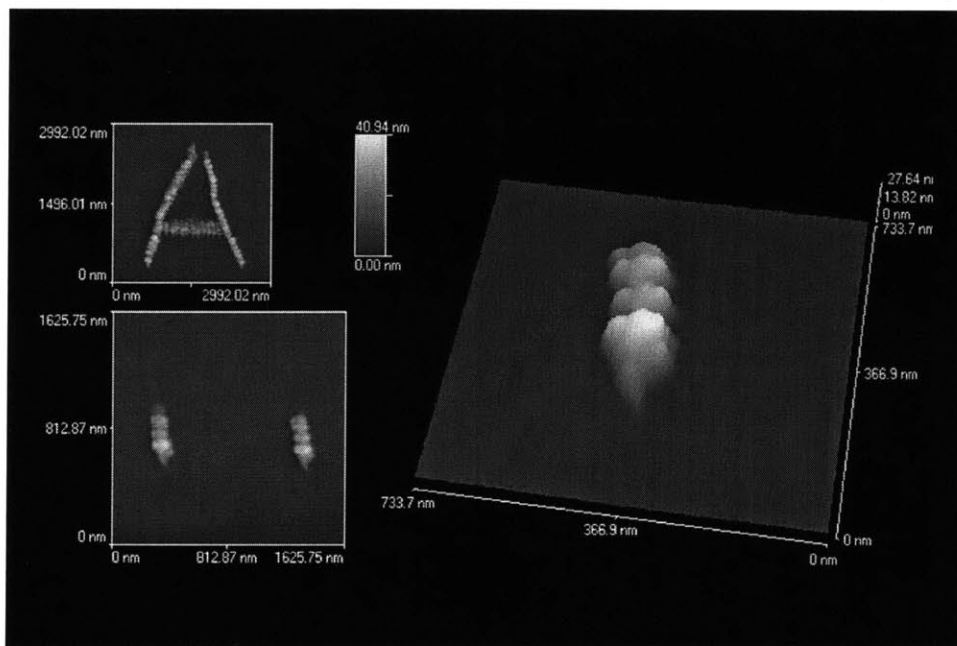


Figure 51 --- The geometry of a damaged tip is replicated in the shape of ink dots deposited onto a substrate. Specially shaped tips may be used as nano-scale stamps, for the direct 1-step deposition of complicated structures such as SET devices. [Ex. q-225-t]

Fabrication of lines

Lines can be fabricated by dragging an ink-laden tip across the surface of a substrate. Lines have been constructed at high translation speeds of 1 to 100 microns per second using both contact and tapping mode operations, with liquid-phase and solid-phase ink sources. A typical line fabrication procedure involves the following major steps: (1) dipping the tip into a reservoir of ink; (2) withdrawing the tip from the reservoir; (3) high speed translation of the tip to the deposition zone at a height of several microns above the surface of the substrate; (4) engagement of the tip with the substrate; (5) dragging the tip across the surface at moderate speed to cause the deposition of a line of ink material; (6) lift-off of the tip from the surface; and (7) high speed levitated translation of the tip back to the ink reservoir. This complete cycle of steps is repeated once for every line that is deposited. The actions required for the fabrication of lines are essentially identical to those needed for dot formation, with the exception of step (5). The most basic kind of line is can be deposited using a contact mode (non-vibrating) tip and a liquid-phase ink. When the ink-laden tip first engages the substrate at the very beginning of the line, a large bulbous mass of liquid is often deposited [Figure 52]. The line generally has a tapered appearance wherein the line width decreases over the length of the line. Eventually the ink on the end of the tip runs out or dries out, and the line simply ends. The bulbous mass is formed when surface tension initiated 'flooding' occurs as the liquid ink rushes off the end of the tip onto the surface. A reverse 'flooding' effect is also a substantial problem when the tip engages the ink reservoir, wherein a large quantity of ink from is sucked up onto the stationary contact mode tip. As discussed in previous sections, tapping mode operations combined with dynamic frequency tuning algorithms can be used to reduce both kinds of flooding effects. A tapping mode vibrating tip enables the fabrication of lines that do not exhibit large bulb-shaped masses of ink at one end [Figure 53]. The frequency of cantilever vibration, which is generally on the order of several hundreds of kilohertz, is high enough so that the surface-tension effects that would normally cause flooding and bulb formation are negligible. Although a tapping mode liquid-phase line does not generally exhibit a large bulb at its beginning, many small blots of ink are periodically deposited at regular intervals along the length of the line [Figure 54]. Depending on the viscosity of the ink, the drawing speed, and the force applied by the tip to the substrate, one blot of ink may be deposited every 1 to 2 microns along the line. The diameter of a blot is usually 2 to 6 times larger than the average thickness of the line. The line segments between the blots can have high resolution line widths that range between 30 and 40 nm [Figure 55]. Very thin thermally-cured lines of gold and silver nanoparticle inks have been fabricated which consist of a single-particle-wide string of 10 to 40 nm particles, with interparticle distances as small as 10 nm. These particles had heights that ranged between 6 and 15 nm [Figure 56 - a]. Height-width (FWHM) aspect ratios were as good as 0.50. Complicated shapes such as letters utilizing curved and sharply-angled lines were fabricated with only a very slight loss in line continuity at tip translation

speeds as high as 1 micron per second [Figure 56 - b]. On occasion, two closely spaced lines of ink can be simultaneously patterned by a single vibrating tip [Figure 57]. The tip continuously deposits an excess of liquid ink just ahead of its point of contact with the surface, and at the same time plows a trench into the deposited ink to cause the formation of two lines that are separated by less than 50 nm. One line is formed on each side of the translating tip. Fully continuous lines as thin as 45 nm have been fabricated by this method. This double-line effect requires the combination of a substantial excess of liquid ink adhered to the tip and higher than normal tip-substrate forces. Tip-substrate forces have also been used to control the width of deposited lines. As expected, increasing the force applied by the tip to the substrate increases the line thickness [Figure 58].

Tapping mode fabrication of continuous lines with liquid inks is challenging and has often proven to be somewhat unreliable, when compared to liquid-phase dot formation. However, many of the challenges associated with liquid-phase inks generally do not apply to solid-phase inks. When the consistency of a solid ink reservoir is still rather soft, before substantial drying can take place, a tapping mode tip can be used to fabricate lines. Unlike their liquid-phase counterparts, solid-phase lines are generally very uniform and do not exhibit bulb-shaped ends or periodic ink blots [Figure 62 - a]. As before, line width can be increased by increasing the average tip-substrate force [Figure 59]. The primary disadvantage of using solid-phase inks is the fact that a vibrating tip is only suitable for picking up the very softest of solids from the ink reservoir, due to reduced impact forces. Most materials harden rather quickly as they dry, and soon become unretrievable by a vibrating tip. If the solid ink can be softened or partially dissolved by a solvent, then a "solvent-assisted" fabrication method can be applied wherein a tapping mode tip is used for solvent acquisition, solid ink acquisition, and ink deposition. The tip is first dipped into a reservoir of a solvent of the solid ink, and then the drawing of lines is carried out in the normal fashion using the hardened solid ink reservoir. Very long, uniform, and thin lines can be drawn continuously until the solvent-ink mixture on the end of the tip runs out or dries out [Figure 60] [Figure 61]. Lines that are 60 nm wide and 20 microns long have been fabricated. These lines do not exhibit undesirable bulb-like formations at their ends or periodic blots of ink along their lengths. Just before the ink completely runs out, lines of very small sub-20 nm dots, each containing a single nanoparticle, can be deposited [Figure 62 - b]. A two-reservoir "solvent-assisted" method is envisioned in which the tip is dipped into a first pool of solvent and then into a second pool of solid ink before the fabrication of each line. This procedure may enable the construction of arbitrarily complex planar designs wherein the duration of fabrication is only limited by the evaporation time of the solvent in the solvent reservoir. Because most solvents do not change viscosity while they evaporate, the tapping mode integral feedback setting used to establish a standing ripple wave in the solvent reservoir and the setting used to dynamically adjust the cantilever frequency to compensate for additional solvent mass would not need to be altered over the entire duration of the run.

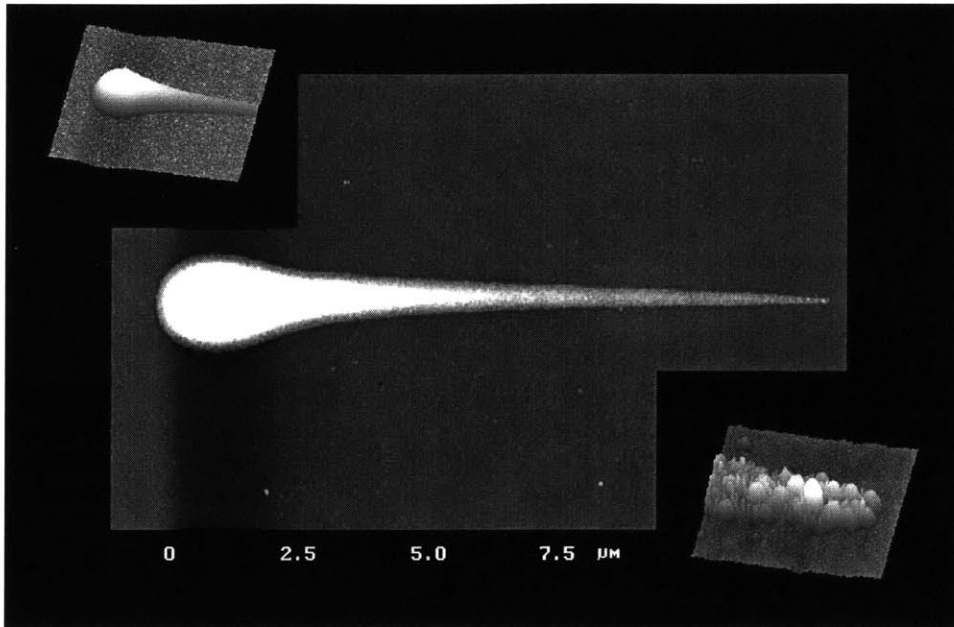


Figure 52 --- Contact mode deposition of a line of liquid-phase silver (30 wt%) nanoparticle ink at 2 microns/second onto a glass substrate. A large bulb of material was deposited at the beginning of the line. Thermally cured before AFM imaging. [Ex. q-061]

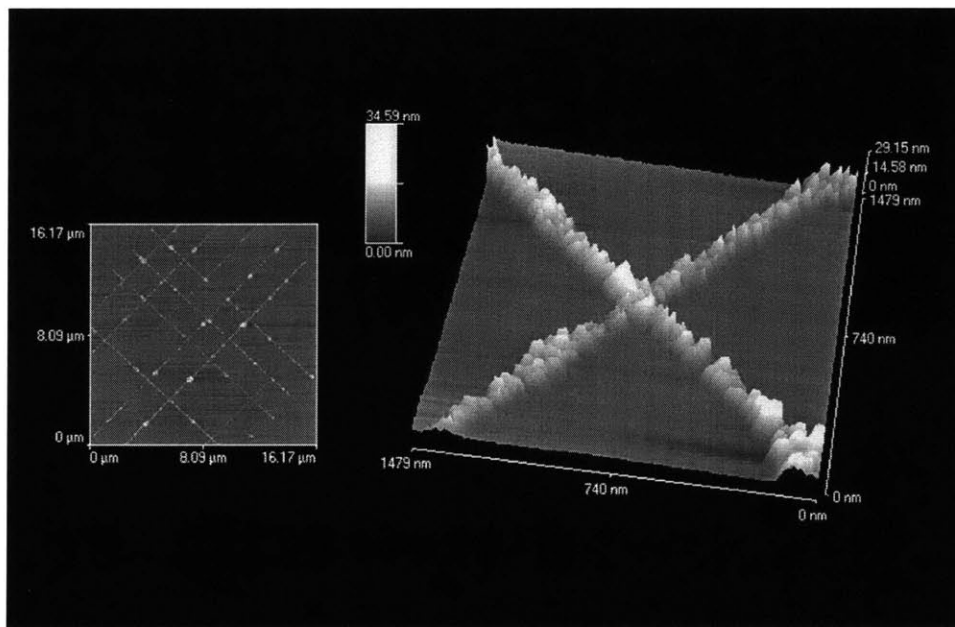


Figure 53 --- Tapping mode lines of liquid-phase silver (30 wt%) nanoparticle ink at 10 microns/second on a silicon substrate. Small blots of ink were periodically formed along the length of each line. A dynamic tip frequency tuning procedure was executed just before the formation of each line. Cured at 250 C. before AFM imaging. [Ex. q-224-d]

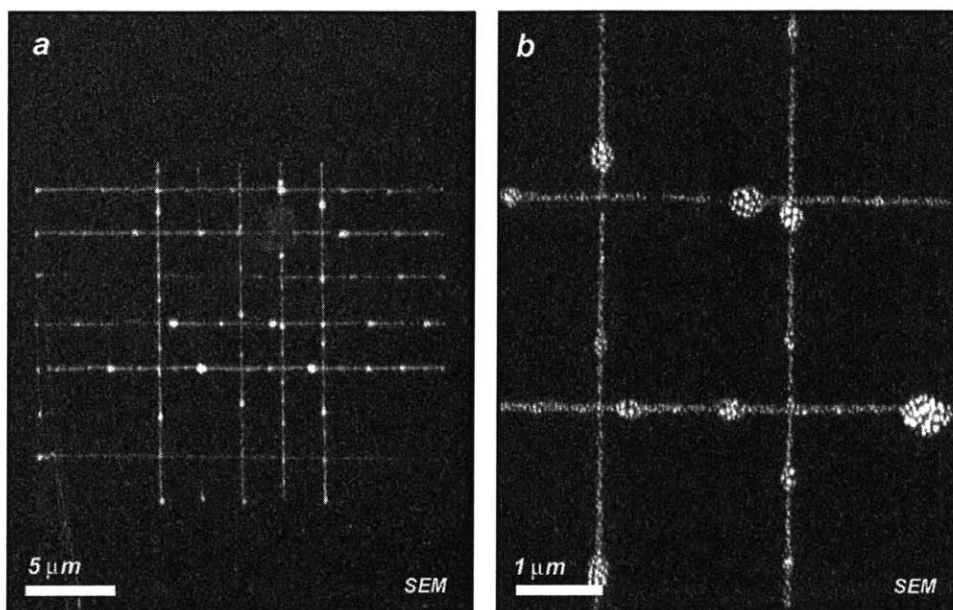


Figure 54 --- SEM images of the same grid of tapping mode liquid-phase lines presented in Figure 53 after thermal curing at 250 C. and then again at 450 C. The periodic deposition of blots of ink are clearly visible in figure 'b'. [Ex. q-224-d]

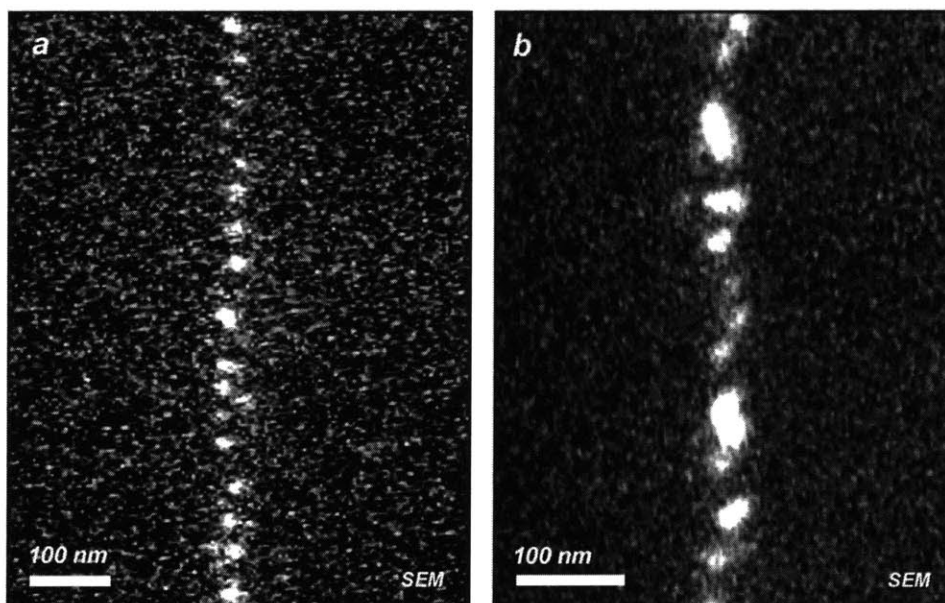


Figure 55 --- Close-up views of two different line segments within the tapping mode liquid-phase grid shown in Figure 54. The average line width of the string of nanoparticle dots shown in figure 'b' was 40 nm, with some sections being as thin as 17 nm. [Ex. q-224-d]

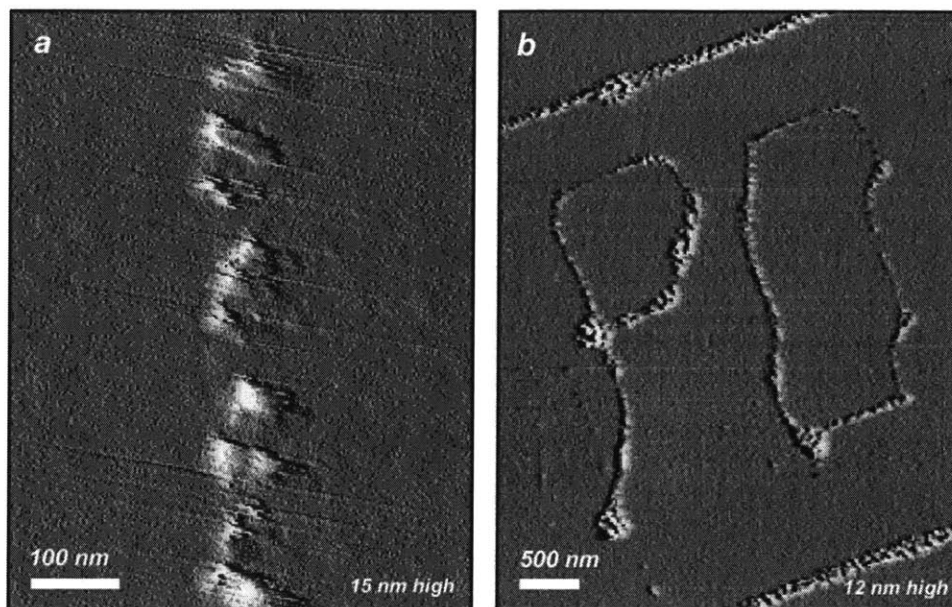


Figure 56 --- Figure 'a': AFM image of liquid-phase lines similar to those shown in Figure 55. Line width was 30-40 nm (FWHM), with heights up to 15 nm. [Ex. q-224-d] -- Figure 'b': Curved liquid-phase silver (30 wt%) lines were used to form the letters "P" and "O" at 1 micron/second. Line width was 50-90 nm. Line height was 6-12 nm. [Ex. q-224-c]

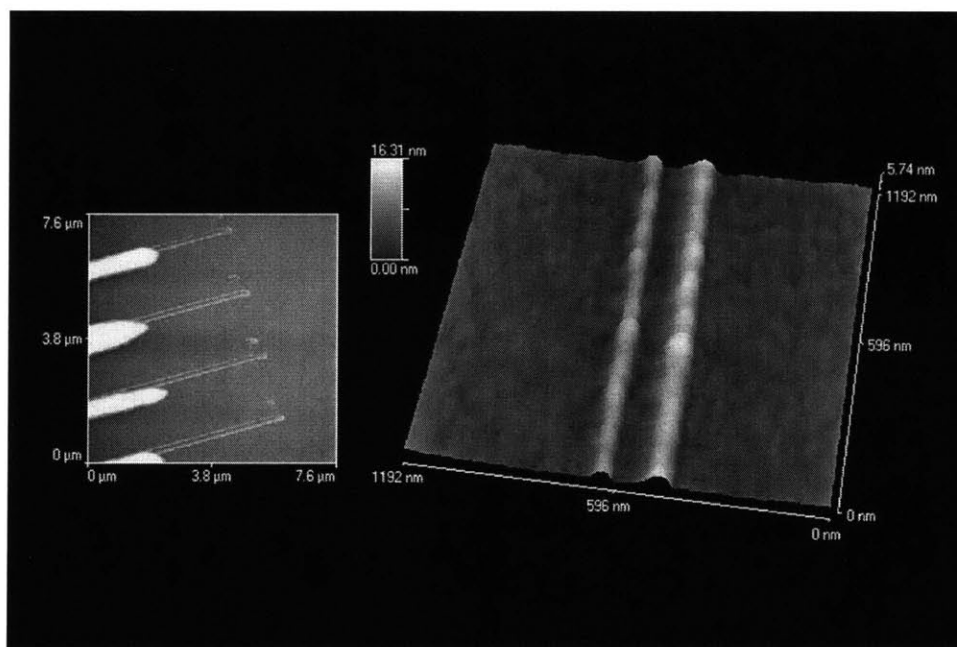


Figure 57 --- Tapping mode double line (separated by 50 nm) of liquid-phase gold (40 wt%) nanoparticle ink on glass at 10 microns/second. The thinner of the two uncured lines was 3.5 nm tall and 45 nm wide (FWHM). [Ex. q-212-c]

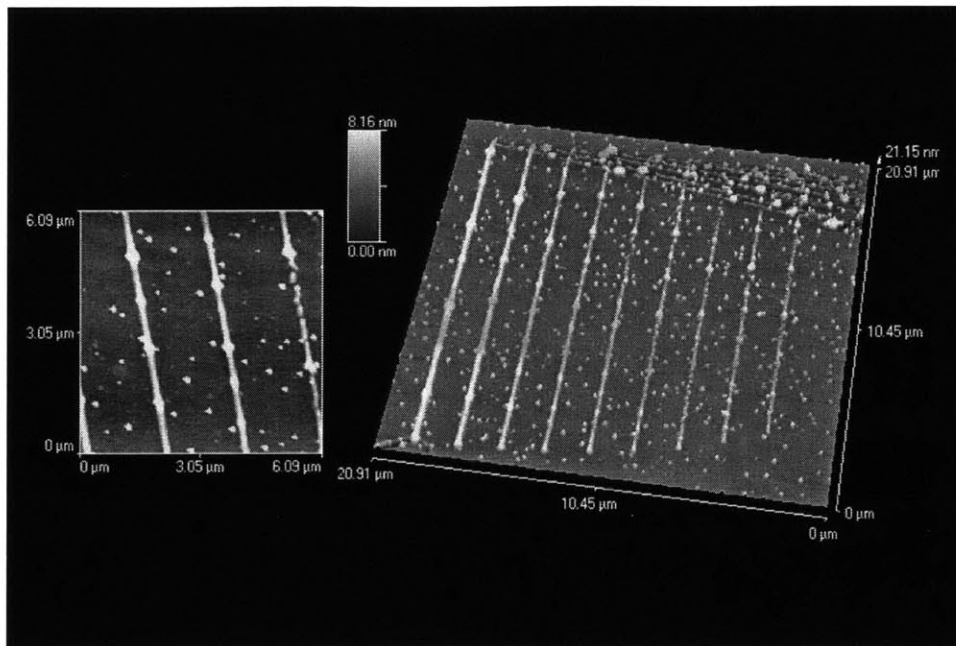


Figure 58 --- Increasing tapping mode tip-substrate pressure increased the width of liquid-phase silver (30 wt%) nanoparticle ink lines drawn at 10 microns/second. The rightmost line received the lightest pressure. Periodic blots were formed. Shock curing of the nearby ink reservoir created particulate debris. No frequency tuning. [Ex. q-200-a]

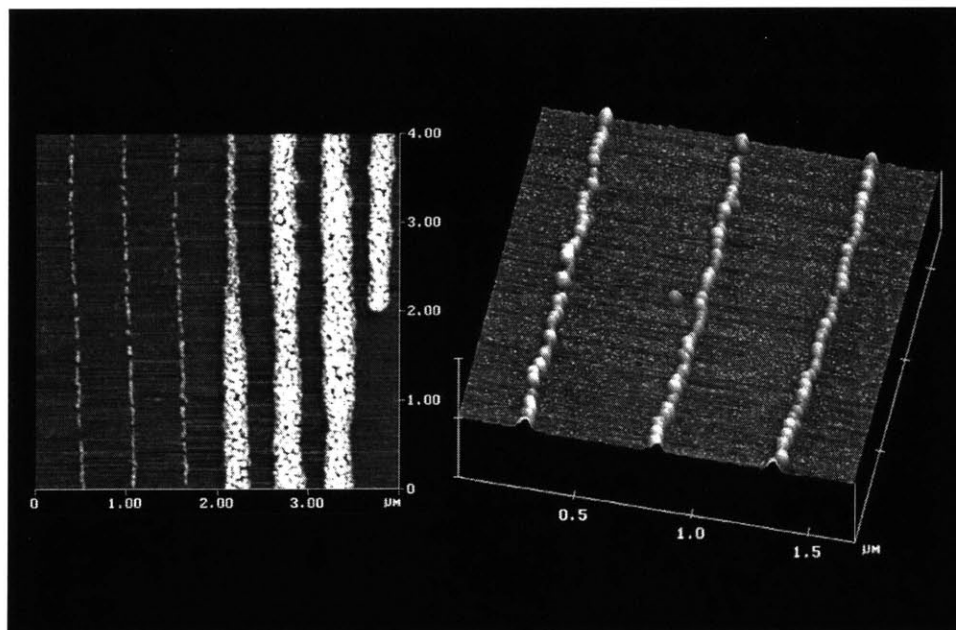


Figure 59 --- The width of solid-phase tapping mode gold (70 wt%) nanoparticle ink lines drawn on glass at 5 microns/sec was increased by higher forces. Line width was increased from 45 to 350 nm. No periodic blots of solid ink were formed. [Ex. q-102]

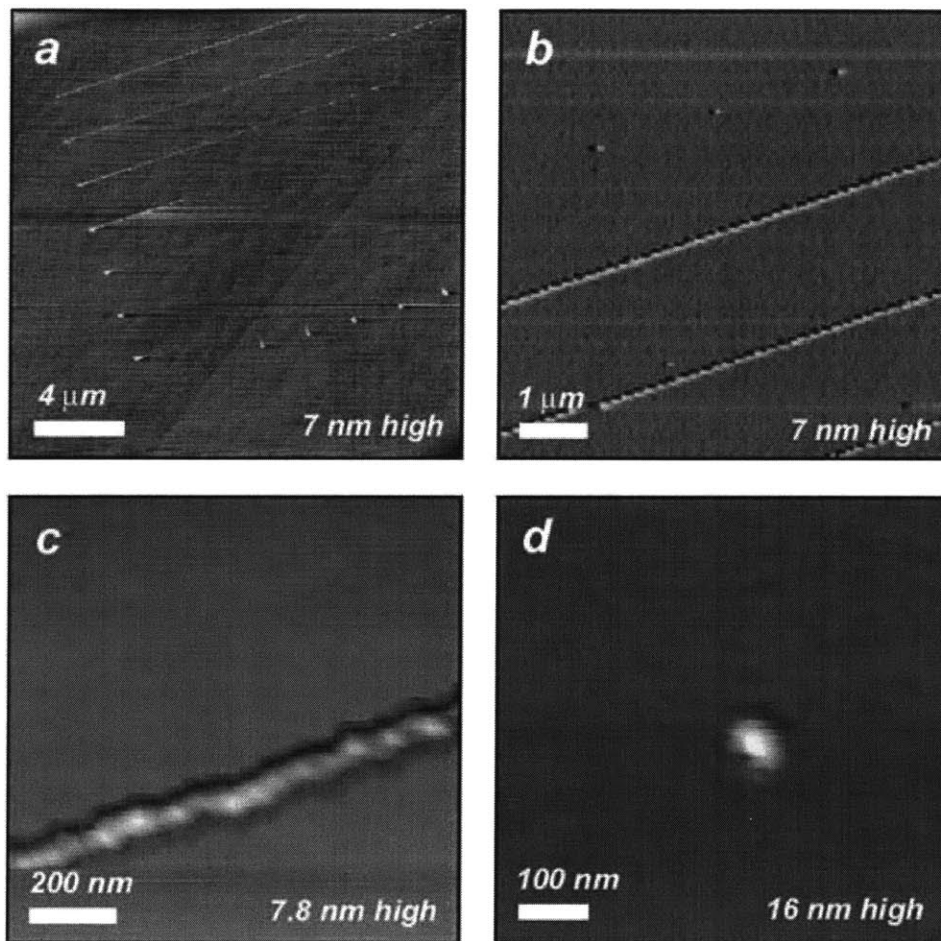


Figure 60 --- Solvent-assisted fabrication of lines using a solvent-soaked tip and tapping mode deposition of solid-phase silver (30 wt%) nanoparticle ink at 10 microns/second. The tip was first soaked in alpha-terpineol, and was then used to withdraw ink from a solid ink reservoir. The top-most horizontal line figure 'a' was deposited first. The lower horizontal lines were sequentially drawn in order, from top to bottom. The lines were formed from left to right. Even though the tip-surface pressure was incrementally increased from line to line, only the first three lines were fully formed. The solvent-ink fluid mixture on the end of the tip eventually ran out during the formation of the fourth line. As shown in figures 'b' and 'c', the lines were nearly uniform in thickness (55 nm FWHM) and height (7.8 nm), and did not exhibit periodic blots of ink along their lengths. The dot in figure 'd' (three more examples of which are barely visible at the top of figure 'b') was 16 nm high and 50 nm across (FWHM) to yield a 0.32 height-width aspect ratio. This dot was formed at the very tail end of a vertically drawn (but invisible) line as the tip was lifted up off the surface of the substrate. All AFM images were obtained while the lines were in an uncured but fully dried state. A dynamic tip frequency tuning procedure was executed just before the formation of each line to ensure proper engagement force. [Ex. q-224-dd]

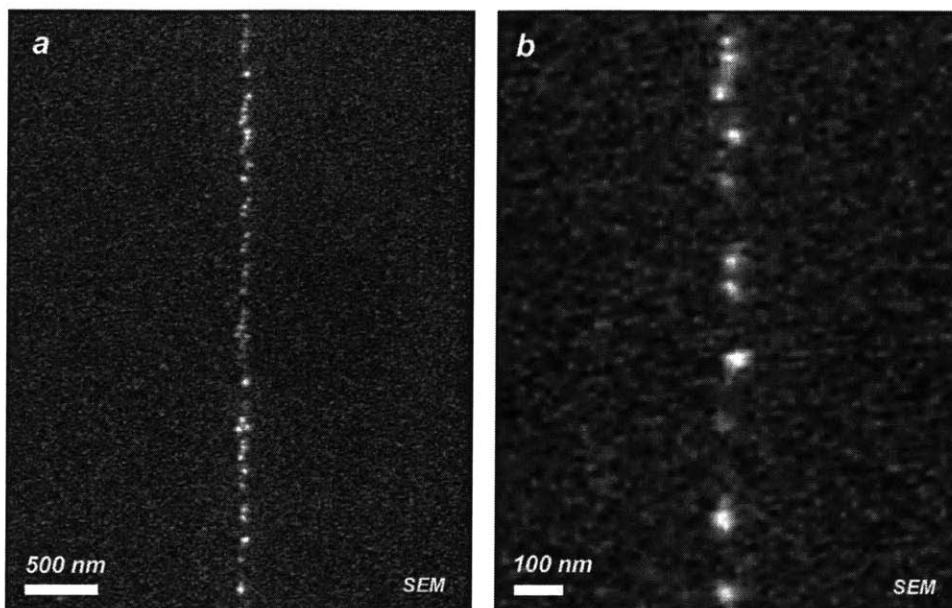


Figure 61 --- SEM images of the solvent-assisted solid-phase silver lines shown in Figure 60 after thermal curing at 450 degrees Celsius. The string of 60 nm particles presented in figure 'b' are separated by relatively long distances of 100 nm or more. [Ex. q-224-dd]

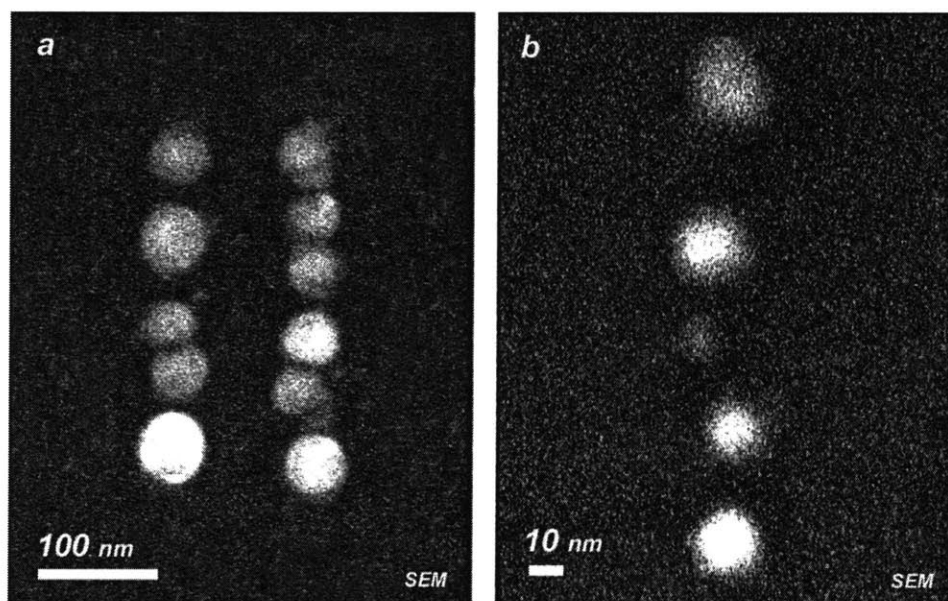


Figure 62 --- SEM views: Figure 'a' shows two very short lines of solid ink separated by less than 100 nm [Ex. q-225-t]. Figure 'b' shows some of the smallest sub-20 nm dots deposited in a line using the "solvent-assisted" method wherein a tapping mode tip is dipped into a reservoir of solvent and then into a reservoir of solid-phase ink. It is likely that a single nanoparticle is contained with each of these very small dots [Ex. q-225-dd].

-
-
- [a] Seiko Epson (<http://www.ea.epson.com>) claims that its Stylus 900 Color ink jet printer product contains piezo heads that are capable of generating the world's smallest ink droplets with a volume of 3 picoliters. The printer has a rated resolution of 1440 dpi. Consumer testing and measurement conducted in April 1999 showed that the Stylus 900 dots are 33 microns across on certain photo-quality ink jet papers (see **cached** article). For comparison, a 10 pL droplet generates a 70 micron dot, and a 6 pL droplet generates a 45 micron dot, and a 0.5 pL droplet (if ever achievable) would generate a 14 micron dot.
- [b] A series of multi-layer dots were deposited using solid-phase ink from an ink pool reservoir that had been allowed to dry for 180-186 minutes (~3 hours) before the nanoassembly process was initiated. Originally, the ink contained a very high solid fraction of gold nanoparticles (40 wt% gold). Solid phase ink; contact mode for dipping and writing. Dots were 5 and 100 layers tall. [Ex. q-237-j]

3D NANOASSEMBLY

Multiple-layer structures

With the successful demonstration of the two-dimensional nanoassembly technique, as described in the previous sections, many of the project's major goals are achieved. Primary among these goals is the demonstration of a system and process that is capable of nano-scale all-additive patterning of useful materials onto various substrates over a wide range of environmental conditions using discrete 'pick-and-place' operations. The nanoassembly system handles multiple substances with widely varying properties, and both build materials and sacrificial materials may be patterned at nanometer scales. This characteristic is a key requirement for the fabrication of useful three-dimensional (3D) devices such as MEMS, wherein the sacrificial materials are typically etched away leaving behind free standing and over-hanging structures such as cantilevers and bridges. Naturally, the next tantalizing goal is the formation of 3D structures such as columns and walls with significant height-to-width aspect ratios. Preferably, the aspect ratio should be 1.0 or greater. For the purposes of this project, the width of a structure is determined by its full-width-half-max (FWHM) dimension. The full-width of the structure is measured at an elevation that is half-way between the top and the bottom of the structure.

Using only room temperature processes and no special assistance, the nanoassembly system has the ability deposit multiple-layer structures, wherein each additional layer of material contributes significantly to the overall height of the structure being fabricated. In general, the same sharp tip that is used to pick up material from the reservoir can also be used to repeatedly add material to the top of an extant structure without subsequently removing material from that structure. This is a non-intuitive result, particularly when working with solid-phase inks. For example, once a multi-layer solid-phase dot becomes large enough, it begins to resemble an ink pool or reservoir itself. One might expect that subsequent deposition steps would cause the tip to remove ink from the dot in a fashion similar to the way that the tip removes material from the original ink reservoir. However, this effect does not generally occur, and the deposited dots very rarely exhibit a tip-shaped crater or even the slightest indentation at their centers.

Multi-layer dots that are many tens or hundreds of layers tall have been fabricated. The tallest structure ever constructed by the nanoassembly system, without special assistance from other processes, was a 100-layer dot using a viscous liquid-phase ink. The multilayer dot was 2 microns in height and 8 microns across (FWHM), to yield a respectable aspect ratio of 0.25 [Figure 63]. It is likely that 2 microns of height is more than sufficient for the manufacture of interesting nano-scale or micro-scale 3D structures.

In general, dots with more layers are generally taller than dots with fewer layers. However, the increased height is usually accompanied by increased lateral dimensions, and the height-to-width aspect ratio increases only slightly as the layer-count goes up. During a single experimental run, a 1-layer, a 5-layer, and a 100-layer dot were created [Figure 64]. The aspect ratios of the dots were 0.10, 0.17, and 0.22, respectively. When comparing the 100-layer dot to the 1-layer dot, a 100-fold increase in the number of layers and a 10-fold increase in overall height netted only a 2-fold increase in the aspect ratio.

The aspect ratio of a multi-layer dot can be improved by switching from a liquid-phase ink to a solid-phase ink. For example, a 100-layer dot of solid-phase ink was 120 nm tall and only a bit more than 300 nm in diameter (FWHM), to yield a 0.36 aspect ratio [Figure 65]. A very promising aspect ratio of 0.46 was achieved with a 200-layer dot that was 180 nm tall and just over 400 nm across. It should also be noted that 400 nm is just slightly more than 10 times the width of the highest-resolution single layer dot ever deposited, and yet contains 200 times as many layers of ink.

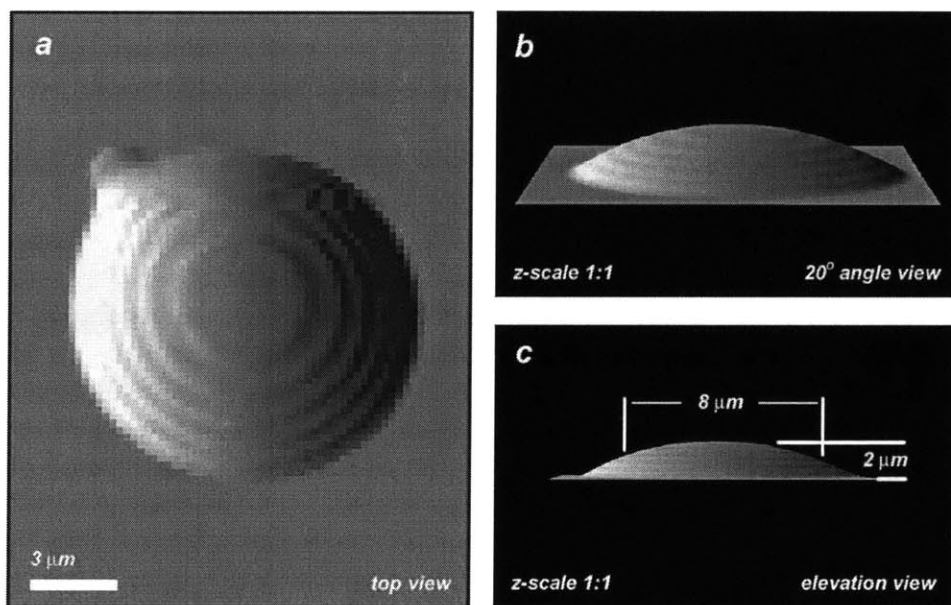


Figure 63 --- The tallest dot ever constructed by the nanoassembly system (without assistance from other processes, such as thermal curing, etc.) is 2 microns tall and contains 100 layers of a very thick liquid phase ink. The aspect ratio is 0.25 (8000 nm FWHM and 1946 nm tall). The ink was deposited using contact mode. [Ex. q-232-b]

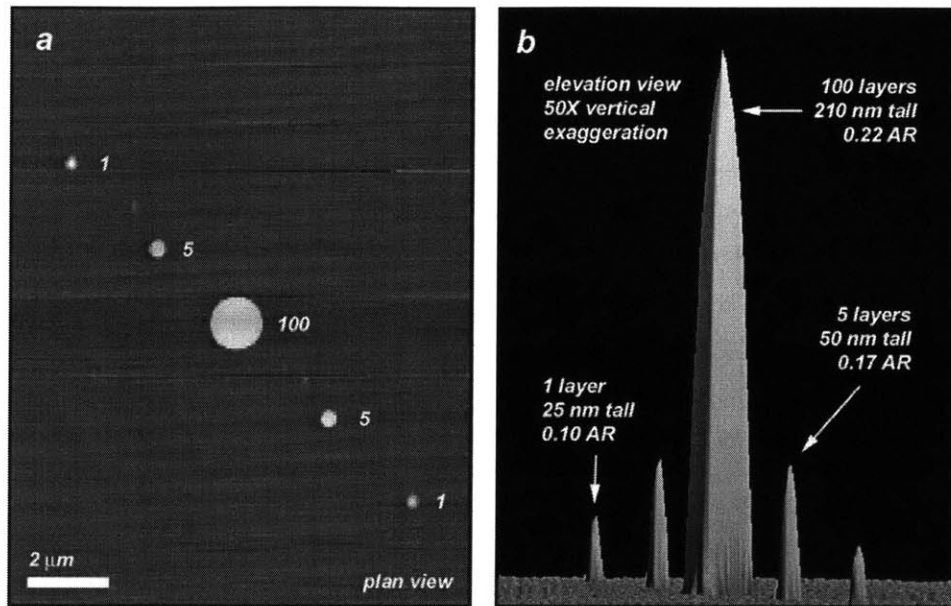


Figure 64 --- A liquid phase ink and contact mode was used to deposit 1, 5, and 100 layer dots with widths of 230, 290, and 935 nm (FWHM), respectively. The 100-fold increase in the number of layers yielded only a 2-fold increase in the aspect ratio. [Ex. q-232-g]

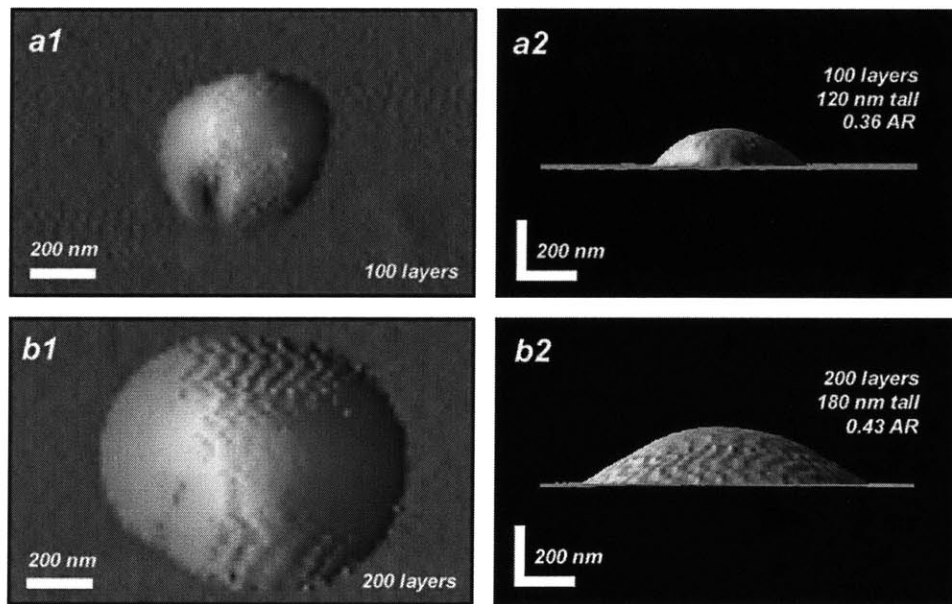


Figure 65 --- Solid phase inks and contact mode can be used to increase the aspect ratio, when compared to liquid inks. The 100-layer dot in figures 'a1' & 'a2' is 120 nm tall and 327 nm FWHM, with an aspect ratio of 0.36. [Ex. q-232-k] The 200-layer dot in figures 'b1' & 'b2' is 180 nm tall and 414 nm FWHM, with an aspect ratio of 0.43. [Ex. q-232-m]

Laser-assisted nanoassembly

As shown in the previous section, multi-layer nanoassembled structures generally become larger in diameter as the number of layers is increased. Repeated deposition at the same location results in the formation of a taller and wider dot instead of a more desirable high-aspect ratio column. It is likely that the deposited material is too soft to withstand the impact force of the tip as it deposits additional layers onto the top of the growing structure. This soft material “slumps” down and to the sides, causing the girth of the dot to increase nearly as rapidly as the increase in height. For some ink materials, such as nanoparticle inks, localized thermal treatment of the dot after the deposition of each layer can cause a liquid or soft-solid ink to be transformed into a hard and thoroughly dense solid phase that will resist “slumping”. For example, gold nanoparticle and silver nanoparticle inks undergo a dramatic transformation from a non-conductive particle-in-solvent fluid to a solid metal film with 25% of the conductivity of the bulk metal when thermally cured at relatively low temperatures between 200 and 350 degrees Celsius. Locally-confined thermal curing of the deposited ink dot is desirable in order to keep curing times at a minimum, and to keep the nearby ink reservoir in an uncured state. Therefore, the peltier system that was used to for global substrate heating and cooling was not appropriate for this application. Low time-constant (<10 microseconds) thermal cantilevers provided by Yiching Liang of the Tom Kenny group at Stanford University, could have provided a promising route for this work. Unfortunately these cantilevers have tips that are extremely short (very short cone protrusion) which makes working with liquid materials very difficult, due to flooding effects. In addition, the root silicon material to which each cantilever is attached overhangs the cantilever body, and blocks the laser beam required for feedback controls, resulting in very low signal strength at the detector. Despite multiple attempts, no pick-and-place operations could be reliably carried out with the provided thermal cantilevers. The time and effort required to design and built custom thermal cantilevers with the proper characteristics specifically tailored for the 3D nanoassembly application using conventional silicon processing techniques is beyond the scope of this project.

Thermal curing with a laser beam provided both of the desirable characteristics of a thermal cantilever, namely a short thermal time constant and high spatial selectivity. A suitable laser source was easily found. An IRE-Poulus Group model YLD-5000 ytterbium fiber infrared laser emitting at 1060 nm was used to supply up to 5 watts of optical power. Conversion of the near-collimated laser beam into a tightly focused and precisely directed spot within the 100x100 micron build zone on the substrate proved to be a challenge, however. The laser beam had to be directed down through the main body of the AFM head without damaging the nearby cantilever or thermally affecting the ink reservoir. The beam spot size could be no larger than 20 microns across because the build zone was often positioned less than 50 microns away from the edge of the ink pool

reservoir. Also, frequent adjustment of the control knobs on the side of the AFM head and the need for an intervening shutter, beam splitter, and focusing lens prevented the laser source from being any nearer than 12 inches from the substrate.

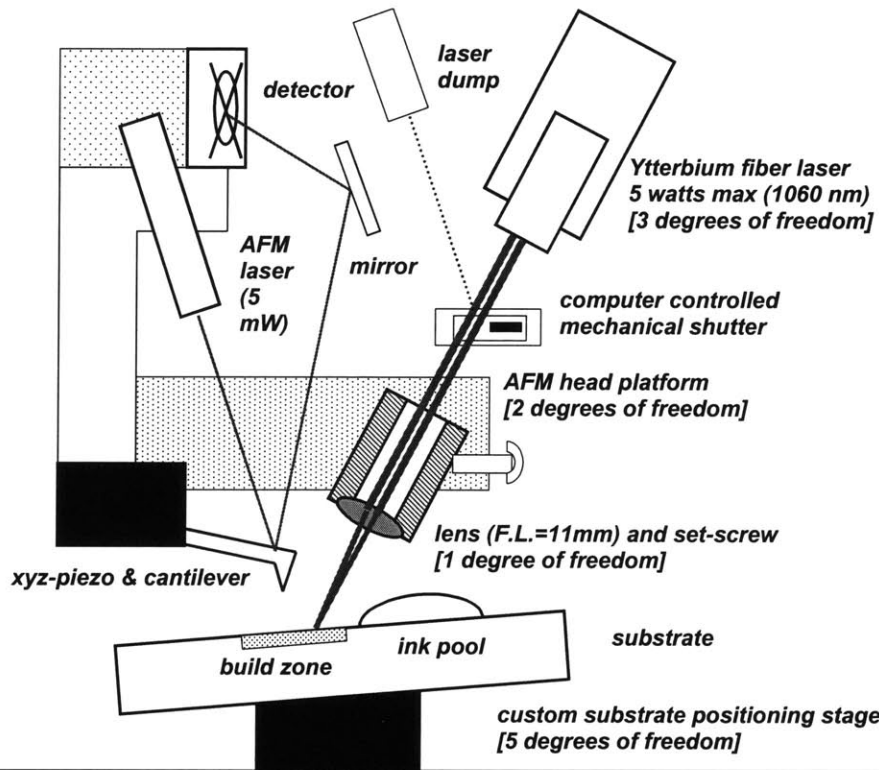


Figure 66 --- Apparatus arrangement for laser-assisted three-dimensional nanoassembly experiments. The infrared laser source, focusing lens, AFM head assembly, and substrate positioning stage all allow multiple degrees of freedom of translation and rotation. This flexibility was useful for precision alignment of the infrared laser beam to the build zone on the substrate.

Several complete laser curing arrangements, including five different positioning stage designs, were built before an optimal implementation was achieved. The total laser curing system [Figure 66] consisted of a laser source on a rotating mount, computer controlled shutter for beam modulation, beam dump, focusing lens, AFM head alignment stage, and a camera beam blocker. The infrared laser beam [Figure 67] was focused down to a 20x10 micron spot on the substrate using an 11 mm focal length lens at the end of a metal

tube inserted into the side of the AFM head. This metal tube in the head was originally used hold the light source for general illumination of the cantilever when viewed through the CCD camera. To obtain the smallest spot size, the lens was positioned about 11mm away from the substrate. Timed laser beam exposure was enabled by a solenoid-driven shutter placed between the laser source and the focusing lens. Laser bursts as short as 50 ms were triggered by timing signals output from the computer during the execution of lithography runs. The CCD camera on the AFM head was protected from the laser beam by a custom beam blocking mechanism attached to the rotating focusing wheel of the camera. The AFM head was mounted on top of the standard substrate positioning stage, which itself was mounted on top of a custom positioning stage [Figure 69] that provided fine control of the horizontal location, lateral location, roll, pitch, and yaw of the AFM head relative to the incoming laser beam. When fully assembled, the final design [Figure 68] provided 1-micron resolution placement of the laser spot anywhere on the substrate within several hundred microns of the cantilever.

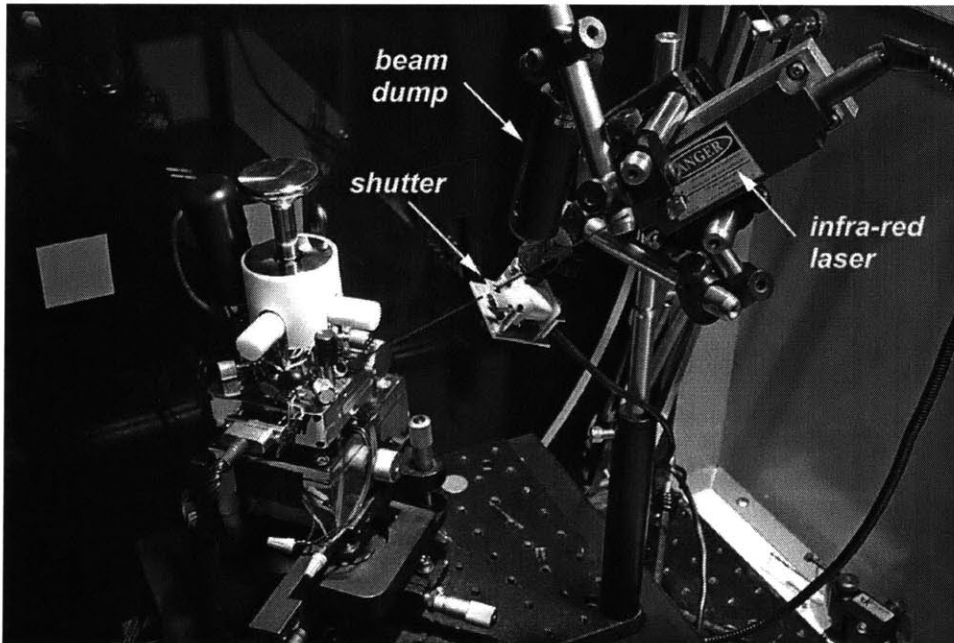


Figure 67 --- The infrared laser source is aimed directly into the heart of the AFM. The laser beam is modulated by a computer controlled mechanical shutter, with excess energy being absorbed by a beam dump.

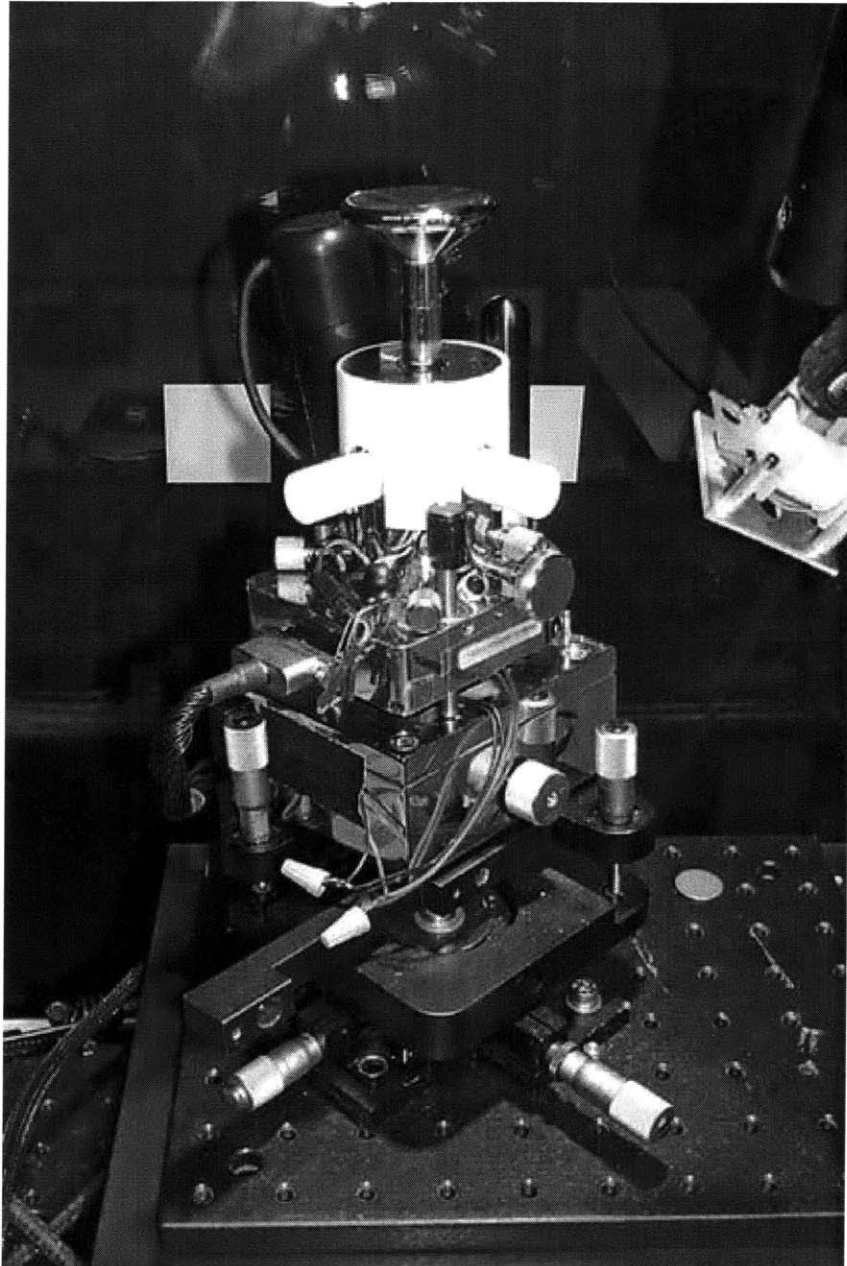


Figure 68 --- When the head of the AFM is placed on top of the custom laser beam alignment stage, the total assembly was tall but stable. For most laser-assisted nanoassembly operations, the vibration isolation was provided by a single layer of carpet and two layers of bubble wrapping under the metal base plate.

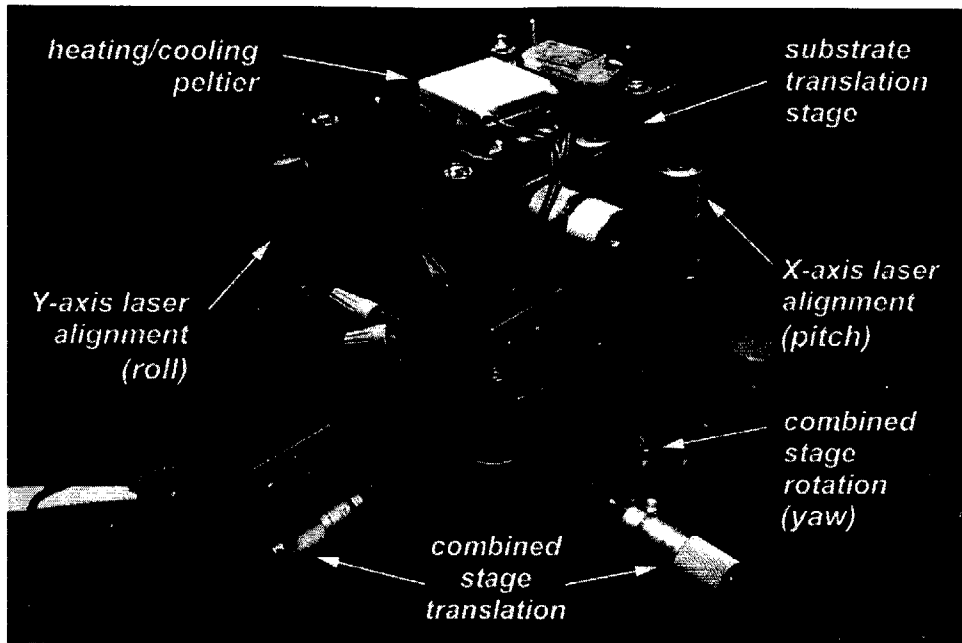


Figure 69 --- Precision alignment of the infrared laser beam within the construction zone on the substrate was enabled by a custom positioning stage. This stage provided 5 degrees of freedom for the AFM head relative to the incoming laser beam including yaw, pitch, roll, and X-Y translation. Z-axis translation was handled by either the feet on the AFM or the vertical slider attached to the laser source. Fine positioning of the laser spot along the X and Y axes within the construction zone was provided by pitch and roll micrometers, which pivoted the AFM head left-to-right and front-to-back. In-situ cooling and heating of the substrate is carried out with a double-stacked peltier system.

Procedures for carrying out laser-assisted nanoassembly experiments were considerably more complex than those for simple non-assisted room-temperature techniques. Before any lithography was begun, the laser was aligned to the center of the build zone on the substrate using a series of pre-run operations [Table 13]. An automated script delivered a number of short laser bursts to the surface of a “dummy” air-dried pool of ink on the substrate. Then AFM imaging methods were used to determine the location of the thermally cured area relative to the cantilever and the desired build zone. Corrections to the beam spot position were handled by manual adjustments to the micrometers on the custom laser alignment stage.

In addition, the computer scripts used to carry out automated laser-assisted construction were somewhat different from their non-assisted counterparts. A typical non-assisted pick-and-place lithography script directed the tip to dip into the ink reservoir, withdraw,

translate to the build zone, deposit a dot of ink onto the substrate, withdraw, and finally return to the reservoir once more. The scripts used for laser-assisted nanoassembly included a few extra steps at the end of each deposition cycle. Instead of returning immediately to the ink reservoir, the tip was directed to move to a "parking location" at the far corner of the 100x100 micron scan area (which was the translation limit of the X-Y piezos) where it could not be damaged by the laser beam [Figure 70]. To initiate the thermal curing step, the computer sent a TTL signal to an amplifier, which opened the solenoid-driven mechanical shutter for a short duration of several tens to hundreds of milliseconds. The shutter was then closed, and finally the tip was allowed to return to the ink reservoir for another dipping procedure. Depending on the specific script used, intermittent laser curing was conducted after the deposition of every dot of material, or after every five dots of material.

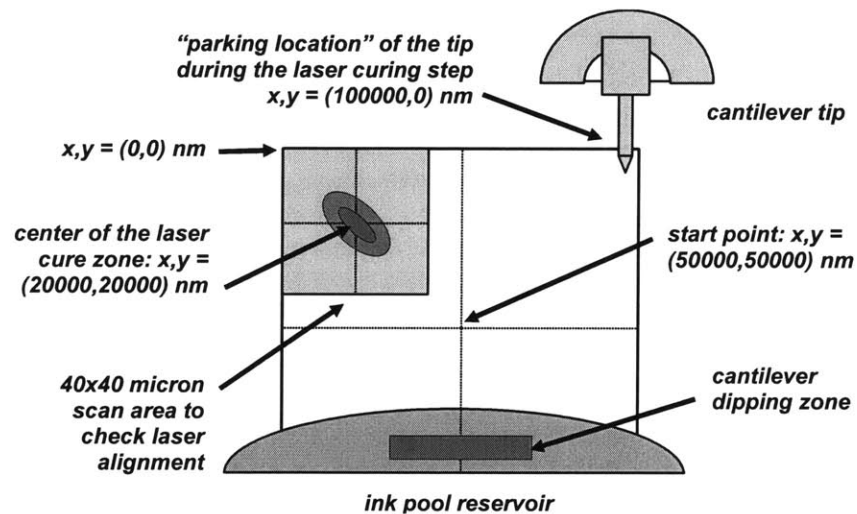


Figure 70 --- Overhead view of the laser curing zone, ink pool, and cantilever parking positions superimposed on the 100x100 micron scan limits of the piezo driven cantilever. The laser beam hits the substrate at an angle from the left. The beam is focused by an 11 mm focal length lens at the location of $x,y = (20,20)$ microns. Alignment of the beam is checked by laser curing a thin air-dried "dummy" pool of ink, and then obtaining a 40x40 micron AFM scan of region closest to $x,y = (0,0)$. The laser beam is properly aligned when the observed laser cure zone within the pool of ink located is at the very center of the 40x40 micron scan. During automated laser-assisted lithography operations, the tip is parked out of the way at $x,y = (100,0)$ as the laser beam shutter is opened.

Table 13 --- Pre-run and laser alignment procedures for laser-assisted nanoassembly

| step | procedures |
|--|--|
| <p>pre-run setup procedures</p> | open original factory-installed Thermomicroscopes imaging software |
| | set AFM head knobs so that the internal laser sum < 7.5 nA, L-R = -0.5 nA, and T-B = -0.5 nA |
| | open LithoLab custom lithography software, set the scan size to be 100 microns, and turn on the AFM head internal laser |
| | adjust X-Y knobs on the substrate positioning stage so that the tip is located over a clean area of the substrate |
| | <p>manually type in the following commands in order:</p> <p>scrncoff2(), scrzz(7000), scrsetsetpoint(6), scrtipapproach(), scrsetsetpoint(-60)</p> |
| | confirm that the tip is hovering just above the surface (but is still in feedback), turn off AFM head internal laser, and remove the AFM head light bulb |
| <p>ROUGH LASER ALIGNMENT</p> <p>(assumes a build area located at x,y=20000, 20000 nm)</p> | scr10out1(2.0,500) |
| | <p>once the IR shutter is open, increase the IR laser output to 100 mA (which corresponds to a laser spot that is just barely visible when reflecting off the substrate using the AFM head CCD camera)</p> <p>Note: although not visible to the naked eye, the infra-red laser beam spot is easily detected and imaged by the CCD camera</p> |
| | scrxy(55000,32000,100) |
| | adjust any of the four knobs on the custom AFM head angle alignment stage so that the IR laser spot forms a thin crescent around the end of the tip |
| | scrxy(55000,15000,100) |
| | confirm that the IR laser spot is completely visible (unblocked by the end of the tip) by the CCD); adjust the position of the AFM head angle alignment stage if required |
| | scrxy(55000,35000,100) |
| | confirm that the IR laser spot-tip interference pattern imaged by the CCD looks like an "X" right at the end of the tip; adjust the position of the AFM head angle alignment stage if required |

| | |
|--|--|
| <p>FINE LASER ALIGNMENT</p> <p>(assumes a build area located at x,y=20000, 20000 nm)</p> | <p>scrxy(50000,50000,100)</p> |
| | <p>use the substrate positioning stage to position the tip just inside and hovering just over the edge of a pool of air-dried diluted (5-10 wt%) silver or gold nanoparticle ink</p> |
| | <p>execute a scripted code that provides eighteen 50 ms long IR laser bursts using a laser current of 297 mA (which corresponds to a laser power of approximately 50 mW when measured directly at the laser source); [code132.txt]</p> |
| | <p>scr10out1(-2.0,500)</p> |
| | <p>once the IR laser shutter is closed, turn off the emission of from the IR laser unit (if still on), disengage the tip, and re-insert the light bulb into the AFM head</p> |
| | <p>without moving the substrate, use the original Thermomicroscopes software to obtain a 40x40 micron image the laser cured area within the ink pool (at 0 degrees scan); the 40x40 micron scan area must be placed in the upper left hand corner of the 100x100 micron total available scan area near the coordinates x,y=0,0.</p> |
| | <p>the IR laser is perfectly aligned when the laser cured area within the ink pool (which should be visible as a 20x30 micron depression in the ink pool) appears in the very middle of the 40x40 micron scan area when imaged by the AFM; use manual adjustments of the X and Y knobs on the custom AFM head angle positioner to place the next laser curing attempt as close to x,y=20000,20000 as possible using the following rules:</p> <p>the laser cured area is moved down (in +Y direction) in the AFM image by decreasing the value shown on the knob of the Y position micrometer (and vice versa); the laser cured area is moved to the right (in +X direction) in the AFM image by decreasing the value shown on the knob of the X position micrometer (and vice versa)</p> |
| <p>repeat laser curing, AFM imaging, and alignment adjustment as required until the laser cured area is as close as possible to x,y=20000,20000 (in the center of the 40x40 micron scan area in the upper left hand corner of the total scan area)</p> | |
| <p>position the tip relative to the ink pool</p> | <p>scr10out1(-2.0,500)</p> |
| | <p>scrxy(50000,50000,100)</p> |
| | <p>use the substrate positioning stage to position the tip just inside and hovering just over the edge of a new ink pool to be used as the material reservoir for subsequent fabrication of nano-structures</p> |

| | |
|------------------------------------|---|
| load and execute the script | load the desired lithography script code |
| | remove light bulb from the AFM head and rotate the custom laser blocker device to protect the CCD camera from the IR laser beam |
| | set the IR laser to the correct power output (watts and amps) and begin emission |
| | execute the automated script to begin the run; wait for the nanoassembly run to conclude |
| shut down | scr10out1(-2.0,500) |
| | once the IR laser shutter is closed, turn off the emission of from the IR laser unit (if still on), disengage the tip, and re-insert the light bulb into the AFM head |

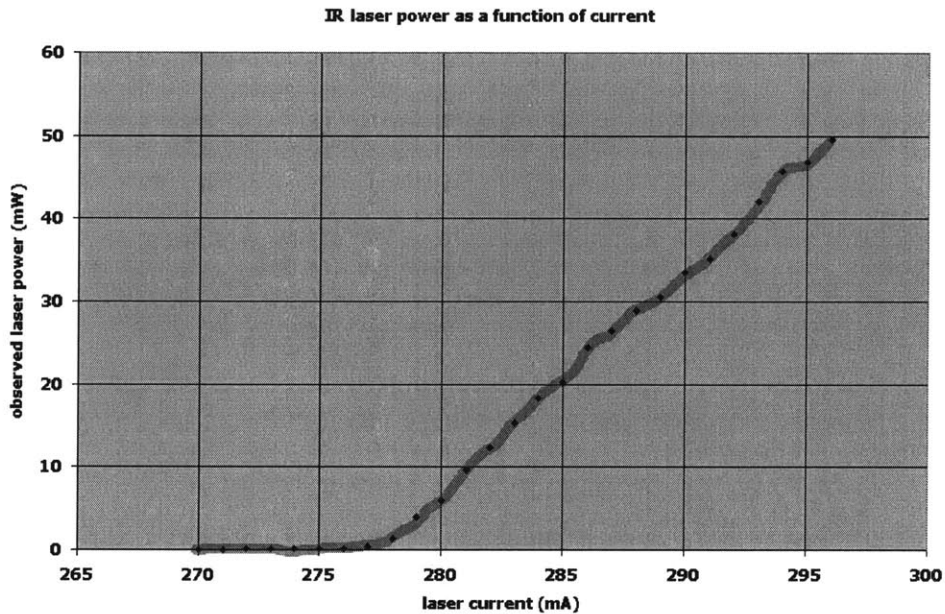


Figure 71 --- A plot of infra-laser power emitted from the ytterbium fiber laser source as a function of the applied current. The power was measured within 2 mm of the source with a Coherent 'Labmaster LM-2' detector. Linear power output was reached above 5 mW at 280 mA of applied current. The detector had a power limit of 50 mW.

Precise control over laser power and exposure times was crucial during laser-assisted experiments. As expected, the area of the thermally affected zone increased as a result of increased laser power [Figure 72]. However, the quality of the cure was also dramatically altered by even a change of a few milliwatts of power. Even though the laser was operating in a linear power output regime [Figure 71], any deposited structures that were exposed to the laser beyond a certain power threshold were damaged in some way. A dot that was deposited in the liquid phase was usually blown flat into a cohesive pool ringed with tiny droplets by excessive laser power, and solid phase dots were often instantly converted into piles of particulate debris [Figure 73]. When over-heated by the laser, highly viscous dots exhibited both the pool-like and particulate characteristics of liquid and solid phase depositions.

Despite a multitude of attempts, no significant improvement in the overall height or aspect ratio of deposited multi-layer structures was obtained by using the laser-assisted fabrication method. This general finding was the case for both solid phase [Figure 74] and liquid phase [Figure 75] depositions. This finding is best illustrated by a solid phase lithography attempt wherein two sets of multi-layer dots were fabricated at opposite corners of the 100x100 micron scan area [Figure 74 --- 'a' and 'b']. In order to factor out the possible effects of hardening of the material reservoir over the duration of the 4-minute lithography run, the two identical sets of dots were deposited simultaneously. The set of dots that was deposited within the laser curing zone was exposed to a 50 ms burst after every deposition cycle, while the other set of dots received no direct laser exposure at all. At the conclusion of the run, the deposited structures were imaged using standard tapping mode AFM imaging techniques. The laser-cured and non-cured dots were found to have nearly identical heights and aspect ratios. In fact, for this particular experiment, the non-cured dots were about 25% taller than their laser-cured counterparts. Confirmation of adequate laser power to cause sufficient curing and perfect laser alignment for the laser-cured set of dots was provided by the small amount of laser-initiated particulate debris found nearby these structures.

The laser-assisted nanoassembly method may not have yielded depositions with superior aspect ratios because the curing step occurred after the tip was removed from the dot being deposited. Due to the very significant interface forces that operate at the nanometer scale, the uncured deposition may have been drawn down into intimate contact with the pre-existing structure immediately after the tip was withdrawn from the surface. There was no scaffolding (such as the tip itself) to hold the new deposition in place while the laser-initiated hardening was conducted. It is also possible that the forces exerted by the tip at the point of impact with the surface may have been large enough to cause the structure and any new deposition to be flattened. Because the laser-curing step was conducted after the moment of impact, the new deposition was likely to be easily flattened by the forces applied by the tip.

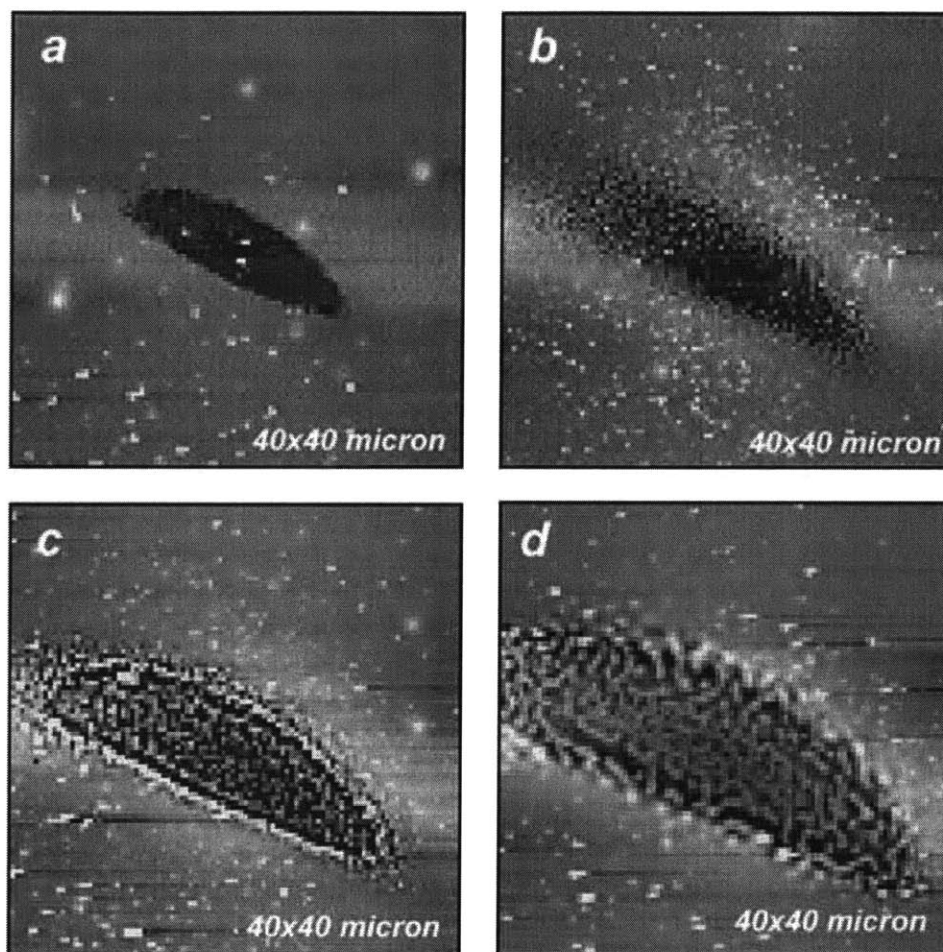


Figure 72 --- The area of the laser-cured zone increased with increasing laser beam power. Figures 'a' through 'd' show the effect of laser-curing an air-dried pool of silver nanoparticle ink at applied laser currents of 290, 300, 310, and 330 mA, respectively. The scripted code executed eighteen 50 ms long laser bursts. [Exp. q-233-c] A 50-50 beam splitter was used near the source, so the power reaching the substrate after the splitter and focusing lens is projected to be substantially less than 18, 30, 42, and 66 mW, respectively [see Figure 71]. However, no beam splitter was used for any experiments presented in the following figures [see Figure 73 through Figure 75].

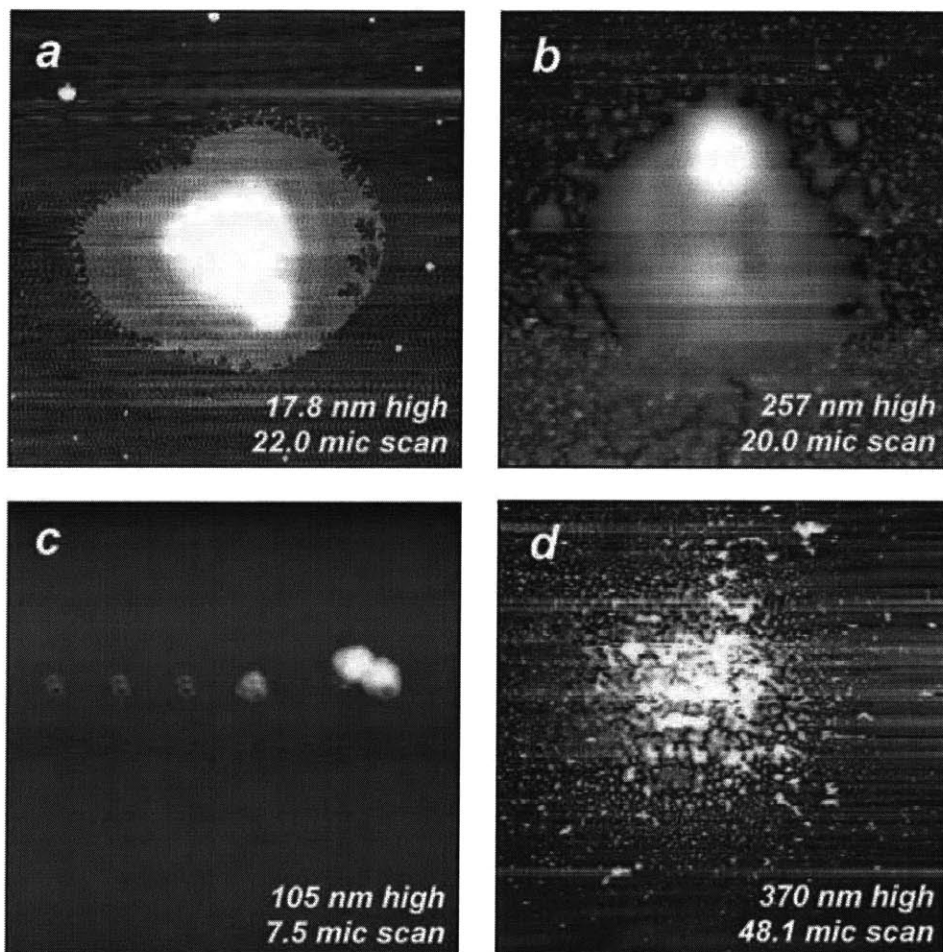


Figure 73 --- Excessive laser power during and after nanoassembly operations with liquid and solid phase inks had a dramatic effect on the quality of the deposited structures. Structures formed from liquid phase inks were blown flat by the laser, while depositions of highly viscous and solid phase inks were obliterated into particulate debris. The puddle-like 40-layer deposition of liquid phase silver nanoparticle ink shown in figure 'a' was exposed to 50 ms laser bursts at 305 mA laser current between each deposition step. [Exp. q-233-e] The 100-layer deposition of exceedingly viscous gold nanoparticle ink shown in figure 'b' was easily disintegrated by 300 ms laser bursts at 320 mA laser current between every five deposition steps. [Exp. q-234-v] The multilayer silver nanoparticle dots, shown in figure 'c', were deposited using 50 ms laser bursts at 290 mA laser current, but looked identical to their non-laser cured counterparts. After construction, the solid phase laser cured structures presented in figure 'c' were subsequently destroyed by exposure to eighteen 50 ms laser bursts at 305 mA laser current, as shown in figure 'd'. [Exp. q-233-j]

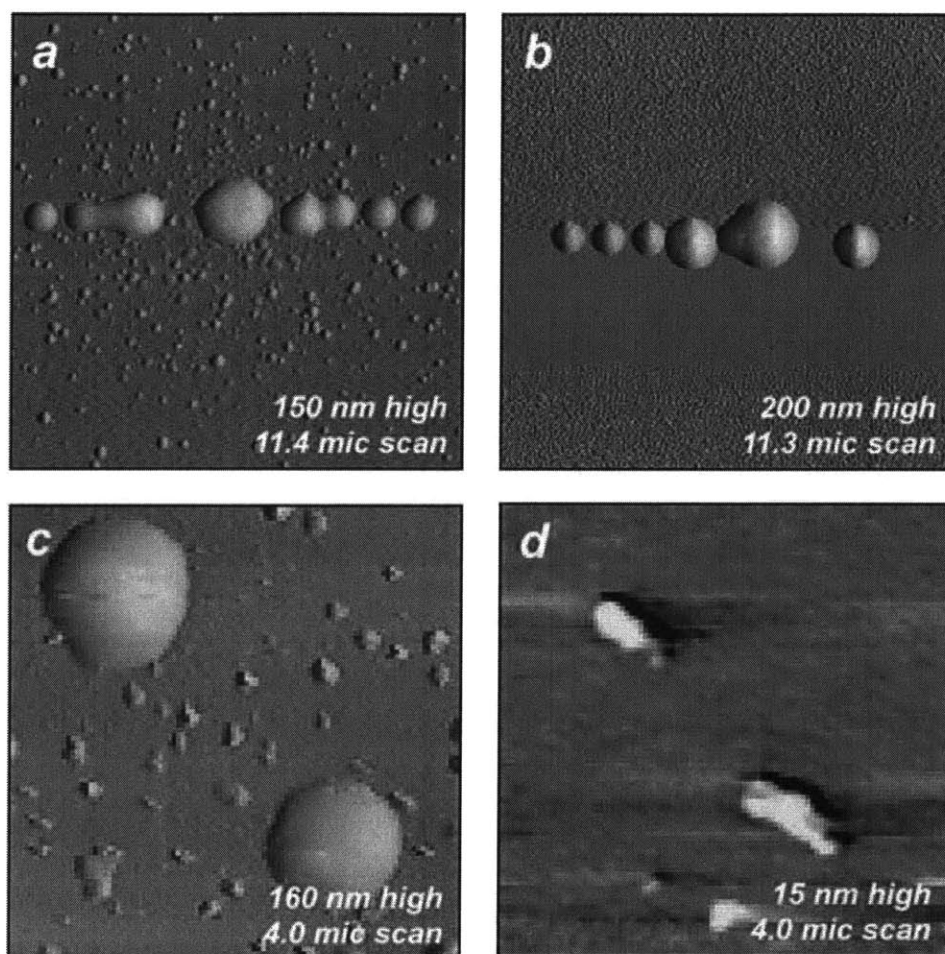


Figure 74 --- In general, intermittent laser curing of solid phase multilayer depositions had no effect on the aspect ratio or over all height of the resulting structures. The single-layer, 5-layer, and 40-layer dots shown in figure 'a' were laser cured with 50 ms laser bursts at 290 mA laser current between each deposition step, while the dots shown in figure 'b' received no laser curing. Both sets of dots were formed in parallel (simultaneously) to factor out the effects of ink pool hardening over the time of the lithography run. The small amount of particulate debris surrounding the dots in figure 'a' is an indication that the laser was correctly aligned over the construction zone and was emitting sufficient power to just slightly over-cure the silver nanoparticle ink material. [Exp. q-233-l] The structures shown in figures 'c' and 'd' were fabricated during different experimental runs, but the results for laser cured and non-laser cured dots for both runs were nearly identical. The 100-layer dots in the upper left corners of both figures were not laser cured, while the 100-layer dots presented in the lower right corners were exposed to 300 ms laser bursts at 305 mA laser current after every 5 deposited layers. [Exp. q-234-x and q-234-z]

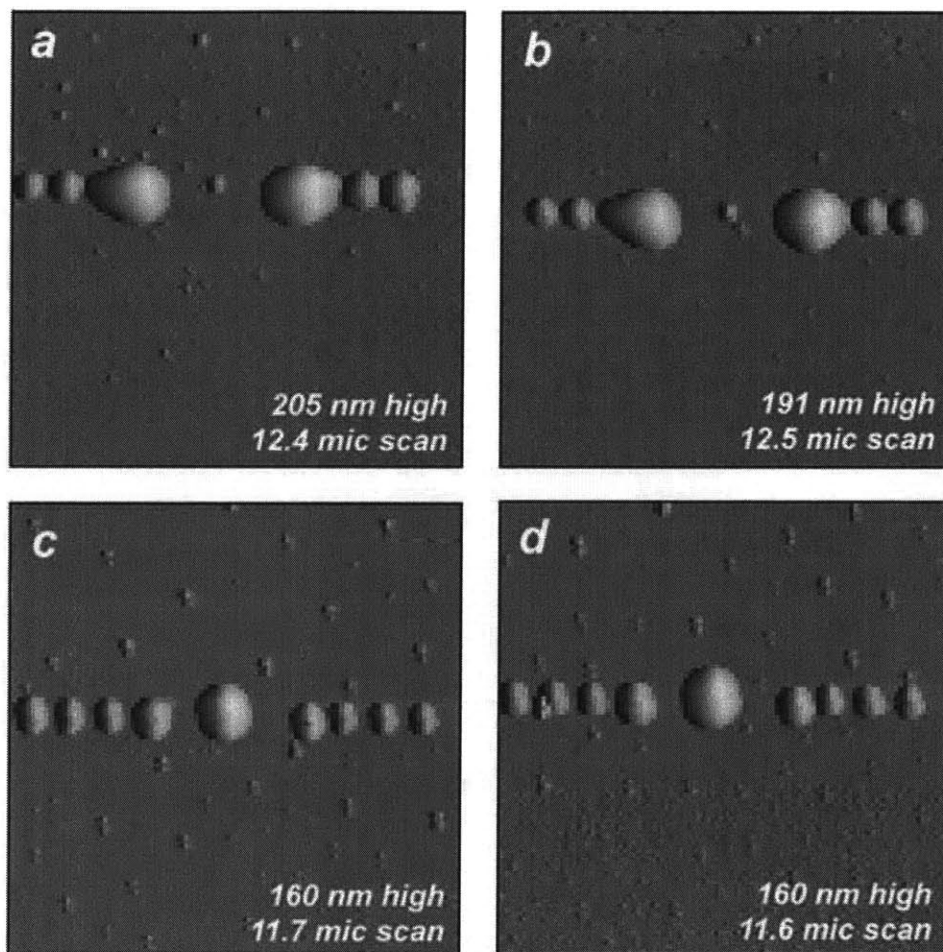


Figure 75 --- In general, intermittent laser curing of liquid phase multilayer depositions had no effect on the aspect ratio or over all height of the resulting structures. The single-layer and 5-layer dots shown in figure 'a' were laser cured with 50 ms laser bursts at 288 mA laser current between each deposition step, while the dots shown in figure 'b' received no laser curing. Both sets of dots were formed in parallel (simultaneously) to factor out the effects of ink pool evaporation and phase changes over the duration of the build procedures. [Exp. q-233-v] Similarly, the single-layer, 5-layer, and 40-layer dots in figure 'c' received very long 2400 ms laser bursts at 288 mA laser current, while the dots in figure 'd' were not exposed. Again, both sets of dots were fabricated in parallel. There is negligible difference in the aspect ratios or the heights of the dots. [Exp. q-233-y]

Local electron beam-assisted nanoassembly (“nanowelding”)

As indicated by the results of the laser-assisted nanoassembly experiments, the successful build-up of high-aspect ratio multi-layer structures is likely to require some method for curing newly deposited material while the material is still vertically held place by a supporting means, such as the end of the AFM tip. To prevent force-related flattening of the deposited structure by the tip at the point of impact, a curing process that can cause a phase change at very the instant when the tip encounters the top surface of the multi-layer structure is needed. In addition, the tip needs to remain in contact with the structure during the entire hardening process to act as support scaffolding for the newly deposited material and to counteract intermolecular and surface forces. It is proposed that an electron beam emitted from the tip during impact and liftoff from the surface would allow the tip to both vertically support and instantly cure any newly deposited material. The proposed process, called “nanowelding”, is similar to a nano-scale version of welding. Work by Wilder [a] [b] has shown that a scanning probe lithography (SPL) method, wherein a beam of electrons is locally emitted from a sharp conductive tip, can be used to expose sub-30 nm patterns in electron beam sensitive resists. Her research demonstrates that SPL techniques are as effective as conventional scanning electron beam lithography (EBL) methods. Work by Griffith [c] and B. Hubert shows that the gold and silver nanoparticle inks can be cured and fixed to the substrate by EBL methods. [Figure 76].

In many ways, the proposed e-beam nanowelding method is similar to the Wilder SPL method. However, the nanowelding technique offers several significant differences: (1) dots (not lines) are being formed; (2) the material to be cured is delivered to the substrate by the tip (there is no pre-existing layer of material on the substrate); and (3) the material is a nanoparticle ink (not an ebeam-sensistive resist). Based on the electron dose required for suitable exposure as given by Wilder (SPL and EBL) and Griffith (EBL), an estimate was calculated for the dose required to cure a 250 nm diameter gold nanoparticle ink dot deposited using the nanowelding process [Table 14]. When using an e-beam resist, Wilder found that SPL requires an electron dose that is 125 times higher than conventional EBL in order to create features with the same line width and resolution. Therefore, nanowelding of nanoparticle inks should require an electron dose that is 125 times greater than Griffith EBL. The area dose for Griffith EBL is approximately $1500 \mu\text{C}/\text{cm}^2$, so the estimated dose for nanowelding is $190,000 \mu\text{C}/\text{cm}^2$. For a 100 nm wide line, the expected nanowelding dose per linear dimension is $1900 \text{ nC}/\text{cm}$. This value is more than 10 times greater and 1000 times greater than the dose required to create a 100 nm wide line in e-beam resist using SPL and conventional EBL, respectively. Because 1 pA of current provides a dose of $1 \text{ nC}/\text{cm}$ when the tip is moving at $10 \mu\text{m}/\text{s}$, and because the equivalent length of a 100 nm wide line within the area occupied by a 250 nm diameter dot is $2 \mu\text{m}$, the estimated current required to nanoweld the dot in a time of $20 \mu\text{s}$ is $19 \mu\text{A}$. The time constraint is derived from the observation that $20 \mu\text{s}$ is the typical

duration of a high intensity current spike when the tip touches down on the surface when using current source circuit 'A' [Figure 77]. The equivalent tip translation speed to cover the entire surface of the dot in a time of 20 μs is 100,000 $\mu\text{m/s}$. It turns out that 19 μA is a satisfactory estimate of the current required for nanowelding. In actual nanowelding experiments, performed with tungsten-carbide coated silicon tips and conductive gold substrates or highly-doped silicon substrates, curing currents ranged between 2 and 20 μA . Currents over 150 μA generally caused significant damage to the tip.

Five different circuit designs [Figure 77] were implemented to test the efficacy of electron beam assisted nanoassembly as a route toward the formation of high-aspect ratio multi-layer structures. The circuits differed from each other primarily by the kind of power source used to supply the tip with electrons. Two of the circuits used a current source that was capable of supplying constant current to the tip. When required, the magnitude of the current flowing from the tip to the conductive substrate was measured using a high-gain current pre-amplifier and an oscilloscope attached to the cantilever. In principle, the current source should have provided constant current flow to the tip at all times. However, in actual practice, the source was not capable of clamping down on the applied current quickly enough to compensate for the dramatic change in resistance that accompanied the tip touch-down event. In general, a 20 μs transient spike with a magnitude that was 300 to 40,000 times greater than the intended steady-state current level was observed at the very instant when the tip touched the conductive substrate. For current source settings between 1 and 10 nA, the peak magnitude of the transients ranged between 0.3 and 400 μA . After the spike, the desired steady-state current level was observed for the duration of the time that the tip was in contact with the substrate. Even when the current level was set at zero at the source, capacitive and other effects in the circuit caused the delivery of a 1 to 10 nA transient current spike upon tip touch-down.

The remaining three circuit designs utilized a constant voltage source, such as a traditional power amplifier. Because there was no clamping action required, no transient spiking effects were observed. However, due to the constantly changing resistance between the tip, the substrate, and whatever ink material may have been sandwiched in between, the voltage level needed to be set high enough to ensure sufficient current flow during the entire nanoassembly process. This overcompensation often resulted in excessive damage to the tip.

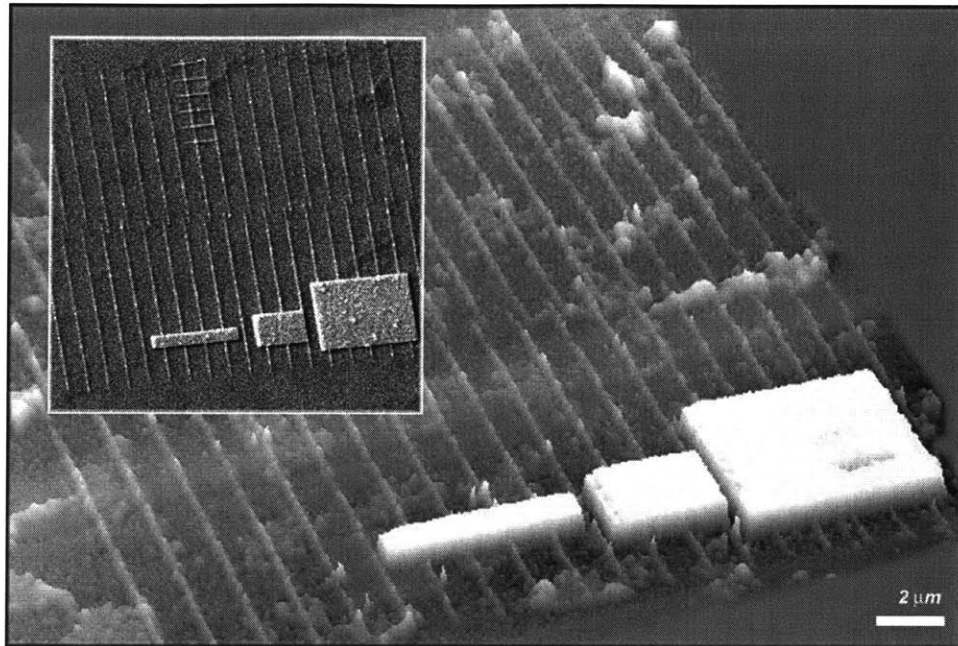


Figure 76 --- AFM and SEM (inset) images of a layer of gold nanoparticle ink patterned by conventional electron beam lithography (EBL) and then subsequently developed in an organic solvent. The three rectangular structures at lower right were 50 nm thick. The approximate beam dose was 1500 micro-coulombs per cm². The patterning was done by Griffith et. al. using a system developed by the Nano-structures Laboratory (NSL) at MIT.

Table 14 --- An estimation of the current required for electron beam "nanowelding" compared to e-beam lithography (EBL) and scanning probe lithography (SPL) methods

| lithography method | material to be exposed | area dose (μC/cm ²) | linear dose for 100 nm wide line (nC/cm) | current (μA) to cure a 250 nm dia. dot in 20 μs |
|---------------------|---|---------------------------------|--|---|
| Wilder EBL | Shipley SAL 601 e-beam resist (65 nm) | 160 | 1.6 | 0.016 |
| Griffith EBL | gold nanoparticle ink, 2.5 wt% (110 nm) | 1500 | 15 | 0.15 |
| Wilder SPL | Shipley SAL 601 e-beam resist (65 nm) | 20000 | 200 | 2 |
| NANOWELD | gold nanoparticle ink, 2.5 wt% (110 nm) | 190000 | 1900 | 19 |

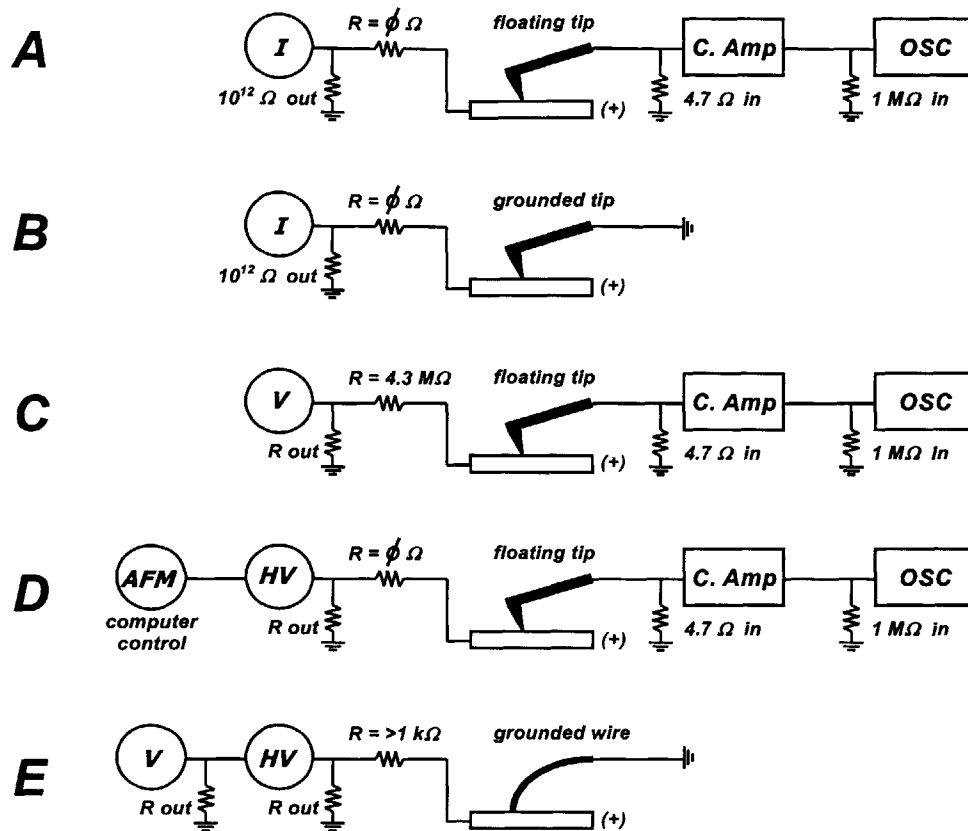


Figure 77 --- Five different circuit designs were used for electron beam assisted nanowelding procedures. Circuits 'A' through 'D' used a conductive metal-coated silicon cantilever as the tip, while circuit 'E' used the end of a 25-micron diameter tungsten wire. For all circuits, the tip was kept at a more negative potential than the current or voltage source. When required, an ultra-sensitive current pre-amplifier and oscilloscope were used to measure the current emitted from the tip to the substrate. The pre-amplifier converted the current passing through the circuit into a voltage signal that was displayed on the oscilloscope. For circuit 'D', the voltage pulse was modulated with millisecond accuracy by the script-controlled TTL-level signal coming from the AFM system internal amplifier board. All other circuits used a voltage or current source that was continuously left 'on' for the entire duration of the nanoassembly process. The tip in circuits 'A' through 'D' was translated using the piezos built into the AFM head. The metal wire in circuit 'E' was translated in a very macroscopic fashion using a manually operated probe and test station. Key: I = current source (Keithley model 225); C. Amp = current pre-amplifier (Ithaco or DL Instruments model 1211); OSC = oscilloscope (Hewlett-Packard model 54602B); V = +/- 60 volt maximum bipolar amplifier (Hewlett-Packard model 6826A); HV = high-voltage 750 volt max. amplifier (Trek model 50/750, output is 150X of the input); AFM = +/- 10 volt computer controlled signal from the amplifier unit (ECU-plus) of the Thermomicroscopes Explorer AFM system.

Three kinds of consumable materials were required for nanowelding: conductive tips, conductive substrates, and inks that undergo some physical change as a result of electron beam exposure. With a melting point of 3028 degrees Celsius, the tungsten-carbide coating on the silicon tip provided a robust conductive surface for electron emission [d]. Unfortunately, the coating also reduced the sharpness of the tip. A conductive path between the electrical circuit and the tip of the cantilever was preserved by a thin layer of conductive adhesive that was used to bond the root of the cantilever to the metal cantilever holder, and this holder was connected via a soldered wire to the circuit. Gold sputtered films on silicon wafers were initially used as the conductive substrates. However, the gold films were found to be too conductive for reliable tapping mode AFM imaging of deposited features. Electrostatic effects caused significant uncertainty about the true height and topography of nanoassembled features [Figure 79]. For example, several dots of ink deposited without e-beam assistance were imaged to have extraordinarily high, and therefore suspect, aspect ratios that exceeded 0.7. Electrostatic effects were also significant enough to prevent reliable engagement of the tip to the gold surface during attempts to execute tapping mode nanoassembly processes. As such, contact mode nanoassembly was used exclusively for all nanowelding experiments.

Even when the tip was disconnected from the electrical circuit, a few unusual results were observed. Primary among these was the observation that pick-and-place deposited dots (without e-beam assistance) were larger than those deposited onto silicon substrates [Figure 78]. These dots also exhibited reduced aspect ratios. The larger dot area may have been due to a combination of the larger radius of curvature of the coated tip (>20 nm) and the enhanced wettability of the ink on the gold surface (as indicated by the reduced contact angle of ink pools on the gold-coated substrates when compared to ink pools on plain silicon substrates). And finally, the gold surface was rather soft and easily damaged by the high transient currents sometimes emitted by the tip during the nanowelding process [Figure 80]. Subsequently, highly-doped (1-10 ohm-cm) silicon wafers, which have a higher contact resistance to the tip than the gold-coated surfaces, were used as conductive substrates, which enabled superior imaging and the fabrication of higher resolution dots.

The Griffith EBL process demonstrates that gold nanoparticle ink can be patterned and fixed to the substrate by exposure to a scanning electron beam, which indicates that some physical change in the ink is initiated by the exposure. Because the e-beam exposure is equivalent to a partial thermal cure wherein the organic capping groups are removed from the metal nanoparticles within the ink, it is assumed that the physical change is also accompanied by an increase in hardness. An increase in modulus is extremely desirable for counteracting the vertical forces delivered by the tip upon impact, and for enabling the construction of taller nano-structures with higher aspect ratios. In an initial macroscopic-scale experiment, a metal wire was connected to a constant voltage circuit.

The very tip of the wire was used to repeatedly transfer gold nanoparticle ink from a reservoir to the same location upon the conductive heavily doped silicon substrate to form a multi-layer dot, wherein every deposited layer was exposed to a curing current. The aspect ratios of the dots formed on the substrate were not particularly impressive. However, the current exposure clearly had dramatic effect on the overall height of the depositions [Figure 81]. For example, a dot that was nearly 4 microns in height (the tallest ever for any piecewise construction on a flat surface) was fabricated onto a silicon substrate. In a subsequent experiment, a conductive AFM tip and constant voltage circuit were used to deposit and weld together a multi-layer dot [Figure 82]. Sufficient constant voltage was applied by the tip to ensure that appreciable current was forced through the gold dot to the conductive substrate, no matter how many layers of ink were deposited on top of the dot. Each layer of gold ink was instantly cured as it was added to the top of the dot. Confirmation of the curing effect was provided by monitoring the current flow through the tip-dot-substrate interface, wherein the resistivity of the dot was consistently no greater than twice the resistivity of the circuit when the tip was in direct contact with bare silicon substrate (without an intervening gold dot). This "factor of two" relationship is in good agreement with the difference in resistance between fully thermally cured gold nanoparticle ink and bulk gold metal, which indicates that the nanowelding current causes nearly complete curing of the nanoparticle ink within the dot. The nanowelding curing effect was further demonstrated by passing current through 480 nm of ink material located at the bottom of a crater in the middle of a 100-layer deposition [Figure 82]. Nearby, constant current was driven through a 10-layer dot that was in excess of 800 nm thick. Although the aspect ratios of the nanowelded dots in these experiments were no greater than dots deposited without nanowelding assistance, the piece wise fabrication of structures that are instantly converted into fully conductive structures may prove useful for both vertical and planar constructions. For example, it may be useful to piece-wise build and electrically cure a conductive nano-scale wire from one electrode to another in a planar configuration.

UV/EB radiation curing describes the use of electron beam (EB), ultraviolet (UV) or visible light to polymerize a combination of monomers and oligomers. UV/EB curing is used extensively in many industries for the fabrication of laminates, inks, coatings, and adhesives. For example, considerable research is being undertaken for the development of EB-cured composites. UV or visible light curing is typically achieved using medium pressure mercury lamps, pulsed xenon lamps, or lasers. UV-curable materials contain a photoinitiator, an ingredient that generates free radicals which initiate cross-linking between the unsaturation sites of monomers, oligomers and polymers. This process is called free-radical polymerization. EB-curing is performed using an electron beam accelerator in ambient environments (no vacuum is required) to cure substantially thicker coatings, due to the greater penetration depth of the electrons. Photoinitiators are not required for EB-curing because the electrons are capable of initiating cross-linking

directly. When used in combination with the nanoassembly system, an electron-beam emitted from a conductive AFM tip may also be used to cause polymerization of a UV-curable optical adhesive (Norland #72). Indeed, multi-layer depositions of optical adhesive with a tip connected to a constant voltage circuit generated the highest aspect ratio (0.43) multi-layer structures of any nanowelding method [Figure 83]. These structures were on the order of 200 nm tall and 450 nm wide. Because the adhesive is an insulator, the observed current flow was not constant throughout the entire voltage application period. Instead, transient currents with peaks on the order of 2 micro-amps were observed at the moment that the tip touched the top surface of the dot.

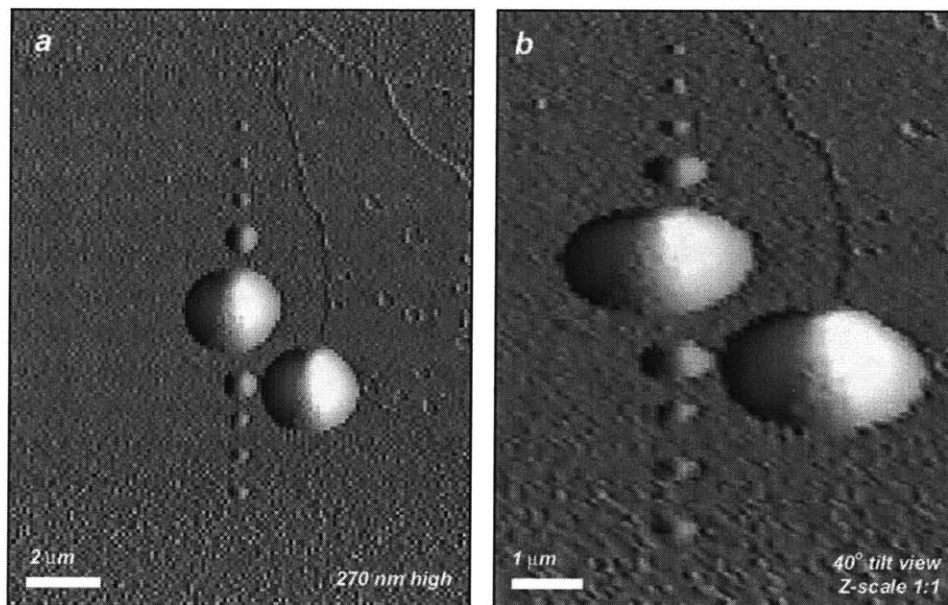


Figure 78 --- Nanoassembly of gold nanoparticle ink (3 wt% gold) onto a gold-coated silicon wafer substrate. No electron beam assistance was used. Figures 'a' and 'b' are top-down and three-dimensional off-angle views (no vertical exaggeration) of the deposited dots, respectively. Despite using a perfectly new tip, the deposited dots were very broad when compared to dots deposited onto plain un-coated silicon substrates. The larger dots are probably due to enhanced wettability of the nanoparticle ink on the gold surface. The aspect ratio of these dots was approximately 0.15. [Ex. q-237-I]

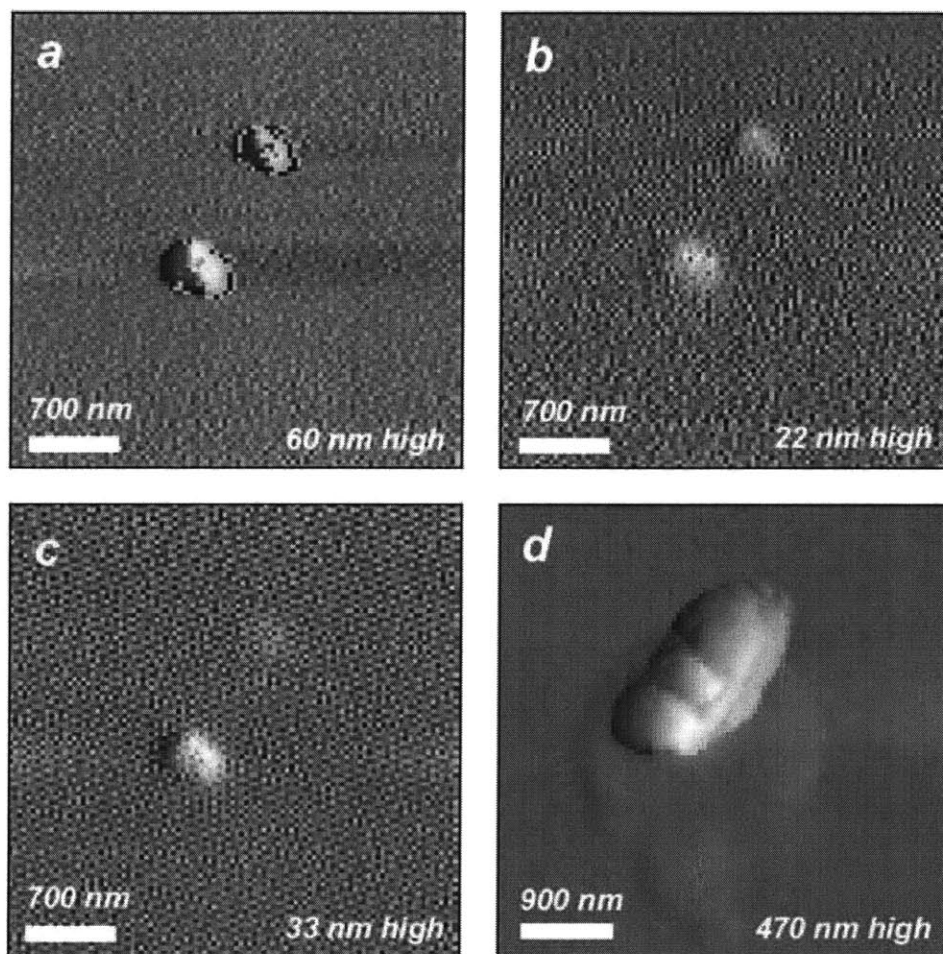


Figure 79 --- AFM tapping mode imaging of structures on a highly conductive gold substrate with a conductive tungsten-carbide coated tip yielded unreliable information about topography. The dots shown in figure 'a' were imaged when the tip was grounded and the substrate was connected to a current source with a very slight positive current flow (\sim pA). These same two dots were later imaged when the current source had a slight negative current flow, as shown in figure 'b'. In figure 'c', these same two dots were imaged when the tip and substrate were electrically disconnected from the current source and ground (floating). Although the dots were the same, the electronic environment changed the height as measured using AFM techniques. The tallest dot in figures 'a' through 'c' was imaged to have heights of 60 nm, 22 nm, 33 nm, respectively. [q-237-noisetest] Figure 'd' shows a dot formed by 80-layers of gold nanoparticle ink on a gold film substrate. No electron beam assistance was used. This dot was imaged to have a height of 500 nm with a FWHM lateral dimension (minor axis) of 700 nm, to yield an aspect ratio of 0.7. This was largest aspect ratio ever recorded, but the results of figures 'a' through 'c' call the reliability of this aspect ratio into question. [Ex. q-237-a]

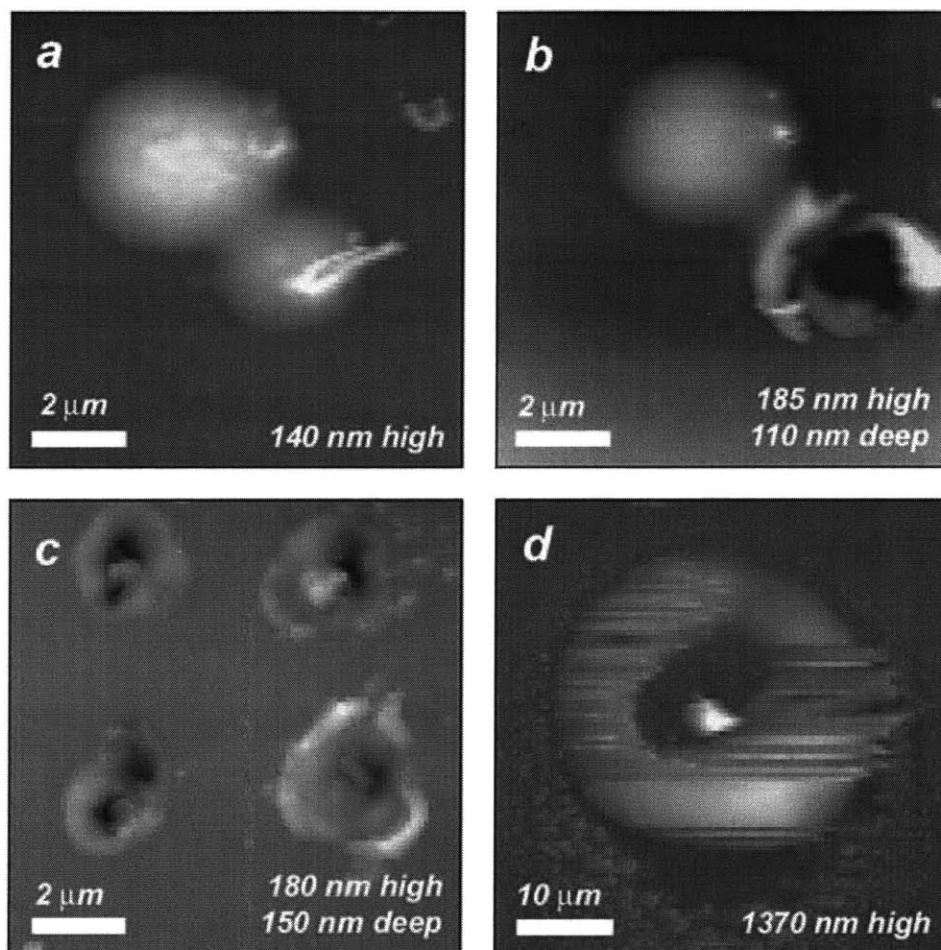


Figure 80 --- Excessively high currents and voltages applied by the tip damaged deposited structures, the tip, and even the substrate. The two 100-layer gold nanoparticle (3 wt% gold) dots shown in figure 'a' were deposited onto a gold surface using a constant current source (circuit A) that was set to constantly deliver 100 pA. However, transient spikes of 800 micro-amps were delivered each time the tip impacted the surface during the deposition step. The curing effect of the electron beam is clearly seen as a raised streak of cured ink emerging from the dot at lower right. While obtaining a second AFM image of the dots, the current source was turned back on. As shown in figure 'b', the tip just barely touched the dot at lower right during the scan, and the current flow during a transient blew the dot away leaving behind an enormous crater that penetrated 110 nm down into the gold film substrate. [Ex. q-237-c] The four craters shown in figure 'c' were created when the tip deposited gold nanoparticle ink (1 wt% gold) onto a gold film substrate using a constant current source with a setting of 100 nA. During touch-down, the current source delivered very large transient spikes of 7.5 mA for 50 microseconds. The deepest crater penetrated 150 nm into the substrate [Ex. q-238-p]

High constant voltage created the bulls-eye structure shown in the figure 'd', wherein 135 volts was continuously applied while the conductive tip was repeatedly impacted on the conductive silicon substrate. The tall object in the center was 1370 nm tall with a 0.4 aspect ratio, and is likely to be the result of blowing off and then depositing the end of the silicon tip. The low-lying ring of material was probably residual optical adhesive ink adhered to the cantilever during a previous experiment. Note that no crater was formed in the hard silicon substrate [Ex. q-236-f]

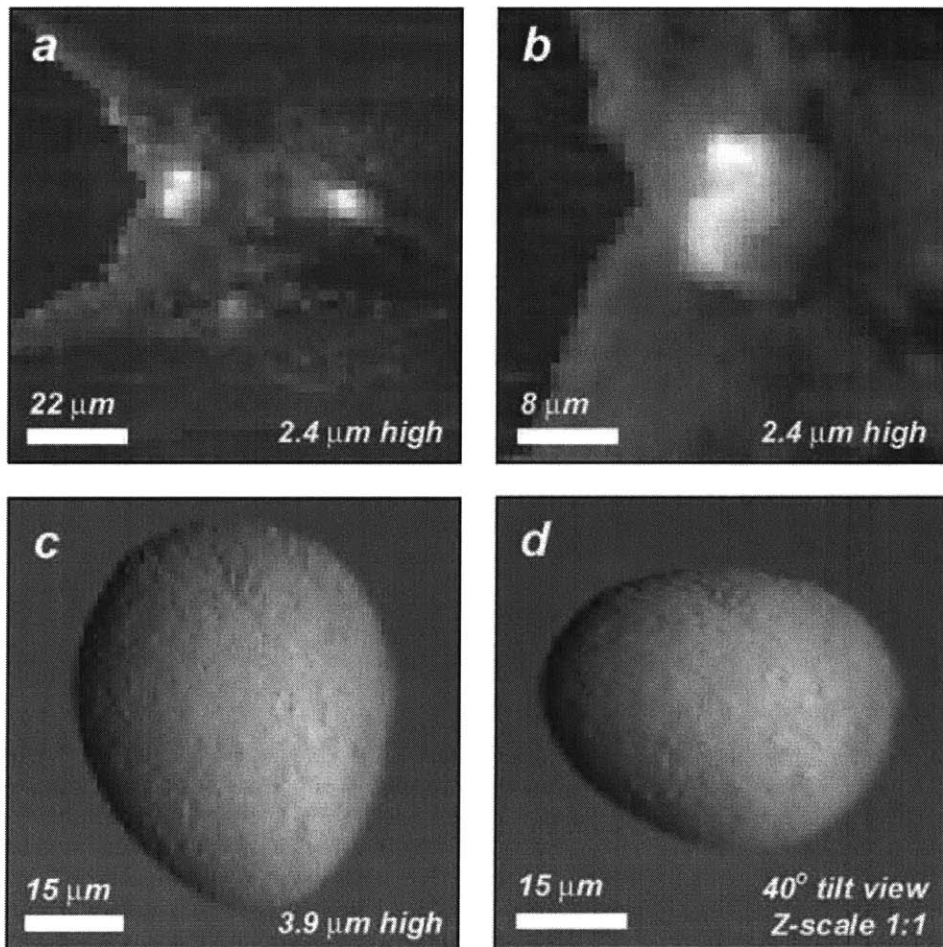


Figure 81 --- The end of a 25 micron diameter tungsten wire was manually driven by a probe station gantry system (instead of an AFM piezo system) to deposit and weld gold nanoparticle ink (1 wt% gold) onto a highly-doped conductive silicon substrate. A constant voltage-source within electrical circuit 'E' was used. Figure 'b' is a close-up view of figure 'a', wherein 95 volts were continuously applied during more than 50 pick-and-place operations. The aspect ratio of the dot in the center of the image was 0.2. [Ex. q-

239-a] Figures 'c' and 'd' are top-down and three-dimensional views (no vertical exaggeration) of a 50+ layer dot of ink (40 wt% gold) deposited with 90 to 180 volts applied during the pick-and-place operations. At 3.9 micrometers in height, this dot was the tallest structure ever fabricated onto a flat substrate. However, the aspect ratio was only 0.11. It should be noted that the structures shown in these images are likely to have had significantly smaller lateral dimensions than what is presented here because all imaging was done using the end of a blunt thermal cantilever, which used the apex of a V-shaped 5-micron diameter wire as its imaging surface. [Ex. q-239-c]

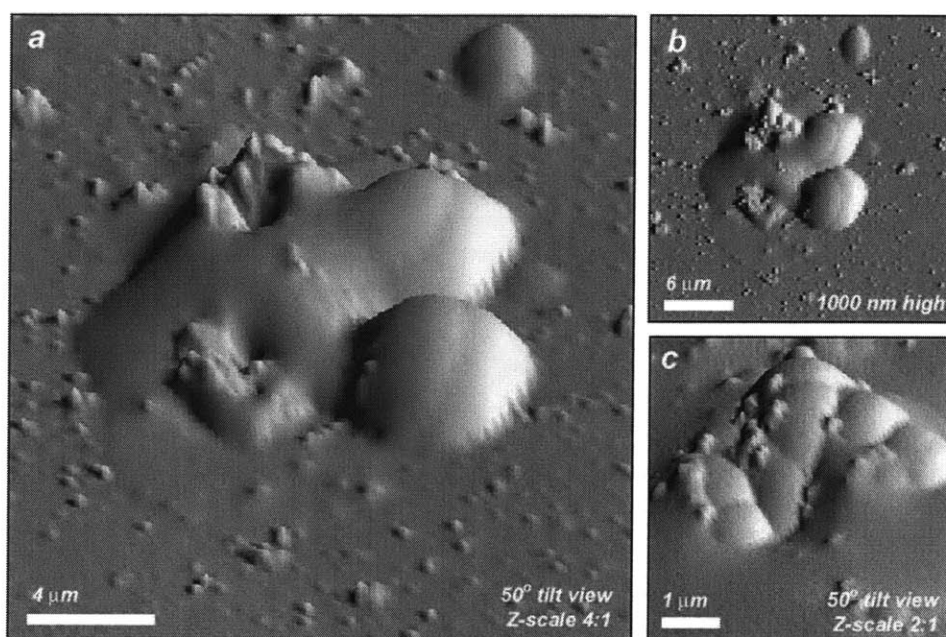


Figure 82 --- Electron-beam assisted nano-assembly of solid-phase gold nanoparticle ink (40 wt% gold) under high voltages and currents. Figure 'a' is a three-dimensional vertically exaggerated view of one 100-layer deposition (upper left) and three 10-layer depositions arranged in a square pattern on a highly-doped conductive silicon substrate (1-10 ohm-cm). The top-down view is provided in figure 'b', while a vertically exaggerated three-dimensional close-up of the 100-layer deposition is provided in figure 'c'. For each deposition step, the ink-laden tip engaged the surface and was then energized with 90 volts for 500 ms using circuit 'D'. A current pre-amplifier and oscilloscope were used verify that 500 to 1000 micro-amps of current flowed no matter how many layers of ink were deposited, which indicated that a path of cured conductive gold was formed within the multi-layer structure. This corresponded to an average circuit resistance on the order of 100 kilo-ohm, which was approximately 2 times the resistance of the circuit when the tip was in direct contact with the bare silicon surface. Further evidence of electron-beam curing is provided by the formation of a crater at the top of the 100-layer deposition. Two of the 10 layer dots (on the right) and had an

extraordinary height of 800 nm. This corresponded to 80 nm of material being deposited per layer, which was more than 10 times greater than normal. Some of this increase was probably due to the use of an ink with very high gold content [Ex. q-236-h]

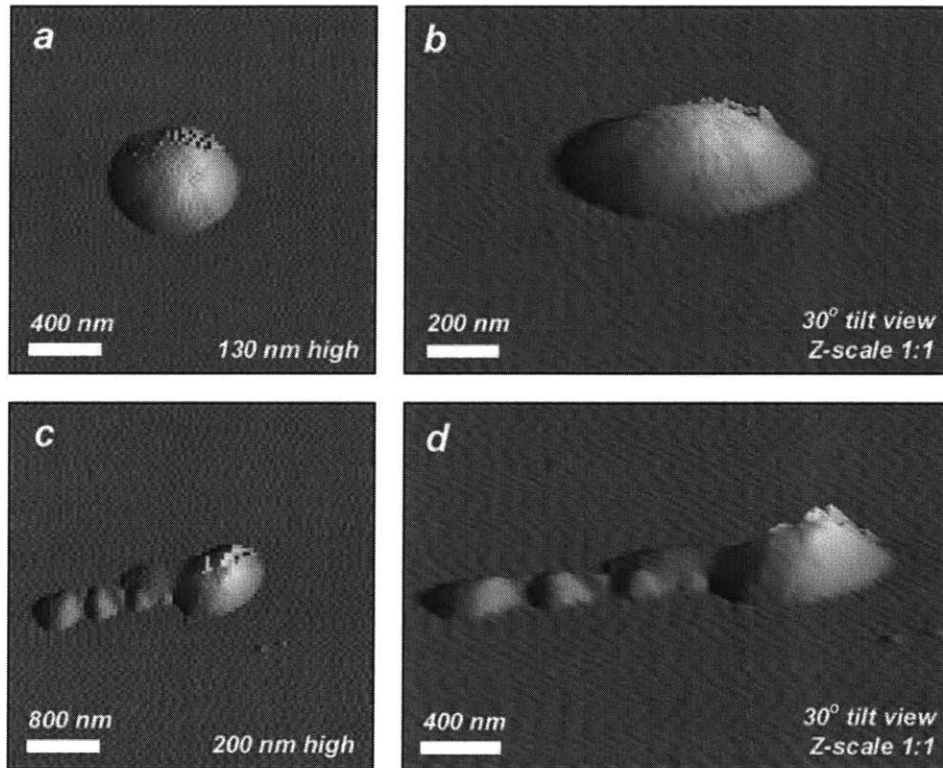


Figure 83 --- Top-down and three-dimensional views of electron beam assisted nanoassembly of UV-light curable optical adhesive (Norland #72) onto a conductive silicon substrate (1-10 ohm-cm). The three-dimensional views have no vertical exaggeration. These depositions were made using a brand new tungsten-carbide coated conductive tip, which may have helped to concentrate the effect of the emitted current through the UV-curable structure. Using a constant applied voltage of 15 volts (circuit C), the peak observed current was 3 micro-amps. The 10-layer dot shown in figures 'a' and 'b' was 130 nm tall and 380 nm wide (FWHM), with a 0.30 aspect ratio. The 100-layer dot shown in figures 'c' and 'd' was 200 nm tall and 460 nm wide (FWHM), with a 0.43 aspect ratio. The tail on 100-layer structure was due to thermal drift of the system over the duration of the construction process. [Ex. q-236-c]

Thermal source-assisted nanoassembly

A commercial thermal AFM tip [e] was used to deposit and thermally cure gold nanoparticle inks onto a silicon substrate. The thermal tip was constructed from a 5-micron diameter platinum/rhodium wire that was bent to form a "V". The apex portion of the "V" was used to pick up and place ink onto the substrate. The wire was made of a 90%/10% platinum/rhodium alloy that exhibited a 0.165% increase in electrical resistance for every degree Celsius increase in temperature. By plotting the " $\Delta R/R$ " function collected from experimental data, the temperature of the tip over a range of applied voltages was calculated. When driven above 350 mV, the thermal tip achieved temperatures above 277 Celsius, which is sufficient for thermal curing of gold nanoparticle inks [Figure 84] [Figure 85]. Various thermal curing schemes were employed in an effort to achieve superior aspect-ratio multi-layer dots: curing with the tip in direct contact with the dot; curing with the tip hovering 3 microns above the dot; and curing the ink on the tip before deposition onto the surface [Figure 86]. None of these curing methods resulted in substantially improved aspect ratios for dots deposited onto the substrate surface. However, over the course of a number of deposition experiments, a very high aspect-ratio column of gold ink material was constructed layer-by-layer directly onto the apex of the tip itself [Figure 87]. This column was 16 microns tall by 4 microns wide by 11 microns across, and had a maximum height-to-width aspect ratio of 4. The column of gold was so firmly bonded to the apex of the wire that aggressive manual manipulation with a metal probe was not capable of breaking it off. This column was a true three-dimensional micro-scale structure with an aspect ratio that was more than 8 times greater than that achieved by any previously attempted nanoassembly method.

The fabrication of the column of gold metal on the end of a thermal tip is a promising result. It is probable that a substantially smaller column of metal can be formed on the end of a sharper cantilever tip. For example, a silicon nitride thermal tip with thermistor metals deposited across the apex of the tip point might be used as a highly localized resistively heated thermal source [Figure 88]. Even smaller columns may be fabricated by using highly specialized thermal cantilevers developed at Stanford University [f]. These cantilevers have a thermal time constant of 0.8 microseconds, and can achieve a maximum temperature over 300 degrees Celsius.

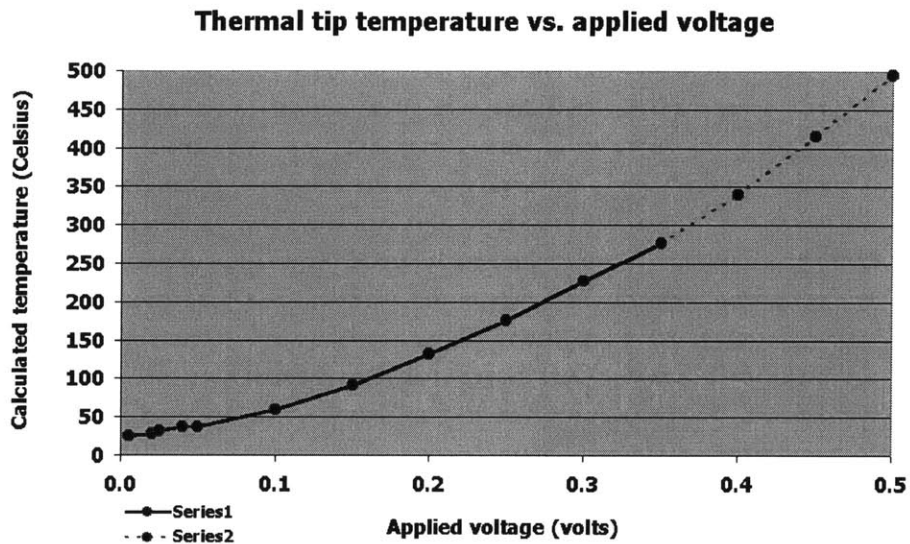


Figure 84 --- Plot of the calculated temperature of the thermal tip (Thermomicroscopes model 1615-00) as a function of voltage applied to the tip circuit. Series '1' data (blue solid line) comes from experimental data for the resistance of the wire in the tip as a function of applied voltage. Series '2' data (red dashed line) is a "by eye" projection of the voltage required to achieve temperatures higher than 277 degrees C.

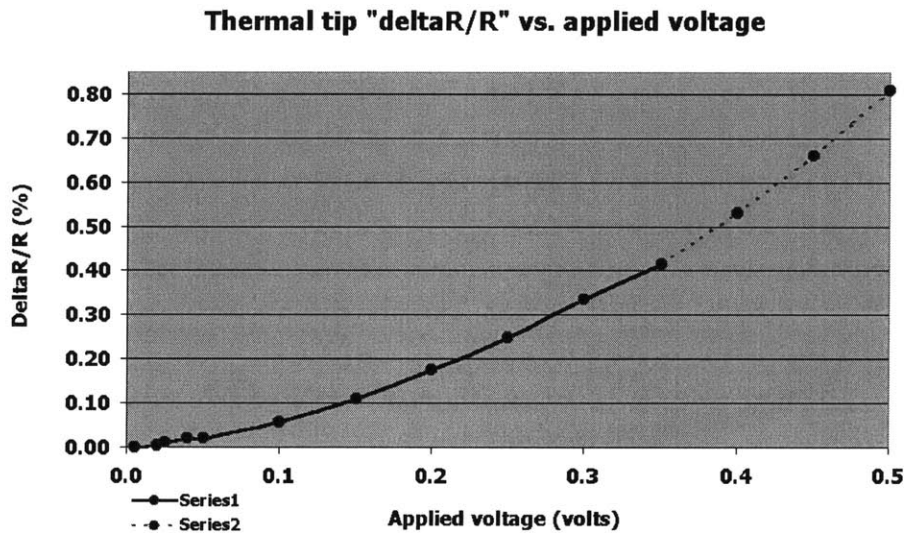


Figure 85 --- A plot of the percentage change in the resistance of the thermal tip relative to its baseline room-temperature resistance (Thermomicroscopes model 1615-00).

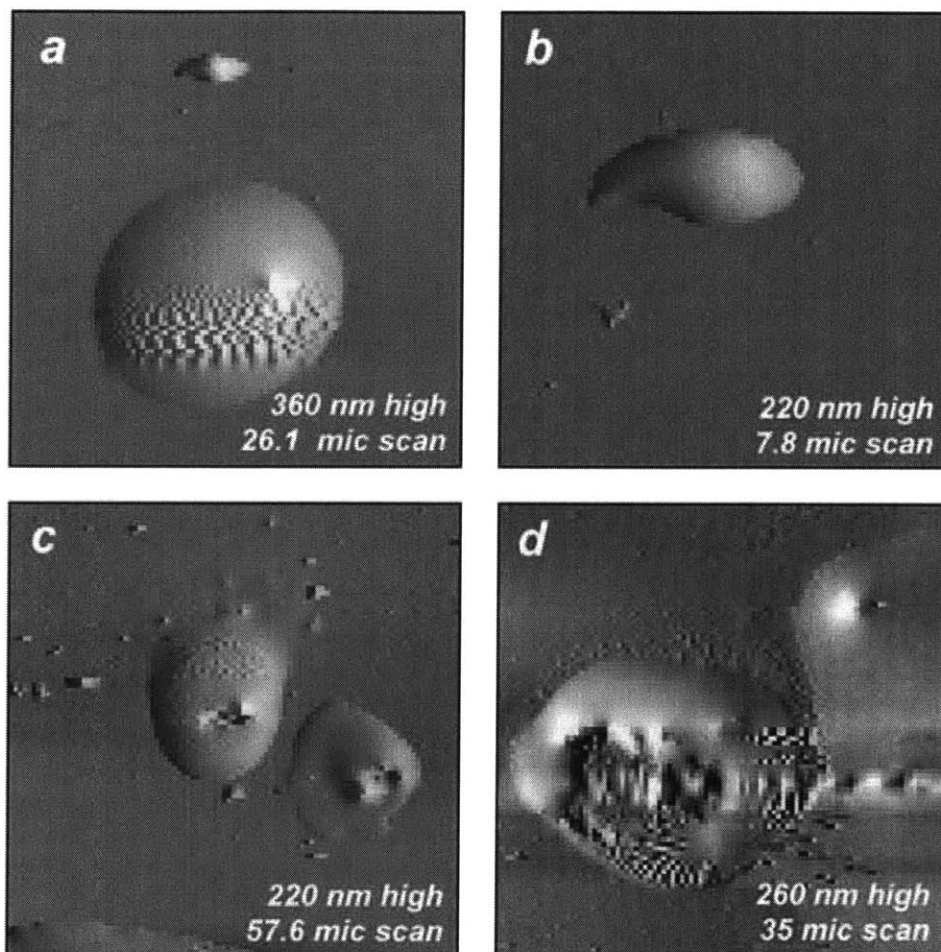


Figure 86 --- Typical multi-layer depositions of solid-phase gold nanoparticle ink (40 wt% gold) using a V-shaped thermal wire tip. The thermal wire is 5 microns in diameter, and the apex of the bend in the wire is used for picking up and depositing material. Generally, 100-layer depositions were about 10 microns across and 250 nm tall. The dots in figures 'a', 'b', and 'c' were intermittently thermally cured with the tip hovering 3 microns above the surface. Figure 'b' is a higher resolution view of the small dot at the top of figure 'a', and probably contains fewer than 10 layers. This dot had a FWHM height-to-width aspect ratio of 1:6. The 100-layer dot in figure 'd' was intermittently cured while the thermal tip was in direct contact with the surface of the dot. Heating of the tip with 500 mV for 500 ms bursts caused the tip to bend down toward the substrate while contacting the dot, which caused to formation of a crater in the middle of the dot. All dots were AFM-imaged in tapping mode with the same blunt thermal tip used for fabrication, so the actual lateral dimensions of these depositions is likely to be significantly smaller than those shown in the figures above. [Ex. q-239-i,k,l]

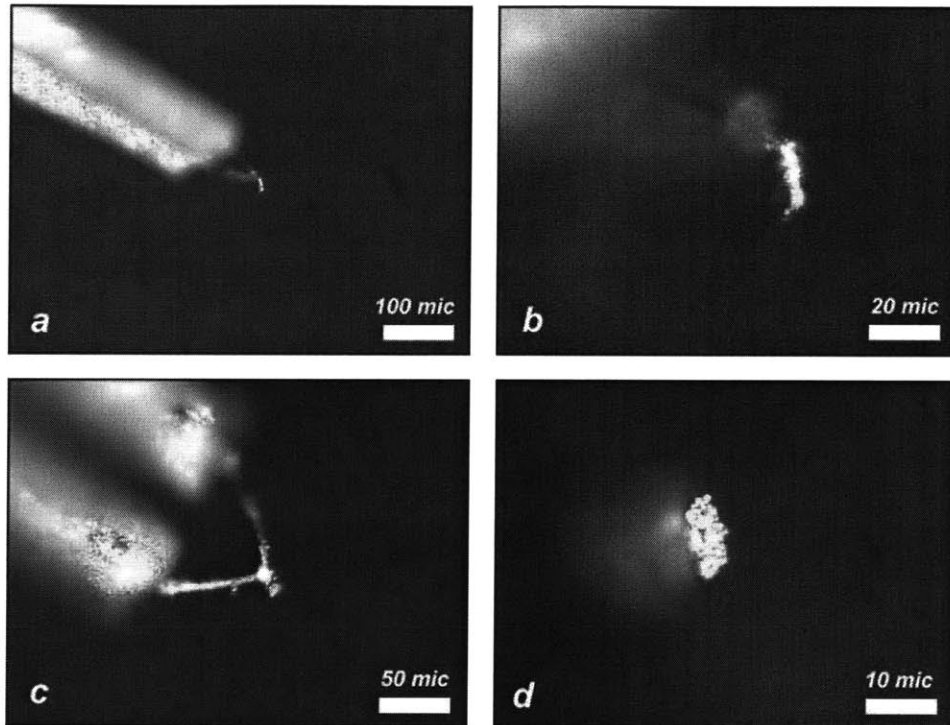


Figure 87 --- Optical microscope views of a true three-dimensional column of gold metal that was formed layer-by-layer on the end of the thermal wire tip as a result of about 1000 'pick-and-place' operations. For each deposition cycle, voltage pulses of 300-500 mV were applied for 100-500 milliseconds. The gold column was 16 microns tall, 11 microns across, and 4 microns wide. The column had a height-to-width aspect ratio of 4:1. Figures 'a' and 'b' are side views of the column, while figures 'c' and 'd' are views from the front and directly below the point of the gold column. [Ex. q-239, d-m]

Future routes to 3D nanoassembly

The most promising route toward 3D fabrication of structures onto flat substrates requires a room temperature tip and a resistively heated metal electrode bonded to a substrate. In this configuration, the tip would be used to nanoassemble ink materials onto the surface of the metal electrode. At the very moment that the ink-laden tip makes contact with the electrode, the electrode is electrically energized and is resistively heated to the curing temperature of the ink. With proper design, the thermal time constant of the electrode could be made short enough to avoid premature curing of the nearby ink reservoir. As an additional advantage, many insulating or non-polymerizing materials that would not be amenable to electron beam or UV curing can be thermally cured with ease. This would provide a substantially extended materials set for nanoassembly.

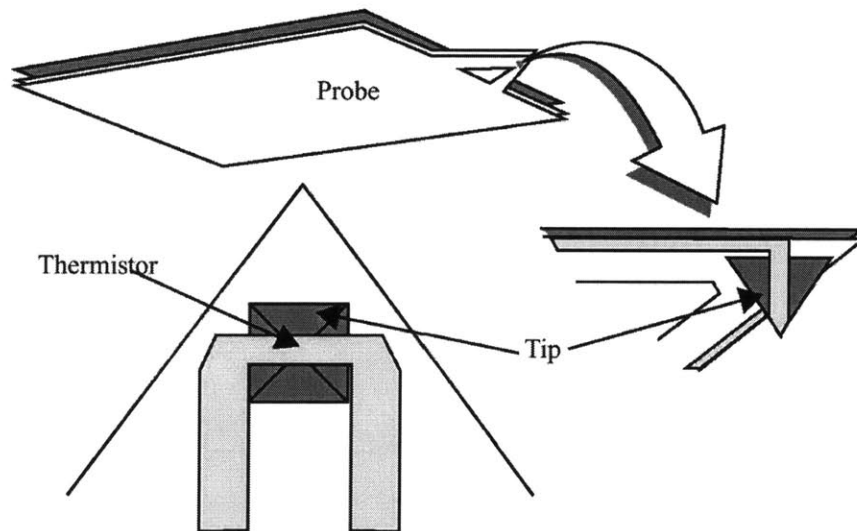


Figure 88 --- Commercially available thermal tip from Digital Instruments consisting of a modified silicon nitride probe with a thermistor deposited at the apex of the tip. This tip is designed for thermal scanning with an atomic force microscope, but could potentially be used as a resistively heated thermal source.

-
- [a] Kathryn S Wilder (Guarini), "Maskless lithography using scanning probes", August 1999, Thesis, Doctor of Philosophy, Dept. of Applied Physics, Stanford University, Advisor: Calvin F. Quate (1999).
- [b] KS Wilder, CF Quate, D Adderton, R Bernstein and V Elings, "Noncontact nanolithography using the atomic force microscope", *Appl. Phys. Lett.*, Vol, 73, No. 17, pp. 2527-2529 (1998) [\[cached\]](#)
- [c] Saul Griffith, "Towards personal fabricators: Tabletop tools for micron and sub-micron scale functional rapid prototyping", 2000, Thesis, Master of Science, Program in Media Arts and Sciences, Massachusetts Institute of Technology, Advisor: Joseph Jacobson (2000).
- [d] MicroMasch (Silicon-MDT, Moscow, Russia) tungsten-carbide conductive coatings for silicon cantilevers: An ultrathin (2 - 25 nm) film of metal is deposited on both sides of the silicon cantilever chips by a pulse plasma deposition method. The chips are then annealed to form the final tungsten-carbide
-
-

(W2C) films. The rated hardness is 18-20 GPa with a melting point of 3028 degrees Celsius. See brochure [\[cached\]](#).

- [e] Thermomicroscopes model 1615-00 thermal probes for scanning thermal microscopy: Made from a 5 micron diameter wire core of 90%/10% Pt/Rh alloy with a temperature coefficient of resistance of 0.00165 per Kelvin and a nominal resistance of 2.1 Ohm. The nominal spring constant is 5 N/m. Website: www.thermomicro.com. Tel: 408-744-3001, 800-727-5782 Address: 1171 Borregas Avenue, Sunnyvale, CA 94089. See brochure [\[cached\]](#).
- [f] Benjamin W. Chui, Jonathon Marmin, Bruce D. Terris, Dan Rugar, Kenneth e. Goodson, and Thomas W. Kenny, "Micromachined heaters with 1-microsecond thermal time constants for AFM thermomechanical data storage", Proc. of Transducers, June '97, Chicago (1997) [\[cached\]](#).

THEORY OF NANOASSEMBLY

Nanomechanical theory of material deposition

The "pick-and-place" NanoAssembly system extracts a small quantity of ink material from a reservoir and then deposits that ink material onto a substrate or on top of pre-existing nanostructures. The interactions between the tip, the ink, and the substrate are very complex, and a full mathematical model that explains the entire process with all of its variables is beyond the scope of this work. Instead, the model presented in the following sections focuses only on the deposition step of the nanoassembly operation for the specific case of the deposition of a solid-phase ink, wherein a quantity of solid ink on the apex of an ink-laden tip becomes disassociated from the tip and adheres to the substrate. The means by which the solid ink separates from the tip to become preferentially adhered to the substrate can be explained to some extent by the Hertzian and JKR models for contact adhesion between solid elastic bodies. However, these elastic models have their limitations and can only partially explain the tip-ink and ink-substrate interactions. For example, there is some evidence that indicates that the ink can behave as an inelastic body, in which case the assumption of purely elastic behavior leads to the generation of a model that is less than fully satisfactory.

Hertzian and JKR models of adhesion

The Hertz (1881) theory for contact between two elastic spheres [Figure 89] of radius ' r_1 ' and ' r_2 ' predicts that their contact radius ' a ' is related to the force ' F ' applied to the spheres and the reduced elastic modulus of contacting spheres ' K ' by

$$a = (RF / K)^{1/3}$$

$$\text{wherein } R = \frac{r_1 \cdot r_2}{r_1 + r_2} \quad \text{and} \quad K = \frac{4}{3} \left[\left(\frac{1 - \nu_1^2}{E_1} \right) + \left(\frac{1 - \nu_2^2}{E_2} \right) \right].$$

Here, ' E ' is the Young's modulus, and ' ν ' is the Poisson's ratio of the spheres. The Hertzian model does not account for any adhesion forces between the spheres at zero external applied load. The predicted contact radius at zero load is always zero. Real bodies experience attractive inter-surface forces that pull their surfaces together, giving rise to a finite contact radius even under zero load.

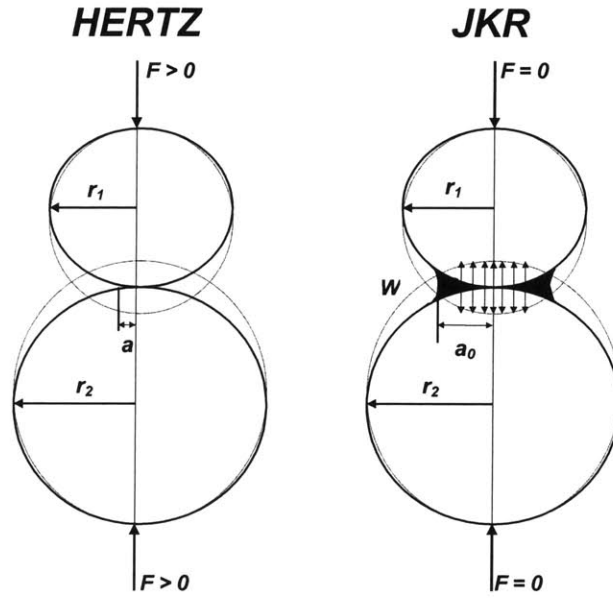


Figure 89 --- Hertz (left) and Johnson-Kendall-Roberts (right) models of adhesion for elastic solids. Even with zero external load, the JKR theory predicts a finite contact radius of 'a₀' as a result of surface energy 'W'.

Further refinements by Derjaguin, Miller, and Toporov (1975) led to the development of the DMT theory [a], which predicts the adhesion forces between the two spheres as a result of long-range attractive forces which act outside of the contact region. The JKR theory [b] by Johnson, Kendall, and Roberts (1971) accounts for the short-range attractive forces local to the region of contact, and forms the basis of many of the modern theories of adhesion mechanics [c]. The contact radius predicted by the JKR theory is always larger than the contact radius predicted by the Hertzian model [Figure 89]. The JKR theory provides for a finite contact radius between two spheres at zero applied load as well as a sudden "jump" discontinuity that arises when the spheres are pulled apart. The contact radius 'a' for any applied external load is

$$a = \left[\frac{R}{K} \left(F + 3\pi RW + \left\{ 6\pi RFW + (3\pi RW)^2 \right\}^{1/2} \right) \right]^{1/3}$$

wherein 'W' is the adhesion energy between the sphere surfaces, and generalized sphere radius 'R' is as defined previously. The contact radius 'a₀' at zero applied load is found by

$$a_0 = \left[\frac{6\pi WR^2}{K} \right]^{1/3}.$$

The spheres can be pulled apart under a negative applied load, with a connective neck of material keeping the two spheres in contact. Separation suddenly occurs when the contact radius has fallen to 63% of zero load radius 'a₀'. The source of the discontinuity is observed within the square-root term found in the equation for contact radius 'a' presented previously. The solution for the equation becomes imaginary when

$$6\pi RFW > (3\pi RW)^{1/2} \quad \text{or} \quad F > -\frac{3}{2}\pi WR .$$

Therefore, the critical adhesion or "pull-off" force 'F_s' is given by

$$F_s = -\frac{3}{2}\pi WR .$$

Adhesion model for deposition for 2D nanoassembly

The proposed model for simple single-layer (two-dimensional) material deposition using the nanoassembly system requires consideration of three primary bodies [Figure 90]. The first body is the silicon cantilever tip, which shall be modeled as a sphere with a radius 'R_T' of 20 nm. The second body is the spheroid of ink material, which shall be modeled as a sphere with a radius designated as 'R_D'. The third body is the substrate surface, which shall be modeled as a silicon sphere with a very large radius 'R_S' of 100 meters.

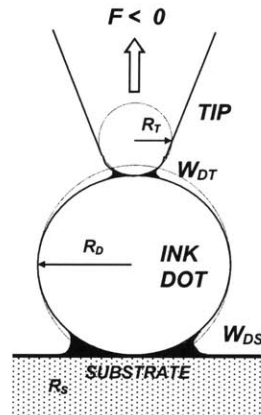


Figure 90 --- As the tip is withdrawn from the substrate, it applies negative force to the tip-ink-substrate system. The JKR model predicts the formation of connective necks at the tip-ink and the ink-substrate interfaces.

The next step is the estimation of the upper and low bounds of the radius of curvature ' R_D ' of the spheroid of ink material. A typical high-resolution dot of solid ink deposited by the nanoassembly system has a full-width-half-max (FWHM) dimension of 60 nm and a full height ' H ' of 15 nm, as measured using tapping mode AFM imaging methods. The deposited dot can be modeled as a "spheroidal cap" having a chord length ' C ' at a half-max elevation of ' $h = H/2$ ' or 7.5 nm above the substrate surface [Figure 91]. It should be noted that the deposited dot could indeed have a more fully spherical shape, but the AFM is not capable of resolving the negative angles of inclination on the underside of a sphere resting on a flat surface.

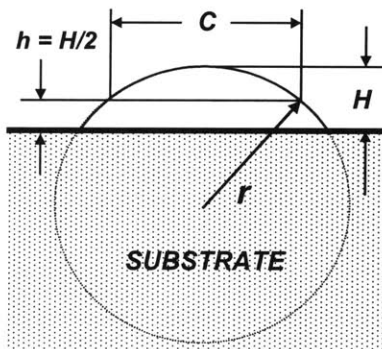


Figure 91 --- Determination of the radius ' r ' and volume of a deposited ink dot with known chord length ' C ' and full-width-half-max (FWHM) dimensions. The 3-D geometry of the dot is a "spheroidal cap".

The chord length of the spherical cap is defined by

$$C = [4h \cdot (2R_D - h)]^{1/2} ,$$

and the radius of curvature of the top surface of the deposited dot is given by

$$R_D = \frac{1}{2} \left[\frac{C^2}{4h} + h \right] = \frac{C^2}{8h} + \frac{h}{2} .$$

The upper bound on the radius of curvature is calculated to be 63.75 nm. The lower bound on the radius is found using the assumption that the entire volume ' V ' of the deposited dot is contained within a perfect sphere. The lower bound on the radius is given by

$$R_D = \left(\frac{3V}{4\pi} \right)^{1/3} \quad \text{wherein } V = \frac{H\pi}{6} \left(\frac{3C^2}{4} + H^2 \right).$$

The volume is calculated to be $2.297 \times 10^4 \text{ nm}^3$, and the lower bound on the radius is calculated to be 17.63 nm. Realistically, the ink material is likely to be an ellipsoid with a radius of curvature presented to both the tip and the substrate having a value between the upper and lower bound radii. For the arguments of this model, the ink dot before deposition is assumed to have an effective radius ' R_D ' of 30 nm. Because the tip and substrate are both composed of silicon, the adhesion energy ' W_{DT} ' between the tip and the ink dot, and the adhesion energy ' W_{DS} ' between the substrate and the ink dot are the same. Therefore the only difference in the 'pull-off' forces for both interfacial surfaces is caused by the difference in geometries intimated by the effective radius ' R ' term. With ' R_{DT} ' and ' R_{DS} ' being defined as the effective radius of the dot-tip and dot-substrate interfaces, respectively, the equations for the effective radii are given as

$$R_{DT} = R_D R_T / (R_D + R_T) \quad \text{and} \quad R_{DS} = R_D R_S / (R_D + R_S) .$$

The calculated ' R_{DT} ' is 12 nm, while the calculated ' R_{DS} ' is 30 nm. Therefore, the critical pull-off force between the dot and the substrate is greater than the pull-off force between the dot and the tip by a ratio of 30:12. Because the tip-dot "bond" is weaker, the dot is preferentially left adhered to the substrate, as shown in the following relationship.

$$F_{DS_{\text{pulloff}}} > F_{DT_{\text{pulloff}}}$$

If the adhesion energies of ' W_{DS} ' and ' W_{DT} ' are equal, and the radius of curvature presented by the ink dot to both the tip and the surface are equal, the tip will always break away from the dot of ink before the dot of ink can break away from the substrate as long as the tip has a radius of curvature that is smaller than the radius of curvature of the substrate, regardless of the size of the ink dot.

Adhesion model for deposition for 3D nanoassembly

The JKR model can also be used to explain the challenge of building three-dimensional (3D) structures, such as columns with large height:width aspect ratios, by assembling dots of ink material on top of one another. The column may have a relatively small radius of curvature at its apex, which may hinder the deposition of additional material. The model of 3D assembly [Figure 92] requires the consideration of the adhesion energy ' W_{DT} ' between the tip and the dot, the adhesion energy ' W_{DC} ' between the dot and the top

of the column, and the adhesion energy ' W_{CS} ' between the base of the column and the substrate. When ' W_{DT} ' and ' W_{DC} ' are equal, as would be the case if the column and tip are both composed of the same silicon material, the tip can no longer deposit additional ink dots on top of the column if the apex of the column achieves a radius of curvature that is smaller than the radius of curvature of the tip. In this case, the critical pull-off force ' F_{DT} ' between the tip and its burden of ink will be less than the critical pull-off force ' F_{DC} ' between the ink and the top of the column, and therefore the ink dot will preferentially adhere to the tip instead of the top of the column.

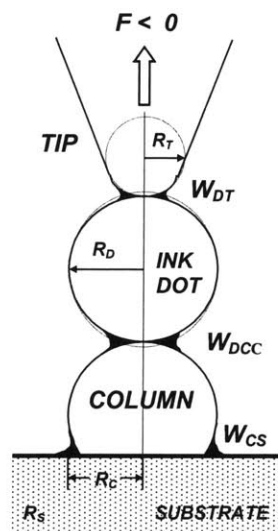


Figure 92 --- Adhesion model for 3D assembly of an ink dot onto a pre-existing column of material.

In a more realistic treatment of the model, the column is constructed from the same material as the ink dot, and the tip is coated with a layer of ink obtained from the reservoir. The deposited dot becomes disassociated from this layer of ink during the deposition process. Because the surfaces of the tip, dot, and column are all coated with the same ink material, the dot-tip and dot-column adhesion energies are essentially equivalent to the adhesion energies of an "ink-to-ink" bond. This leads to the conclusion that ' W_{DT} ' and ' W_{DC} ' are essentially equal in magnitude for an ink-coated tip and a column fabricated from ink. This effect of breaking an "ink-to-ink" bond has been demonstrated in experiments that show that multiple depositions can be carried out using a tip that has been dipped only once within the material reservoir. Gray scale patterns

have been fabricated using this "dip-once, write-many" scheme [Figure 93]. After the first deposition step, there is enough ink material remaining on the end of the tip to allow for the deposition of additional dots. This indicates that the cleave line of separation between the dot and the ink-coated tip occurs within the ink layer and not along the boundary between the ink layer and the surface of the silicon tip. Therefore, the critical pull-off force required to cause separation between the tip and the dot may be largely dictated by the adhesion energy of the ink to itself, rather than by the adhesion energy of the ink to the silicon tip.

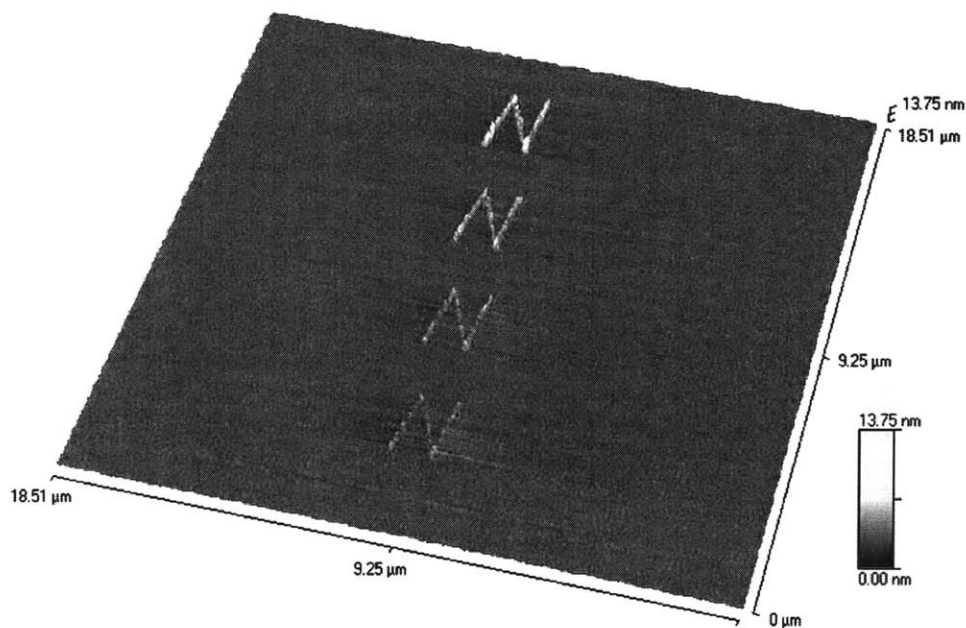


Figure 93 --- Four gray scale copies of the letter "N" have been nano-assembled in parallel. Four different line thicknesses were achieved by using a single dipping operation in the ink reservoir followed by four consecutive deposition steps, one for each "N" being constructed. [Ex. q-232-h]

Calculation of the smallest line width for a 3D column nanostructure

As discussed previously, the first dot of ink deposited by a clean silicon tip onto a clean and flat silicon substrate enjoys a favorable critical pull-off force ratio of 30:12 ($F_{DS}/F_{DT} = 2.5$). The deposited dot, which shall now be designated as the first dot at

the base of the column, has the geometry of a spheroidal cap and has a radius of curvature 'r' of 63.75 nm, as calculated before. The next dot that is deposited on top of the column (which is presently one dot thick) no longer enjoys the extremely large radius of curvature of the flat substrate. Instead, the critical pull-off force ratio is severely compromised by the very much smaller radius of curvature 'R_C' of the column. Using the same geometric assumptions as before, wherein the radius 'R_D' of the second dot of ink is 30 nm and the radius 'R_T' of the tip is 20 nm, then the critical pull-off force ratio is given by

$$\frac{F_{DC}}{F_{DT}} = \frac{-\frac{3\pi}{2} W_{DC} R_{DC}}{-\frac{3\pi}{2} W_{DT} R_{DT}}$$

$$\text{wherein } R_{DC} = \frac{R_D R_C}{R_D + R_C} \quad \text{and} \quad R_{DT} = \frac{R_D R_T}{R_T + R_C} .$$

For the reasons given earlier, it can be assumed that $W_{DC} = W_{DT}$, as both cleave lines above and below the second ink dot are within the ink material itself. With these equations, the critical pull-off force ratio for the second deposited dot is calculated to be only 15:12 ($F_{DS}/F_{DT} = 1.268$), or about half of the value for the first deposited dot. If this force ratio is maintained at 1.268 as a constant throughout the remainder of the build-up process for subsequently deposited dots, the smallest possible radius of curvature of the top of the column can be calculated. As before, 'R_D' and 'R_T' are given as 20 nm and 30 nm, respectively. The radius of curvature of the column 'R_C' is found by rearranging the previous equation to yield

$$R_C = \frac{R_D R_{DT} \left(\frac{F_{DC}}{F_{DT}} \right) \left(\frac{W_{DT}}{W_{DC}} \right)}{R_D - R_{DT} \left(\frac{F_{DC}}{F_{DT}} \right) \left(\frac{W_{DT}}{W_{DC}} \right)} .$$

Because it is assumed that $W_{DT}/W_{DC} = 1$ and $F_{DC}/F_{DT} = 1.268$, the growing column may have a radius of curvature no smaller than $R_C = 54$ nm and an overall line width of 108 nm. If the radius of curvature of the column drops below 54 nm, no additional ink material can be added to the top of the column.

Limitations of the adhesion model

In the 2D and 3D nanoassembly models presented previously, the JKR theory was invoked, but the theory is only applicable to the adhesive interactions of elastic bodies. It

should be noted that the existence of a "pull-off" cleave line within the ink layer coating the tip is a characteristic of the interaction of inelastic bodies, not elastic bodies. In addition, the permanent indentations left in the surface of a soft-solid ink reservoir by sharp point of the tip are yet another indication of inelastic behavior. A treatment of inelastic theory as applied to the nanoassembly deposition process is beyond the scope of what can be discussed here.

Resonating cantilever as real-time mass transfer detector

By monitoring the resonance frequency of the tapping mode cantilever during pick-and-place operations, real time information about the quantity of ink that is adhered to the tip can be obtained. It is anticipated that such a frequency monitoring technique may be useful for determining how much ink has been acquired by the tip during the most recent dip into the ink reservoir, and for determining how much and at what rate ink material is being deposited onto the substrate. The feasibility of this notion can be predicted with the formulae for cantilever mechanics. First, continuous beam and lumped parameter models are invoked to provide an estimate of the undamped natural frequency of the cantilever and tip. Then the minimum detectable shift in frequency is determined by the calculation of the quality factor of the cantilever in an air-damped condition. Finally, the minimum detectable mass of ink

Continuous beam model

Derived from conventional continuous beam theory [d], the natural resonant frequency for the first mode of vibration for a simple cantilever beam in an undamped condition is

$$f = \frac{3.52}{2\pi} \sqrt{\frac{EI}{L^4 A \rho}} = \frac{3.52}{4\pi} \frac{t}{L^2} \sqrt{\frac{E}{3\rho}} = 0.162 \cdot \frac{t}{L^2} \sqrt{\frac{E}{\rho}} .$$

In this equation, 'E' is the Young's modulus and 'ρ' is the bulk density of the cantilever material. The quantity represented by 'I' is the moment of inertia, which contains elements of cantilever geometry including length 'L', thickness 't', and width 'w'. It should be noted that the frequency is independent of beam width 'w', which appears in both the numerator and denominator of the frequency equation as a component of 'I' and 'A', respectively. Generally, commercial silicon cantilevers are constructed so that the

Young's modulus of the <110> silicon orientation applies. The material and geometric values for a typical commercial scanning probe [e] useful for this model are

E <110> orientation = 169GPa

$\rho = 2330 \text{ kg/m}^3$

t = 4 μm

L = 125 μm

w = 35 μm

The estimate of the cantilever natural frequency using the continuous beam theory is

$$f = 353.2 \text{ kHz} .$$

The continuous beam theory equation used here assumes low amplitude oscillations (as large amplitudes cause the effective spring constant to change) and an undamped condition. The actual nanoassembly experiments were performed in air in the presence of fluid damping. The effect of this damping is clearly visible in a plot of the cantilever frequency response [Figure 94], wherein the observed amplitude at the damped peak frequency is only a few times greater than the amplitude at the off-resonance frequencies. If desired, the value of the fluid damping coefficient can be determined by an experiment in which the end of the cantilever is deflected by a secondary probe and released. The observed resonant decay would provide information about the damping characteristics of the cantilever in air.

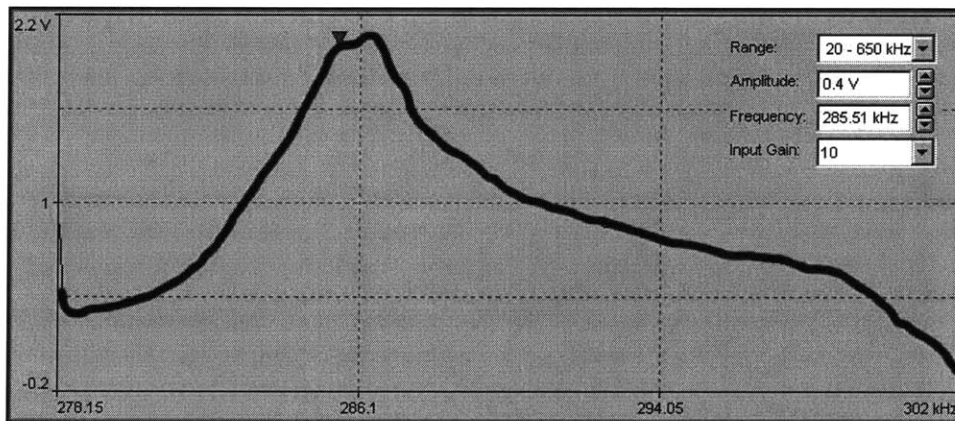


Figure 94 --- Frequency response of a silicon cantilever (tungsten-carbide coated). Peak frequency = 285.4 kHz; peak amplitude = 1.945 Volts. MicroMasch (Silicon-MDT) model NSC15; 325 kHz; 40 N/m force constant. Dimensions: 4 x 35 x 125 microns.

The continuous beam equation used previously also neglected the mass contribution at the end of the cantilever by the conical or pyramidal tip, which is often 5 to 15 microns tall. The mass contribution of the tip although generally small, can have a noticeable effect on the resonant frequency, particularly for very pliable tips. The cantilever frequency 'f' of the cantilever and pyramidal tip is

$$f = \frac{\sqrt{3}}{2\pi} \sqrt{\frac{E \cdot w \cdot t^3}{12 \left[(R \cdot L^3) + (0.236 \cdot V \cdot L^4) \right]}}$$

wherein 'R' is the mass of the tip (which is assumed to be concentrated at the very end of the cantilever) and 'V' is the cantilever mass per unit length ($V = \rho \cdot w \cdot t$). If the tip is assumed to have a conical shape (instead of a pyramidal shape), with its height and base dimensions being defined by variable 'H', the frequency of the cantilever and tip is found to be

$$f = 0.276 \sqrt{\frac{E \cdot w \cdot t^3}{\rho \left[(\pi \cdot H^3 \cdot L^3) + (2.832 \cdot w \cdot t \cdot L^4) \right]}}$$

For the cantilever values used previously, but now adding a conical tip that is 15 microns tall and 15 microns at its base, the new calculated resonant frequency is

$$f = 324.6 \text{ kHz}$$

Lumped parameter model

The equations for the resonating cantilever can also be derived more intuitively by recasting the continuous beam form into a lumped parameter model, wherein the system can be described by an effective mass and an effective spring constant which are relevant over moderate displacements. Effective mass ' M_{eff} ' is determined using the geometry and density of the cantilever, and can be expressed as

$$M_{\text{eff}} = \frac{3}{8} \rho \cdot w \cdot t \cdot L$$

The effective spring constant ' K_{eff} ' is determined by the geometry and modulus of the cantilever, and is expressed as

$$K_{\text{eff}} = \frac{3EI}{L^3} \quad \text{wherein} \quad I = \frac{wt^3}{12} .$$

Here, I is the moment of inertia. It is clear that the effective spring constant is extremely sensitive to the accuracy of the beam thickness measurement, as the effective spring constant is proportional to the beam thickness cubed. Using the standard "square-root-of-k-over-m" argument, the cantilever frequency is found by

$$f = \frac{1}{2\pi} \sqrt{\frac{K_{\text{eff}}}{M_{\text{eff}}}} .$$

Using the previously given commercial cantilever values, the frequency ' f ', effective spring constant ' K_{eff} ', and effective mass ' M_{eff} ' are calculated to be:

$$f = 283.3 \text{ kHz}$$

$$K_{\text{eff}} = 48.46 \text{ N/m}$$

$$M_{\text{eff}} = 6.11 \times 10^{-11} \text{ kg}$$

Comparison

The commercial scanning probe cantilever used as an example in the previous modeling equations is the NSC15 series single non-contact cantilever from MikroMasch [e] [Figure 94]. The manufacturer states that the typical resonant frequency is 325 kHz (with a range of 265 - 400 kHz) and that the typical spring constant is 40 N/m (with a range of 20 to 75 N/m). Despite their limitations, both the continuous beam model and lumped parameter model have provided reasonable estimates of the resonant frequency of the cantilever.

Frequency shift detection sensitivity

The resonant frequency of the cantilever shifts as the tip acquires and deposits ink material. The mass of the adhered material can be measured by detecting the shift in resonant frequency. For the slope detection method [f], in which amplitude and phase changes are monitored at a fixed frequency, the minimum detectable frequency change Δf_{min} is approximately defined by

$$\Delta f_{\min} = \frac{2\pi f}{Q} .$$

The resonance peak for a typical scanning probe cantilever in air is somewhat rounded at its top [Figure 94]. The roundness of the resonance peak limits the sensitivity of a mass monitoring technique. This loss of quality factor, or 'Q', is largely due to fluid damping from the air and other effects. The quality factor is defined by

$$Q = \frac{M_{\text{eff}} \cdot 2\pi f}{b}$$

wherein the effective mass 'M_{eff}' and frequency 'f' are as previously calculated. The fluid damping coefficient 'b' can be calculated using Griffin's squeeze-film damping equation [g][h]

$$b = \frac{96 \cdot U \cdot L \cdot w^3}{g^3 \cdot \pi^4} ,$$

which is a classic small-motion linearization of the governing Reynolds equation. Here, 'U' is the fluid viscosity (1.86 x 10⁻⁵ Ns/m² or kg/ms for air at room temperature) and 'g' is the gap distance between the underside of the cantilever and the substrate. If the height of the conical tip at the end of the cantilever is assumed to be 15 microns, the gap can be no smaller than 15 microns when the end of the tip is in direct contact with the substrate. In most circumstances, the frequency measurement procedure for ink mass detection is likely to be conducted when the tip is retracted about 5 microns from the surface, which provides a squeeze-film gap of 20 microns. The squeeze-film damping coefficient 'b' is calculated to be

$$b = 9.22 \times 10^{-9} \text{ kg/s} .$$

Using the calculated values for 'f', 'M_{eff}', and 'b', the quality factor is found to be

$$Q = 11,796$$

and the minimum detectable frequency change is found to be

$$\Delta f_{\min} = 173.4 \text{ Hz} .$$

This is equivalent to a frequency shift sensitivity of 0.53%. This value corresponds very well with experimental data, wherein the rounded nature of the resonance peak prevented reliable detection of frequency shifts below 100 Hz.

Now that the quality factor and damping coefficient have been determined, additional aspects of the cantilever dynamics can be calculated including the time constant of resonance decay and the amplitude of vibration under both damped and undamped conditions. The amplitude of cantilever resonance amplitude will decay as $e^{-t/T}$, where the time constant is $T = 2Q/2\pi f$. For the example cantilever, the resonance amplitude is expected to decay with a time constant of $2Q/2\pi f$ or 5.7 milliseconds. The amplitude drops to $1/\sqrt{e} = 60.56\%$ of its original magnitude at every time $t = Q/2\pi f$. The amplitude of resonance 'A' (as measured in units of length) caused by an excitation force 'F' can be calculated by $A = (Q \cdot F)/K_{\text{eff}}$. For most scanning probe operations, the forces on the cantilever are in the pico-Newton to nano-Newton range. Therefore, the expected range of amplitudes is 0.2 to 200 nanometers. And finally, the ratio of the damped amplitude to the undamped amplitude (A_{damp}/A) of 22% was calculated using the following equation:

$$\frac{A_{\text{damp}}}{A} = \frac{K_{\text{eff}}}{2\pi f \cdot Q}$$

Mass measurement sensitivity

Recall now the continuous beam model for the cantilever and extra contribution from a conical tip of mass 'R' positioned at the very end of the cantilever. In the following equation, the resulting frequency is designated as 'f₁':

$$f_1 = \frac{\sqrt{3}}{2\pi} \sqrt{\frac{E \cdot w \cdot t^3}{12 \left[(R \cdot L^3) + (0.236 \cdot V \cdot L^4) \right]}}$$

Mass per unit length of the cantilever is $V = \rho \cdot w \cdot t$, and the conical tip with identical height and base length 'H' has a mass $R = \rho \cdot \pi \cdot H^3/12$. When the tip is dipped into a reservoir of material, an extra amount of mass 'r' becomes concentrated right on the apex of the tip, and can therefore be treated as a simple increase to the mass the of the tip without significantly affecting geometry. At this point the cantilever would have a modified frequency, designated here as 'f₂'. The "before" and "after" equations of frequency are as follows:

$$f_1 = \frac{\sqrt{3}}{2\pi} \sqrt{\frac{E \cdot w \cdot t^3}{12 \left[(R \cdot L^3) + (0.236 \cdot V \cdot L^4) \right]}} \quad (\text{before dipping})$$

$$f_2 = \frac{\sqrt{3}}{2\pi} \sqrt{\frac{E \cdot w \cdot t^3}{12 \left[((R+r) \cdot L^3) + (0.236 \cdot V \cdot L^4) \right]}} \quad (\text{after dipping})$$

Setting the $E \cdot w \cdot t^3$ terms in both equations equal to each other, and canceling identical terms, allows the two equations to be combined, as shown below:

$$\frac{(f_1)^2}{(f_2)^2} = \frac{(R+r) \cdot L^3 + (0.236 \cdot V \cdot L^4)}{R L^3 + (0.236 \cdot V \cdot L^4)}$$

Rearranging again and solving for the additional mass 'r' gives

$$r = \left(\frac{1}{L^3} \left(\frac{(f_1)^2}{(f_2)^2} (R L^3 + 0.236 V L^4) \right) - 0.236 V L^4 \right) - R$$

wherein

$$f_2 = f_1 + \Delta f$$

Here, Δf is the minimum detectable change in frequency, which was previously calculated to be 173.4 Hertz for the sample cantilever. In the final equation below, substitutions are made for the mass of the conical tip and the mass per unit length of the cantilever to provide an expression for the minimum detectable ink mass 'r':

$$r = \left(\frac{1}{L^3} \left(\frac{(f_1)^2}{(f_1 - \Delta f)^2} \left(\left(\frac{\pi \rho H^3}{12} \right) L^3 + 0.236 \rho w t L^4 \right) \right) - 0.236 \rho w t L^4 \right) - \left(\frac{\pi \rho H^3}{12} \right)$$

For the sample cantilever, the minimum detectable mass is:

$$r = 1.255 \times 10^{-14} \text{ kg} = 12.55 \text{ picograms}$$

A more intuitive solution for the minimum detectable mass can be derived from the lumped parameter model equations. The comparable "before" and "after" dipping equations are:

$$K_{\text{eff}} = (2\pi f_1)^2 (M_{\text{eff}})^2$$

$$K_{\text{eff}} = (2\pi f_2)^2 (M_{\text{eff}} + r)^2$$

These two equations can be combined by canceling out the ' K_{eff} ' terms. Rearranging and solving for ' r ' yields

$$r = M_{\text{eff}} \left(\frac{(f_1)^2}{(f_1 - \Delta f)^2} - 1 \right).$$

According to this equation, which is derived from the lumped parameter model, the minimum detectable mass is

$$r = 6.530 \times 10^{-14} \text{ kg} = 65.30 \text{ picograms} .$$

The scale of a picogram

As shown previously, the minimum detectable mass is on the order of 10 picograms. The following calculations will reveal the size of a deposited hemispherical dot with a mass of 10 picograms consisting of gold atoms. Each gold atom weighs 3.3×10^{-22} grams, has an atomic radius of 0.1441 nm, and has an atomic volume of 0.0125 cubic nanometers. Therefore, a 10 picogram dot contains 3.03×10^{10} gold atoms. Using an assumption of a 60% fill factor for the packing of atom-sized spheres within the deposited dot, the effective volume per gold atom is 0.0208 cubic nanometers. If the 10 picogram dot is deposited as a perfect hemisphere on the surface of the substrate, the dot will have an equatorial diameter of 1.3 micrometers. The full-width-half-max (FWHM) dimension of this deposited dot is approximately 900 nm. For comparison, the smallest dot of material deposited by the NanoAssembly system had a FWHM dimension below 30 nm.

Routes to increasing mass measurement sensitivity

Clearly, there is a need to increase the mass measuring resolution of the proposed system. The quality factor ' Q ' can be increased by reducing the fluid damping in the system, as can be accomplished by placing the resonating cantilever within a vacuum environment. However, this option is highly non-ideal because many of the nanoassembly processes

require a liquid ink reservoir that would immediately evaporate when placed within a vacuum environment. Recently, scanning probe researchers have shown that the use of a positive feedback system can increase the effective 'Q' by 2 orders of magnitude from 1 to several hundreds within a liquid environment [f]. A phase-locked loop arrangement is used to track cantilever frequency, while a positive feedback loop provides phase-locked gain to the drive signal of the cantilever. The end result is a system with a dramatically improved quality factor. The effective damping coefficient can be driven to near zero (or even negative, which can create an unstable system), as shown in the following equation

$$b_{\text{eff}} = b - \frac{G}{2\pi \cdot f} ,$$

wherein 'G' is the gain input of the positive feedback loop. Naturally, by making 'b_{eff}' very small, the quality factor can be increased dramatically. It is envisioned that a positive feedback system can also improve the effective 'Q' of the cantilever used in the NanoAssembly system when operating in a gaseous environment, thereby improving the detection of the shift in frequency.

If the quality factor can be increased by 100 fold, the minimum detectable frequency shift would decrease by 100 fold to about 1.7 Hertz. This provides a 100-fold decrease in the minimum detectable mass to 0.12 picograms, which yields a deposited dot with a hemispherical diameter of 300 nm and a FWHM of about 220 nm. These dot dimensions are comparable to the 200 nm average sized dot deposited by the NanoAssembly system when using a dull tip.

-
- [a] BV Derjaguin, VM Muller and YP Toporov, *Journal of Colloid Interface Science*, Vol. 53, pp. 314-320 (1975).
- [b] KL Johnson, K Kendall and AD Roberts, "Surface energy and the contact of elastic solids", *Proceedings of the Royal Society A*, Vol. 324, pp. 301-313 (1971).
- [c] Jacob Israelachvili, "Intermolecular and surface forces", second edition 1998, Academic Press, London, pp. 326-334 (1992).
- [d] Formulas derived from "Roark's Formulas for Stress and Strain", 6th edition, Warren C. Young, McGraw Hill.
-
-

-
- [e] For this example, the typical commercial scanning probe is illustrated by the following: MicroMasch (Silicon-MDT, Moscow, Russia) unmounted high resonance frequency tapping mode silicon cantilever: model NSC15; 325 kHz; 40 N/m force constant. Dimensions: 4 microns thick by 35 microns wide. Cantilever length: 125 microns. Websites: www.spmtips.com, www.micromasch.com, www.siliconmdt.com. Distributed in the USA by K-TEK International, 7086 S.W. Beveland Street, Portland, Oregon 97223. Website: www.ktekintl.com. Tel: (503) 624-0315. See brochure [\[cached\]](#).
- [f] ADL Humphris, J Tamayo and M.J Miles, "Active quality factor control in liquids for force spectroscopy", *Langmuir*, Vol. 16, No. 21, pp. 7891-7894 (2000). [\[cached\]](#)
- [g] WS Griffin, HH Richardson and S Yamanami, "A study of fluid squeeze-film damping," *J. Basic Eng.*, Trans. ASME, pp. 451-456, June 1966. pages pp. 451456 (1966).
- [h] An excellent treatment of squeeze-film damping as applied to MEMS structures is provided by the following reference: Yao-Joe Yang (Joseph Y.-J. Young), "Squeeze-film damping for MEMS structures", Thesis, Master of Science, Dept. of Electrical Eng., Massachusetts Inst. of Tech., Advisor: SD Senturia (January 1998). [\[cached\]](#)

REFERENCES

Cited references by chapter (in order of citation)

Introduction

"International Technology Roadmap for Semiconductors (ITRS)", 1999 Edition and 2000 update; available on the web at <http://public.itrs.net/Reports.htm> .

HC Manoharan, CP Lutz and DM Eigler, "Quantum mirages formed by coherent projection of electronic structure", Nature, Vol. 403, No. 6769, 512-515 (2000).

R Resch, N Montoya, BE Koel, A Madhukar, AAG Requicha and P Will, "Manipulation of nanoparticles in liquids using MAC mode Atomic Force Microscopy", Molecular Imaging Application Note, April 1999 (1999).

MR Falvo, RM Taylor II, A Helser, V Chi, FP Brooks Jr, S Washburn and R Superfine, "Nanometre-scale rolling and sliding of carbon nanotubes", Nature, Vol. 397, No. 6716, 236-238 (1999).

S Hong, J Zhu, and CA Mirkin, "Multiple ink nanolithography: Toward a multiple-pen nano-plotter", Science, Vol. 286, Oct 15, 523-525 (1999). [[cached](#)]

S Hong and CA Mirkin, "A nanoplotted with both parallel and serial writing capabilities", Science, Vol. 288, June 9, 523-525 (2000). [[cached](#)]

3D NanoAssembly

Kathryn S Wilder (Guarini), "Maskless lithography using scanning probes", August 1999, Thesis, Doctor of Philosophy, Dept. of Applied Physics, Stanford University, Advisor: Calvin F. Quate (1999).

KS Wilder, CF Quate, D Adderton, R Bernstein and V Elings, "Noncontact nanolithography using the atomic force microscope", Appl. Phys. Lett., Vol, 73, No. 17, pp. 2527-2529 (1998). [[cached](#)]

Saul Griffith, "Towards personal fabricators: Tabletop tools for micron and sub-micron scale functional rapid prototyping", 2000, Thesis, Master of Science,

Program in Media Arts and Sciences, Massachusetts Institute of Technology,
Advisor: Joseph Jacobson (2000).

Benjamin W. Chui, Jonathon Marmin, Bruce D. Terris, Dan Rugar, Kenneth e. Goodson, and Thomas W. Kenny, "Micromachined heaters with 1-microsecond thermal time constants for AFM thermomechanical data storage", Proc. of Transducers, June '97, Chicago (1997) [[cached](#)].

Theory of NanoAssembly

BV Derjaguin, VM Muller and YP Toporov, Journal of Colloid Interface Science, Vol. 53, pp. 314-320 (1975).

KL Johnson, K Kendall and AD Roberts, "Surface energy and the contact of elastic solids", Proceedings of the Royal Society A, Vol. 324, pp. 301-313 (1971).

Jacob Israelachvili, "Intermolecular and surface forces", second edition 1998, Academic Press, London, pp. 326-334 (1992).

"Roark's Formulas for Stress and Strain", 6th edition, Warren C. Young, McGraw Hill.

ADL Humphris, J Tamayo and M.J Miles, "Active quality factor control in liquids for force spectroscopy", Langmuir, Vol. 16, No. 21, pp. 7891-7894 (2000). [[cached](#)]

WS Griffin, HH Richardson and S Yamanami, "A study of fluid squeeze-film damping," J. Basic Eng., Trans. ASME, pp. 451-456, June 1966. pages pp. 451-456 (1966).

Yao-Joe Yang (Joseph Y.-J. Young), "Squeeze-film damping for MEMS structures", Thesis, Master of Science, Dept. of Electrical Eng., Massachusetts Inst. of Tech., Advisor: SD Senturia (January 1998). [[cached](#)]

Un-cited references

T Tanikawa, Y Hashimoto, and T Arai, "Micro drops for adhesive bonding of micro assemblies and making a 3-D structure 'micro scarecrow'", IEEE/RSJ Proc., Int'l

Conf. on Intelligent Robots and Systems, 13-17 Oct. 1998, vol. 2, pp. 776-781
(1998) [\[cached\]](#)

S Saito, H Miyazaki, and T Sato, "Pick and place operation of a micro-object with high reliability and precision based on micro-physics under SEM", Int'l Conf. on Robotics and Automation, 10-15 May 1999, IEEE Proceedings, Vol. 4, pp. 2736-2743 (1999).
[\[cached\]](#)

T Kasaya, H Miyazaki, S Saito and T Sato, T, "Micro object handling under SEM by vision-based automatic control", Int'l Conf. on Robotics and Automation, 10-15 May 1999, IEEE Proceedings, Vol. 3, pp. 2189-2196 (1999). [\[cached\]](#)

H Miyazaki, and T Sato, "Pick and place shape forming of three-dimensional micro structures from fine particles", IEEE, Proc. of the Int'l Conf. on Robotics and Automation, 22-28 April, Vol. 3, pp. 2535-2540 (1996). [\[cached\]](#)

Masayuki Nakao, Yotaro Hatamura and Tomomasa Sato, "Tabletop factory to fabricate 3D microstructures: Nano Manufacturing World", Proc. ASPE 1996 Annual Meeting, Monterey, California, pp. 58-65, 74-79 (English) (1996).

Masayuki Nakao, et al.; "Tabletop factory to fabricate 3D microstructures, nano manufacturing world", SPIE, Vol. 2906/58 (1996).

Takeshi Kasaya, Hideki Miyazaki, Shigeki Saito and Tomomasa Sato, "Micro-object handling under SEM by vision-based automatic control", pp.181-192, SPIE Proceedings Vol. 3519, Microrobotics and Micromanipulation (1998).

Kazuhiisa Ishii, Masayuki Nakao & Yotaro Hatamura, "A 1/100 Machine Tool to Fabricate 1/100 Micro Parts", Proc. of ASPE 12th Annual Meeting, Vol.16, Norfolk, Virginia, Oct. 5-10, 1997, pp. 482-485 (1997).

Hideki Miyazaki and Tomomasa Sato, "Mechanical Assembly of Three-Dimensional Microstructures from Fine Particles", Advanced Robotics, 11, pp. 169-185 (English) (1997).

Yotaro Hatamura, Masayuki Nakao & Tomomasa Sato, "Construction of Nano Manufacturing World", Microsystem Technologies, 1 (3), pp. 155-162, (English) (1995).

Masayuki Nakao, Yotaro Hatamura, Tomomasa Sato, Koichi Koyano, et al., "Integration of 3-D shape construction and assembly to realize micro systems", Microsystem Technologies, 1 (3), pp. 24-128 (English) (1995).

Yotaro Hatamura, "Realization of integrated manufacturing system for functional micromachines", The 1st International Micromachine Symposium, 1995, pp. 55-63, (English) (1995).

A Kawaji, F Arai, T Sugiyama and T Fukuda, "Three-dimensional bio-micromanipulation," Advanced Robotics, Vol. 13, No. 3, VSP and RSJ, pp. 321-322 (1999).

Suggested reading

Shuji Tanaka, Masayuki Nakao and Yotaro Hatamura, "Near-field photolithography to realize high resolution smaller than light wavelength stamp photolithography", Proc. of ASPE 12th Annual Meeting, Vol.16, Norfolk, Virginia, Oct. 5-10, 1997, pp. 521-524 (1997).

Osamu Nakabeppu, et al., "Experimental study on point contact transport phenomena using the atomic force microscope", Microscale Thermophysical Engineering, 1(3), pp. 201-213 (English) (1997).

M Hatakeyama, Shuji Tanaka, K Ichiki, Y Toma, M Nakao and Yotaro Hatamura, "Novel fast atom beam (FAB) processes for fabricating functional nano-structures on three-dimensional microstructures", Proc. Microsystem Technologies '96, Potsdam, pp. 499-504 (English) (1996).

Masayuki Nakao, Yotaro Hatamura, et al., "New-type focused fast atom beam (F-FAB) source and evaluation of emitted beam density distribution", Applied Surface Science, 100/101, pp. 277-282 (English) (1996)

S Tanaka, Masayuki Nakao and Yotaro Hatamura, et al., "New fast atom beam processing with separated masks for fabricating multiple microstructures", Thin Solid Films, 281/282, pp. 630-633 (English) (1996).



